AD-A099 990 TEXAS UNIV AT AUSTIN APPLIED RESEARCH LABS F/G 20/1
AXISYMMETRIC PROPAGATION OF A SPHERICAL N WAVE IN A CYLINDRICAL--ETC(U)
MAY 81 R D ESSERT N00014-75-C-0867
UNCLASSIFIED ARL-TR-81-22 NL

1 OF 2
AD
A099990

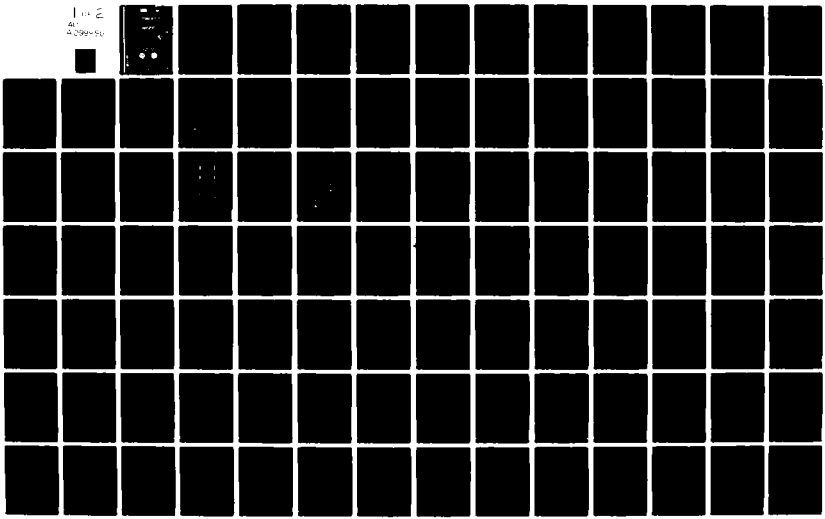

AD A099990

[redacted]

4 May 1981

Technical Report

APPROVED FOR PUBLIC RELEASE;
DISTRIBUTION UNLIMITED.

Prepared for:

OFFICE OF NAVAL RESEARCH
DEPARTMENT OF THE NAVY
ARLINGTON, VA. 22217

81 6 10 038

UNCLASSIFIED

SECURITY CLASSIFICATION OF THIS PAGE (When Data Entered)

(9) Master's thesis

REPORT DOCUMENTATION PAGE

READ INSTRUCTIONS BEFORE COMPLETING FORM

1. REPORT NUMBER

2. GOVT ACCESSION NO. AD-A099990

3. RECIPIENT'S CATALOG NUMBER

4. TITLE (and Subtitle)

(6) AXISYMMETRIC PROPAGATION OF A SPHERICAL N WAVE IN A CYLINDRICAL TUBE

5. TYPE OF REPORT & PERIOD COVERED

technical report

6. PERFORMING ORG. REPORT NUMBER

ARL-TR-81-22

7. AUTHOR(s)

(10) Robert Dale Essert, Jr.

8. CONTRACT OR GRANT NUMBER(s)

(12) N00014-75-C-0867

9. PERFORMING ORGANIZATION NAME AND ADDRESS

Applied Research Laboratories
The University of Texas at Austin
Austin, Texas 78712

10. PROGRAM ELEMENT, PROJECT, TASK AREA & WORK UNIT NUMBERS

11. CONTROLLING OFFICE NAME AND ADDRESS

Office of Naval Research
Department of the Navy
Arlington, Virginia 22217

(11)

12. REPORT DATE

4 May 1981

13. NUMBER OF PAGES

154

14. MONITORING AGENCY NAME & ADDRESS (if different from Controlling Office)

(12)

15. SECURITY CLASS. (of this report)

UNCLASSIFIED

15a. DECLASSIFICATION DOWNGRADING SCHEDULE N/A

16. DISTRIBUTION STATEMENT (of this Report)

DISTRIBUTION STATEMENT A
Approved for public release;
Distribution Unlimited

17. DISTRIBUTION STATEMENT (of the abstract entered in Block 20, if different from Report)

18. SUPPLEMENTARY NOTES

19. KEY WORDS (Continue on reverse side if necessary and identify by block number)

20. ABSTRACT (Continue on reverse side if necessary and identify by block number)

An experimental and theoretical study of the propagation of a spherical N wave in a rigid cylindrical tube is presented. Both source, an electric spark, and receiver, a very wideband condenser microphone, were located on the tube axis. Spark energies of between 0.04 J and 2.3 J were used. The received signal is a series of pulses. The first pulse is the direct N wave, which travels straight down the axis. Subsequent pulses represent waves reflected from the tube wall; their waveforms vary (they are not N shaped). There is, however, a shape repetition every fourth reflected wave. A theoretical analysis of the

DD FORM 1 JAN 73 1473 EDITION OF 1 NOV 65 IS OBSOLETE

404434

UNCLASSIFIED

SECURITY CLASSIFICATION OF THIS PAGE (When Data Entered)

20. (Cont'd)

problem was based on a solution of the linear wave equation for a dissipative medium. The solution, expressed as a ray expansion, indicates that the variation in pulse shape for low energy sparks is due primarily to focusing of the reflected rays each time they cross the tube axis: Each focus is accompanied by a 90° phase shift of the components making up the pulse. It was also found that atmospheric absorption and microphone directivity have important effects on the shapes of the received pulses. Both analytical and numerical methods were used to compute individual pulse waveforms from the theoretical results. For low spark energies (<0.1 J) computed and measured waveforms are in good agreement. For higher spark energies (>0.1 J) the shapes of the measured waveforms are altered by finite amplitude effects, and the simple linear theory is no longer sufficient to explain the results. A numerical propagation algorithm, which includes nonlinear propagation distortion, has been proposed. A qualitative rendering of the algorithm accounts reasonably well for the observed changes in wave shape.

Accession For
NTIS GRA&I ☑
DTIC TAB ☐
Unannounced ☐
Justification
By
Distribution/
Availability Codes
Avail and/or
Dist Special
A

ARL-TR-81-22

AXISYMMETRIC PROPAGATION OF A SPHERICAL N WAVE IN A CYLINDRICAL TUBE

Robert D. Essert, Jr.

APPLIED RESEARCH LABORATORIES
THE UNIVERSITY OF TEXAS AT AUSTIN
POST OFFICE BOX 8029, AUSTIN, TEXAS 78712

4 May 1981

Technical Report

APPROVED FOR PUBLIC RELEASE;
DISTRIBUTION UNLIMITED.

Prepared for:

OFFICE OF NAVAL RESEARCH
DEPARTMENT OF THE NAVY
ARLINGTON, VA 22217

FOREWORD

This report is an adaptation of the master's thesis of Robert D. Essert, Jr., "Axisymmetric Propagation of a Spherical N Wave in a Cyclindrical Tube". Mr. Essert was enrolled in the Department of Mechanical Engineering and received his degree in December 1980.

This research was carried out at Applied Research Laboratories and was supported by the Office of Naval Research under Contract N00014-75-C-0867. Scientific Officer for ONR was Dr. Logan E. Hargrove.

PRECEDING PAGE BLANK-NOT FILMED

TABLE OF CONTENTS

	Page
FOREWORD	iii
LIST OF FIGURES	vii
GLOSSARY OF IMPORTANT SYMBOLS	ix
CHAPTER I INTRODUCTION	1
A. Description of the Problem; Motivation by Experiment	1
B. Background	8
C. Outline and Scope of the Study	15
CHAPTER II EXPERIMENT	17
A. Apparatus	17
B. Microphone Calibration	24
C. System Alignment and Experimental Procedure	32
D. Preliminary Results: Sample Waveforms	33
CHAPTER III THEORETICAL ANALYSIS	36
A. Mathematical Formulation of the Problem	36
B. Fourier Transform $t \to \omega$, $x \to \xi$	41
C. Solution of the Radial Equation	43
D. Alternative Derivation of the Guided Pressure Field-- The Method of Images	48
E. Inverse Fourier Transform $\xi \to x$: Method of Stationary Phase	52
F. Inverse Fourier Transform $\omega \to t$: Analytical Evaluation	60
G. Inverse Fourier Transform $\omega \to t$: Digital Evaluation	69

PRECEDING PAGE BLANK-NOT FILMED

Page

CHAPTER IV COMPARISON OF EXPERIMENTAL AND THEORETICAL RESULTS: SMALL-SIGNAL WAVES 75

A. Influence of Absorption and Microphone Directivity on the Pulse Waveforms 76

B. Computer Solution for a Nonideal Input Waveform 81

C. Amplitude Envelope 84

D. Off-Axis Measurements 87

E. Summary 90

CHAPTER V PROPAGATION OF FINITE-AMPLITUDE WAVES IN THE TUBE 91

A. Measurements 91

B. A General Propagation Algorithm 94

C. An Algorithm for the Propagation of Axisymmetric Waves in the Tube 98

D. Qualitative Results 105

CHAPTER VI SUMMARY AND CONCLUSIONS 109

APPENDICES 113

APPENDIX A 90° PHASE SHIFT OF A BROADBAND SIGNAL 114

APPENDIX B ATMOSPHERIC ABSORPTION OF A SMALL-SIGNAL N WAVE 116

1. Quadratic Approximation for α 117

2. Propagation of a Small-Signal N Wave; Approximate Absorption 122

3. Digital Implementation; ANSI Standard Absorption 126

4. Experiment 129

APPENDIX C PROGRAM LISTINGS 135

REFERENCES 144

LIST OF FIGURES

Figure	Title	Page
1.1	Experimental Apparatus for N Wave Propagation in a Tube	2
1.2	Signals Received on Axis (Long Time Record)	4
1.3	First Received Pulses	5
1.4	Progression of Direct and Reflected Wave Fronts in the Tube	7
2.1	Electrode and Microphone Assemblies	18
2.2	Arrangement of Short and Long Tubes, Source, and Receiver	20
2.3	Ideal N Wave and Idealizations of Measured N Waves	29
2.4	Microphone Calibration Data	30
2.5	Measured Waveforms, Short Tube	34
3.1	Axisymmetric Coordinate System	39
3.2	Real and Image Sources	49
3.3	Travel Paths of Real and Image Waves	55
3.4	Off-Axis Geometry	58
3.5	Calculated On-Axis Waveforms for a Lossless Medium	66
3.6	Ideal N Wave After Successive Phase Shifts	68
3.7	Simplified Flow Chart of Program NTUBE	73
4.1	Effects of Atmospheric Absorption and Microphone Directivity on Waveforms Measured on Axis (Short Tube)	80
4.2	Comparison of Measured and Computed Waveforms (Short Tube)	82
4.3	Amplitude Envelope--Odd Numbered Reflections (Long Tube)	85
4.4	Estimated Microphone Offset--Odd Numbered Reflections (Long Tube)	88

Figure	Title	Page
4.5	Waveforms Measured On and Off Axis	89
5.1	Effect of Finite Amplitude on Measured Waveforms	93
5.2	Translated Coordinate System	99
5.3	Simplified Flow Chart for Proposed Propagation Algorithm	103
5.4	Finite Amplitude Pressure Waveforms	107
B.1	Absorption Curves for Air: ANSI Standard and Polynomial Fit	119
B.2	Analytical Solution for Various Values of tne Absorption Parameter η	125
B.3	Computer Algorithm for Evaluating Absorption Effects on a Signal of Arbitrary Time Waveform	126
B.4	Comparison of Ideal N Waveforms Calculated by Analytical and Digital Methods for Various Values of the Absorption Parameter η	128
B.5	Measured and Computed N Waveforms as a Function of Range	131
B.6	N Waveforms Calculated by Analytical and Digital Methods as a Function of Range	133

GLOSSARY OF IMPORTANT SYMBOLS

a	tube radius
c_o	small-signal, adiabatic sound speed
f	frequency
i	ray segment index
j	$\sqrt{-1}$
$\vec{k}$	complex propagation vector
n	reflected wave index
$p(t)$	acoustic pressure (time domain)
p_o	ambient pressure
r	radial coordinate
r_n	2na (radius of the nth ring image source)
t	dimensional time coordinate
t'	retarded time
x	axial coordinate
A_{ni}, A_i	point of ith reflection (Chapters III, V, respectively)
A, B	coefficients in approximate absorption α^* (Appendix B)
$D(\theta)$	Piston directivity $2J_1(k\sigma\sin\theta)/k\sigma\sin\theta$
$F(\omega)$	$\mathcal{F}[N(t)]\left(1+j\omega\nu\Gamma/c_o^2\right)$
$\mathcal{F}[g(t)]$	Fourier transform of $g(t)$
$H_m^{(1,2)}(z)$	Hankel functions of the first and second kind of order m
$J_m(z)$	Bessel function of the first kind of order m

O_i	position of ith focus
$O[z]$	of order z
$P(\omega)$	$\mathcal{F}[p(t)]$, acoustic pressure (frequency domain)
P_o	peak pressure amplitude at position R_o
Pr	Prandtl number
$\vec{R}$	vector coordinate
R	direct travel path length $\left(x^2+r^2\right)^{1/2}$, or $x \cos\theta + r \sin\theta$
R_n	path length for the nth reflected signal $\left(x^2+r_n^2\right)^{1/2}$, or $x \cos\theta_n + r_n \sin\theta_n$
R'	$r \sin\theta_n$
T	absolute temperature (Chapters III, IV, Appendices B, C), N wave half-duration (Chapter II)
T_o	reference N wave half-duration (duration of 1st half for nonideal N wave)
α	atmospheric absorption coefficient, as given by ABSORP
α^*	approximate absorption coefficient $A\omega^2 + B$
β	$(\gamma+1)/2$
γ	ratio of specific heats
Γ	$(\lambda+2\mu)/\mu + (\gamma-1)/Pr$
$\delta(z)$	Dirac delta function
η	dimensionless absorption parameter
θ	azimuthal angle of propagation
λ	dilatational coefficient of viscosity
μ	shear coefficient of viscosity
ν	kinematic viscosity μ/c_o

ξ	axial wave number
ρ	radial wave number
ρ_o	ambient density
σ	microphone radius
ϕ	dimensionless time t'/T_o
Φ	initial phase of a wavelet
χ	reflection coefficient
ω	angular frequency $2\pi f$

CHAPTER I

INTRODUCTION

This thesis documents an experimental and theoretical investigation of the sound field produced by a transient point source in a cylindrical tube. The field is made up of the direct pulse and a sequence of pulses representing reflections from the tube wall. Linear theory is used to explain the amplitude and phase of waveforms measured on the tube axis. The solution, given as a series expansion in terms of rays, provides an adequate explanation of the measured waveforms for low source amplitudes. Measurements indicate the growth of nonlinear effects as the source amplitude is increased.

A. Description of the Problem; Motivation by Experiment

Because the genesis of our study was experimental in nature, we begin this work with a brief description of the measurement system and some preliminary data. The measurements are discussed in greater detail in Chapter II. The basic apparatus is sketched in Fig. 1.1. A high voltage spark source was used to produce a short pressure transient on the axis of an air-filled aluminum tube. The pressure pulse emitted by the spark was an N wave, so called because of its resemblance to the capital letter N. The typical duration of the N wave was 10 μsec, and the electrode gap was small enough that the spark could be considered a point source. Two different lengths of tube were used, as is indicated by the two microphone positions in the sketch. The inside diameter of the tube was 5.1 cm, and the lengths of the short and long tubes were about 1.5 and 15 diameters, respectively. The receiver was a wideband

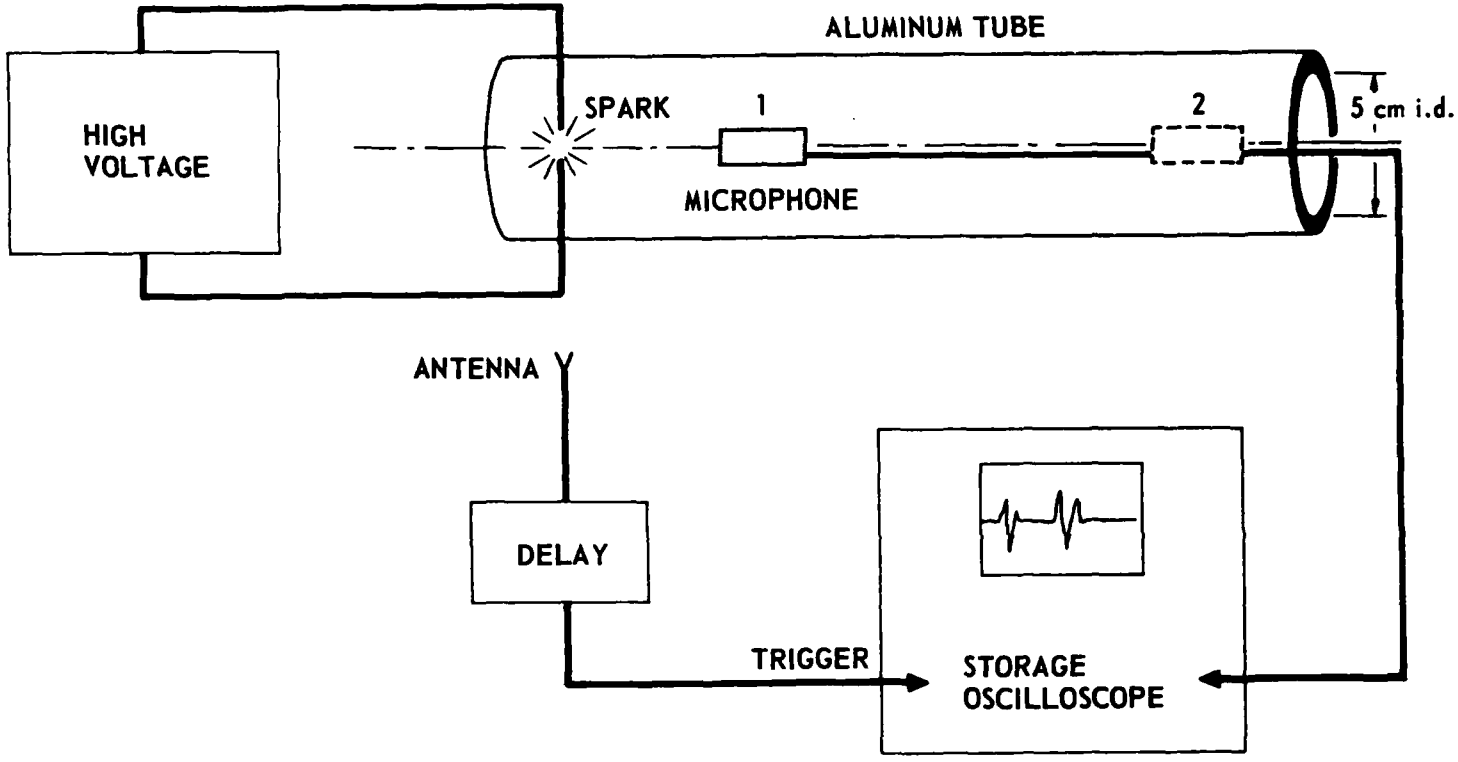

FIGURE 1.1
EXPERIMENTAL APPARATUS FOR N WAVE PROPAGATION IN A TUBE

ARL-UT
AS-79-2160-S
RDE-GA
11-6-79
REV 6-16-80

condenser microphone, centered on the axis of the tube. The active portion of the microphone had a diameter less than 4% of the tube diameter, and so approximated a point receiver. The microphone preamplifier, not shown, but located outside the tube, was connected directly to a digital oscilloscope. The oscilloscope was triggered after an appropriate delay by the electromagnetic radiation from the spark.

Oscillograms of the on-axis pressure at the two different microphone positions are shown in Fig. 1.2. Each series of pulses begins with the reception of the direct N wave which has traveled straight down the tube axis. A series of reflected signals follows. The first of these represents a wave reflected from the tube wall midway between source and receiver, the second represents a twice reflected wave, and so on. In the long tube, the first several reflected signals overlap because path length differences are smaller than the pulse length. In the short tube, however, all pulses are resolved in time.

Some important features of the behavior of the pressure waveform are evident in Fig. 1.2. First, most of the reflected signals are larger in amplitude than the direct wave. Second, the overall envelope of the pulse peaks increases to a maximum and then slowly decays. The rise and fall are more rapid in the short tube. Third, the envelope exhibits oscillatory behavior. The "period" of oscillation is four pulses.

In order that the individual pulse shapes may be more closely examined, the first half of the oscillogram in Fig. 1.2(b) is repeated in Fig. 1.3 on an expanded time scale. A fourth observation may now be made: Although the direct arrival is an N wave, later arrivals are <u>not</u> N waves; the delayed pulses are different from the direct wave in shape

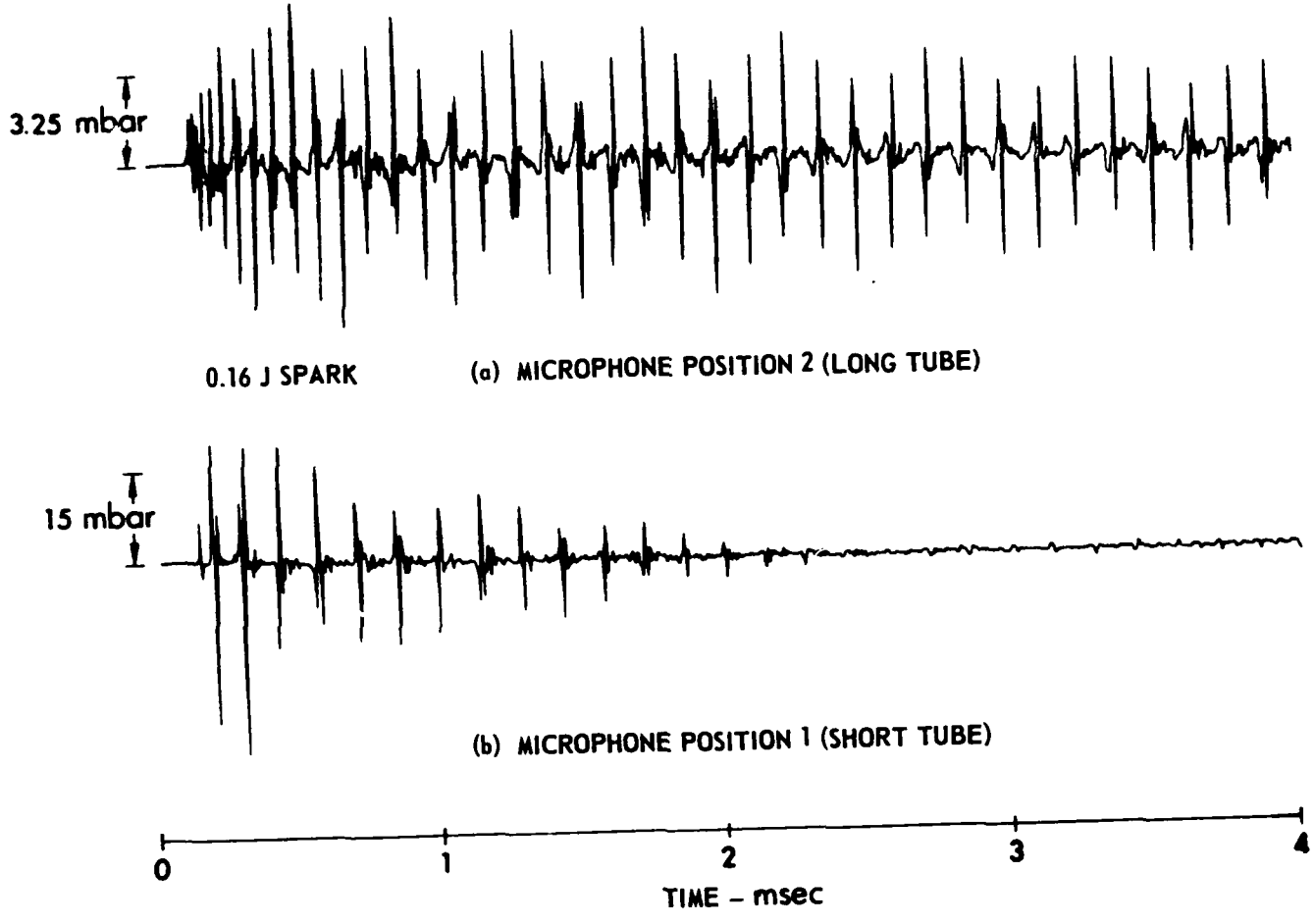

FIGURE 1.2
SIGNALS RECEIVED ON AXIS
(LONG TIME RECORD)

ARL:UT
AS-79-2161-S
RDE-GA
11-6-79

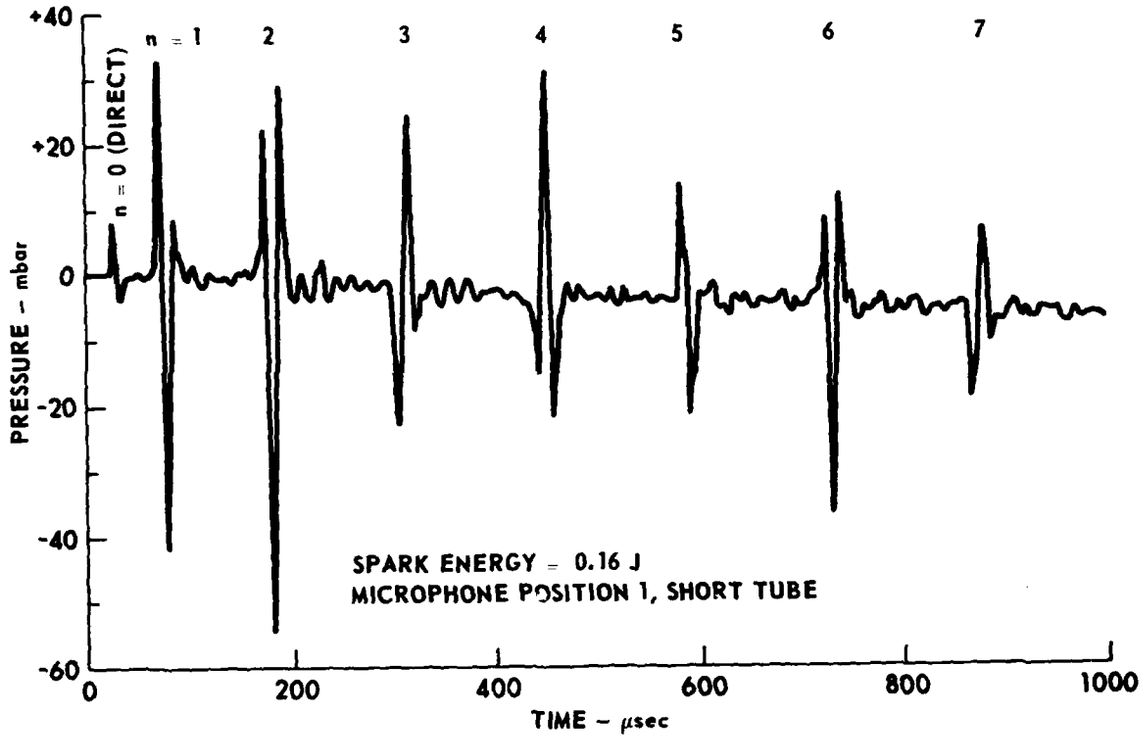

FIGURE 1.3
FIRST RECEIVED PULSES

AR:UT
AS-80-1154
RDE-GA
5-12-80
REV 6-16-80

as well as amplitude. It is seen that the oscillatory behavior of the amplitude envelope is associated with a periodic variation in wave shape: the fifth reflected wave (n=5) resembles the first (n=1), the sixth resembles the second, and so on. The sequence of four wave shapes is repeated indefinitely.

We submit that the sequential change in wave shape is due to cumulative 90° phase shifts.* The tube wall is a curved reflector; indeed, it is a cylindrical mirror. Focusing produced by a cylindrical mirror is two dimensional, and whenever a wave passes through a two-dimensional focus, it suffers a phase lag of 90°.[1] In the tube reflected portions of the confined wavefront cross the axis at least once (see Fig. 1.4). Because the axis is a line on which the convergent waves focus, the phase of each reflected front changes abruptly there. The phase of the divergent post-focus front lags that of the corresponding pre-focus front by $\pi/2$. As each part of the wavefront alternately converges and diverges, its relative phase lag increases in increments of $\pi/2$. Hence, every fourth reflected wave possesses a cumulative phase shift of 2π, and the wave shape repeats.

A primary objective of this investigation is to analyze the salient features of the waveforms measured on the axis of the tube. A valid mathematical description should account explicitly for the amplitude variation and cumulative phase shift exhibited by the measured waveforms. In Chapter III it is shown that a solution of the linear wave equation for a lossy medium provides an adequate explanation of the measurements for low source amplitudes. At high source amplitudes, measured waveforms differ

---

*A transient signal is said to undergo a 90° phase shift when the phase of each frequency component in the signal is shifted 90°.

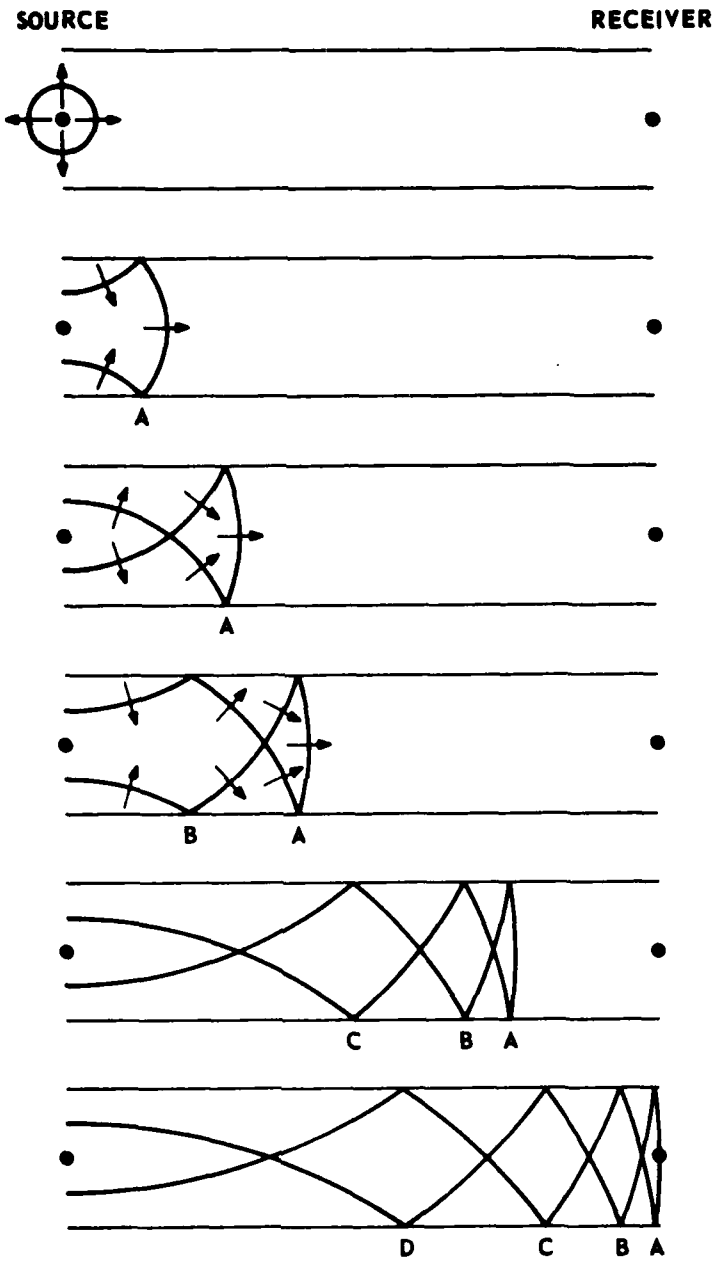

FIGURE 1.4
PROGRESSION OF DIRECT AND REFLECTED WAVE FRONTS IN THE TUBE

PHASE LAG AT POINT A IS 0; B, $\pi/2$; C, π; D, $3\pi/2$
ARROWS INDICATE DIRECTION OF TRAVEL

ARL:UT
AS-80-1279
RDE-GA
6-13-80

substantially from those predicted by linear theory. The discrepancies are attributed to nonlinear propagation distortion.

B. Background

Sound propagation in acoustic waveguides may be discussed in terms of either normal modes or rays. Of major concern in deciding which approach is more appropriate in a given situation is the ratio of the acoustic wavelength λ to a characteristic dimension of the waveguide. A commonly used parameter is ka, where $k=2\pi/\lambda$ and a is the characteristic dimension. Mode solutions are, in principle, valid for all possible values of ka, but they must often be evaluated numerically and can become unwieldy when the source frequency is high enough to excite a great many modes. Ray solutions are valid only for $ka \gg 1$, but they have an important advantage over mode solutions: they have more appeal for physical understanding. Hamet[2,3] analyzed the problem of a point source in a cylindrical tube in terms of both modes and rays. His results are of limited practical applicability.

In the present problem, the signal is a transient whose duration is short compared to travel time across the tube. The sample measurements in Figs. 1.1 and 1.2 show that the sound field on the axis is a superposition of direct and reflected waves. Consequently, a solution given in terms of rays may be more readily applicable than a mode solution. In fact, a ray path solution can be derived from the mode solution in the limit of short wavelength. The direct path between source and receiver corresponds to the fundamental (plane wave) mode, the reflected paths to higher order (transverse) modes. The results contained in this thesis will be interpreted, for the most part, in terms of ray theory.

It is shown in Chapters III and IV that focusing on the tube axis and energy dissipation by the medium are primarily responsible for the modification of the N shape as the wave propagates down the tube. These two mechanisms have been investigated independent of one another by other researchers, but little work has been published that accounts for focusing and absorption together. In his modal analysis (Ref. 2) Hamet accounted for thermal and viscous boundary layer losses, but he did not deal with the problem of focusing. In his ray path analysis (Ref. 3) he recognized that the reflected wavefronts must focus, but he neglected losses altogether.

We now draw attention to research efforts of others that have contributed to our understanding of the present problem. First, studies of absorption and dispersion of sound waves by the medium are discussed. Next, we review time domain methods used in dealing with pulses and note how those methods have been applied to problems involving the focusing of acoustic transients and the propagation of finite amplitude sound in tubes. Finally, relevant work in some areas of applied acoustics is mentioned.

1. Absorption and dispersion in an air-filled tube. It is now known that the three most important causes of sound attenuation and dispersion in an homogeneous atmosphere are viscosity, thermal diffusion, and molecular relaxation. While molecular relaxation is a comparatively new field of study, sound propagation in a viscous, heat conducting (thermoviscous) medium has been investigated for over a century. In 1868 Kirchhoff[4] reported an analysis of quasi-plane waves in a cylindrical tube containing a thermoviscous gas. He found an exact dispersion relation satisfied by the complex wave number k, but his result is in the form of

a complicated transcendental equation that cannot in general be solved explicitly. By assuming that the boundary layer effects (viscous drag and heat conduction at the tube wall) were of much greater importance than mainstream effects (friction and heat conduction that occur in the main body of the fluid, away from the tube wall), Kirchhoff was able to determine an approximate form for k that may be easily incorporated in a frequency domain solution for plane progressive waves in a tube.† The effect of thermoviscous boundary layer absorption on higher order modes in waveguides was the subject of much discussion in the early 1950's.[6-11] Using different methods, Beatty[10] and Lambert[11] arrived at equivalent expressions for the boundary layer attenuation of higher modes. Neither considered the dispersive effects of the boundary layer, nor of the mainstream absorption. In our problem mainstream absorption is larger than boundary layer absorption; so either boundary layer effects must be neglected altogether, or a more rigorous solution of the full Kirchhoff dispersion relation, restated for higher order modes, must be attempted.

More recently, several researchers have utilized numerical techniques to calculate absorption and dispersion from the Kirchhoff solution. Shields, Lee, and Wiley[12] were the first to compute a numerical solution for the plane wave mode from the exact Kirchhoff equation. Their results were later verified experimentally by Shields, Bass, and Bolen[13] over a wide range of frequencies. Tijdeman[14] developed a numerical model similar to that of Shields, Lee, and Wiley[12] after rewriting the Kirchhoff equation in terms of the compressional wave number, the shear

---

†Kirchhoff's analysis was repeated by Rayleigh in his treatise of 1877.[5]

wave number, and a reduced frequency parameter. The Tijdeman paper also contains a review of other important analytical and numerical solutions of the Kirchhoff equation.

Scarton and Rouleau[15] calculated attenuation and dispersion curves and mode shapes for the first thirty-two axisymmetric modes in a tube filled with a viscous liquid. Their solution contains both mainstream and boundary layer viscosity effects, but it does not include the influence of heat conduction. Uncoupled scalar and vector viscous wave equations are solved for each particular value of the product of frequency and viscosity (which is proportional to the boundary layer thickness). Such calculations are beyond the scope of this investigation.

Since it was not possible to obtain a manageable solution of the thermoviscous wave equation valid for our problem, boundary layer effects were neglected altogether. Implications of this decision and further justification for it are discussed in Chapters III and IV.

Viscosity, heat conduction, and molecular relaxation all make important contributions to mainstream absorption, but the relative importance of each varies with frequency. Within the frequency interval of interest in the present study, 10 kHz - 1 MHz, each of the three absorption mechanisms is important. Atmospheric absorption of a small-signal N wave is discussed in Appendix B of this work. For further information on the study of atmospheric absorption the reader is referred to Appendix B and Refs. B.1-B.4.

2. Time domain analysis of the diffraction and focusing of pulses. The Helmholtz-Kirchhoff (or simply Kirchhoff) integral theorem has been employed by many researchers in their analyses of the refraction,

diffraction, and reflection of small-signal acoustic pulses. The theorem gives the value of the field at a point Q in terms of an integral of certain properties involving the pressure and pressure gradient on a surrounding surface S.† Anderson, Northwood, and Barnes[16] used the Kirchhoff integral to obtain a solution for a pulse reflected from the inside surface of a sphere. Agreement between their measurements and theory was compromised by the fact that their transducers were not omnidirectional. A time domain analysis of broadband refraction and diffraction was published by H. A. Wright.[17] The accompanying experimental results were obtained using an (approximately) omnidirectional spark source. The Kirchhoff integral has been applied by Lockwood[18] and by Cobb[19] to diffraction of N waves in lossless media. W. M. Wright[20] has studied the scattering of N waves by plates and cylinders and interference of reflected and diffracted signals at the face of a microphone.

Most of the pulse-to-pulse variation in wave shape observed in the present study is due to focusing. Since the advent of supersonic aircraft there have been numerous studies related to sonic boom focusing. The theoretical work of Whitham[21,22] provided a strong foundation for later experimenters in acoustics and fluid mechanics. Whitham described how the process of self-refraction can prevent focusing: As a concave wavefront approaches a focus, the points near the center of the front travel faster than those near the edge. If finite amplitude effects are large compared to absorption effects, the center of the front overtakes the edge, and the once concave front turns convex without ever passing through a focus. The refraction and diffraction of finite-amplitude N waves by gas bubbles were

---

†Anderson[30] derived the Kirchhoff integral for a lossy medium.

observed by Davy and Blackstock.[23] Beasley, Brooks, and Barger[24] investigated two- and three-dimensional focusing of finite amplitude, spark produced N waves. Cornet[25] used an improved microphone to perform experiments for the three-dimensional case. In his theoretical analysis, Cornet began with the Kirchhoff integral and later included nonlinear distortion. The signal at the focus was, in the linear approximation, predicted to be the derivative of the original signal. It will be shown in a later section of the present work that a "half-derivative" of the original signal is predicted at a two-dimensional focus.

The focusing of intense transients other than spark produced N waves is relevant to this discussion. Measurements of three-dimensional focusing in a shock tube have been published by Sturtevant[26] and by Sturtevant and Kulkarney.[27] The measurements are qualitatively explained by the theory of Whitham. Sanai and Toong[28] modeled sonic boom focusing on a ballistics range. They observed focusing due to increasing Mach number ("acceleration superboom") and medium stratification ("refraction superboom").

Stepwise propagation algorithms have proved to be worthwhile tools in the study of nonlinear acoustical phenomena. Nonlinear distortion is calculated in the time domain over a short propagation distance. Then a correction is made for losses and dispersion, which are computed in the frequency domain. Pestorius[29] used such an algorithm to investigate the propagation of plane, finite amplitude waves in a tube. He assumed that all absorption and dispersion were due to the presence of a thermoviscous boundary layer. A short time later, Anderson[30] used a similar routine to analyze the propagation of a spherical N wave in the open

atmosphere. To this date, no author has proposed a solution of the problem of two-dimensional focusing of either large or small amplitude waves in a lossy medium. This problem is of fundamental concern in the present study.

3. Relevant work in applied acoustics. In the preceding paragraphs we have endeavored to illuminate the diversity of the basic research which forms the foundation of this paper. Let us now examine some applied research that has provided direction for, and may benefit from, the results to be presented in this thesis. For example, guided propagation of sonic booms has received recent attention. Gardner and Rogers[31,32] developed an elaborate analytical model to describe the propagation of sonic booms in the thermosphere. They accounted for nonlinear propagation distortion and atmospheric absorption and predicted a 90° phase shift of the pressure wave.

Consider next the growing interest in the study of borehole acoustics. Techniques associated with the use of sound to determine geologic structure have undergone considerable theoretical development. Far-reaching results for sound propagation within the borehole were given by Roever, Rosenbaum, and Vining,[33] while propagation between boreholes was studied by Hall, Miller, and Simmons.[34] Our investigation concerns a highly simplified version of the former problem. One of the most important virtues of our study is its simplicity. Full-scale borehole measurements are often quite difficult to explain. It is assumed in the present study that one has control of, or at least knowledge of, the environmental conditions and the physical properties of the tube.

Finally, we mention the importance of our work to the study of core noise radiated by turbofan engines. Core noise originates within the engine, which is basically a duct of finite length. Salikuddin et al.[35] developed a method for measuring the radiation from a duct/nozzle system, using a spark source inside the duct. The source was located on-axis, and its spectral density was, for the most part, concentrated below the lowest cutoff frequency. Consequently, the pulse traveled down the duct as a quasi-plane wave front. Although the authors do not mention it in the paper, a portion of the duct surrounding the source was lined with sound absorbing material to suppress unwanted reflections[36]--the very reflections we wish to observe. Whether the first few reflected waves (corresponding to the low order transverse modes) were effectively attenuated is questionable. It is possible, however, that the results to be described in this thesis may find application in the study of high frequency radiation from ducts and nozzles.

C. Outline and Scope of the Study

The remainder of this thesis is organized as follows. The experimental apparatus and procedure are described in Chapter II and sample measured waveforms are presented. Chapter III contains a theoretical analysis of the problem. The wave equation is solved for a point source on the axis of a tube containing a lossy gas. Both on- and off-axis observation points are considered. The solution is given in terms of a ray expansion in integral form that is valid for any low amplitude, high frequency signal. The integral may be evaluated in closed form if the source is omnidirectional and the medium nondissipative. For less restrictive conditions, digital methods are required to evaluate the integral

solution. The effects of medium dissipation and receiver directivity are included in a numerical solution for a real (measured) N wave source function. Computed waveforms and low amplitude measured waveforms are compared in Chapter IV. Results of measurements made a high source amplitudes are presented in Chapter V. Differences between the high and low amplitude measurements are attributed to nonlinear effects. A numerical algorithm, which includes the contributions of nonlinear propagation distortion, focusing, and atmospheric absorption, is proposed. Chapter VI contains a summary of the results and some concluding remarks.

Three appendices are included. Appendix A contains a brief discussion of the application of a 90° phase shift to a broadband signal. In Appendix B analytical and digital models of the atmospheric absorption of a small-signal N wave are derived, and results are compared with data from a free-medium propagation experiment. Appendix C contains listings of the programs developed to compute on-axis waveforms for the linear case.

CHAPTER II

EXPERIMENT

A general account of the experiment was presented at the beginning of the previous chapter. This chapter contains detailed descriptions of the measurement apparatus and method, and results obtained therefrom. First, the spark source, aluminum tube, microphone, and electronic system are discussed. Next, the microphone calibration and system alignment procedures are outlined. Finally, measurements of the pressure waveforms observed on the axis of the tube are introduced.

A. Apparatus

The measurement system was composed of four basic subsystems--spark source, cylindrical waveguide, condenser microphone, and data capture equipment (see Fig. 1.1). The important features of each are described in the following paragraphs.

1. Spark Source. A Spellman Model PN-30 0-30 kV dc power supply was used to charge a capacitance of 0.083 μF, made up of six 0.5 μF condensers connected in series, to between 0.5 and 7.5 kV. The possible range of spark energies was thus 0.01 to 2.3 J. A 66 MΩ resistor wired in series with the capacitor limited the charging current.

The capacitance was allowed to discharge across a gap between two diametrically opposed tungsten electrodes. Each electrode was 0.16 cm in diameter, and its point was ground to a cone of half-angle roughly 30°. A lucite ring, 5.1 cm i.d. (the same as the i.d. of the aluminum tube), 11.2 cm o.d., and 2.5 cm length, was machined to support the electrodes in the tube [see Fig. 2.1(a)]. The spark gap was centered on the tube axis;

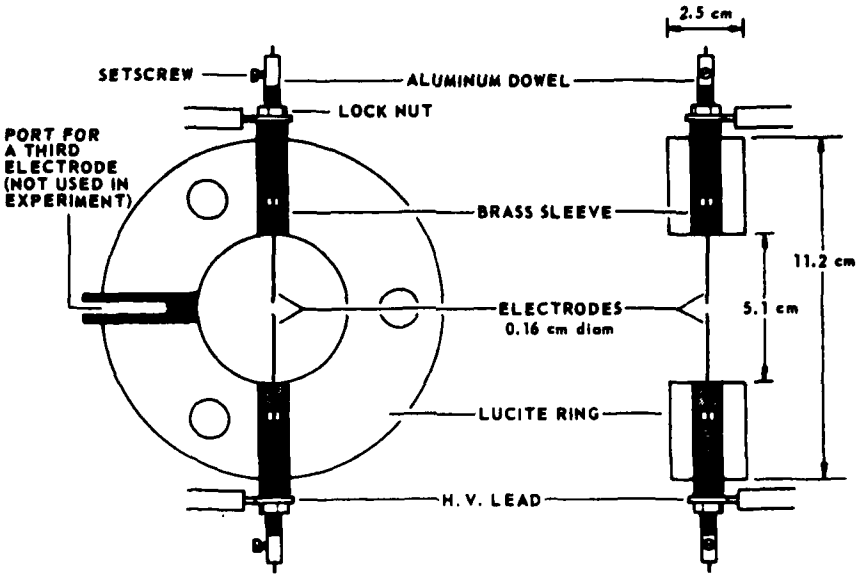

(a) ELECTRODE ASSEMBLY

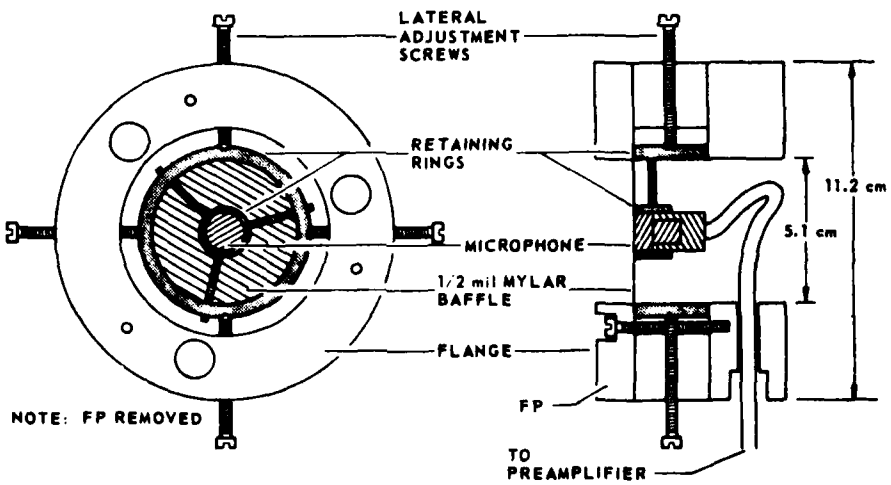

(b) MICROPHONE ASSEMBLY

FIGURE 2.1
ELECTRODE AND MICROPHONE ASSEMBLIES

ARL:UT
AS-80-1280
RDE-GA
6-13-80

typical gap lengths were between 0.01 and 0.2 cm. The electrodes were held in threaded aluminum dowels, which allowed symmetric adjustment of the spark gap from outside the tube. When the voltage across the capacitor reached the breakdown voltage of air, the capacitor discharged through the gap. The voltage across the capacitor was monitored by means of a Simpson Model 260 voltmeter.

2. Aluminum Tube. Two different lengths of tube were used in the experiments (see Fig. 2.2). The long tube was composed of the lucite electrode holder, a connecting flange, a 71.1 cm length of aluminum tubing (wall thickness 0.32 cm), a second connecting flange, and the microphone holder. The elements making up the short tube were the same electrode and microphone assemblies and a single connecting flange, 4.9 cm in length. The i.d. of each component was 5.1 cm. Care was taken in construction and alignment of the various components to minimize surface irregularities at the junctions. The total axial distance from source plane to receiver plane was 76.2 cm in the long tube and 7.4 cm in the short tube. A 15 cm length of tube containing approximately 5 cm of fiberglass was fastened to the back side of the electrode holder to absorb backward traveling waves. The tube wall could be considered a rigid boundary for the present problem.

A wave front incident on the inside face of the tube wall is partly reflected back into the air and partly transmitted into the tube wall. Of concern here is the airborne reflected wave. It is assumed that the boundary is locally reacting and that shear coupling between the air and aluminum is negligible. It is assumed also that the propagation vector for the incident wave has no circumferential component. Consider a reflected wave incident on the tube wall at grazing angle θ_n. The

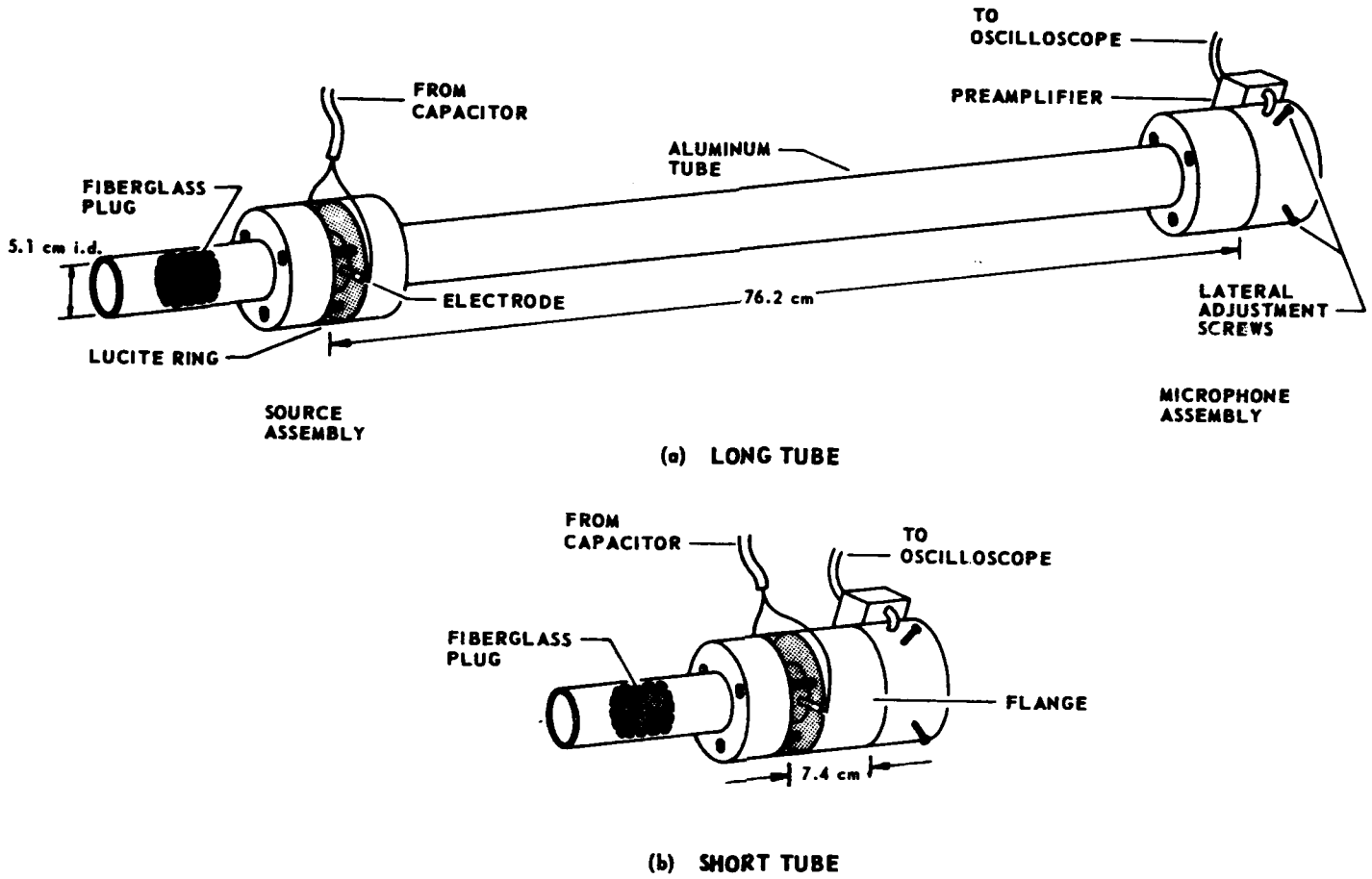

FIGURE 2.2
ARRANGEMENT OF SHORT AND LONG TUBES, SOURCE, AND RECEIVER

ARL-UT
AS-80-1281
RDE-GA
6-13-80

angle of reflection is equal to the angle of incidence, and the angle of transmission θ_n^t is given by Snell's law,

$$\cos\theta_n^t = (c_2/c_1)\cos\theta_n \quad ,$$

where c_1 and c_2 are the sound velocities in air and aluminum, respectively. The reflection coefficient χ_n for a single reflection is given by

$$\chi_n = \frac{Z_2 \sin\theta_n - Z_1 \sin\theta_n^t}{Z_2 \sin\theta_n + Z_1 \sin\theta_n^t} \quad ,$$

where Z_1 and Z_2 are the characteristic impedances of the two media. By the time the signal reaches the receiver, it has been reflected from the tube wall n times. The cumulative reflection coefficient is therefore equal to $\left(\chi_n\right)^n$. For all cases of interest in this study (n=1-35, long tube; n=1-15, short tube) θ_n is less than the critical angle $\theta_{cr} = 86.9°$, and as a result χ_n is complex. However, since $\mathrm{Re}\left[\left(\chi_n\right)^n\right] \geq 0.99990$ and $\mathrm{Im}\left[\left(\chi_n\right)^n\right] \leq 0.0134$, we were able to assume with inconsequential error that the tube was perfectly rigid, i.e., $\left(\chi_n\right)^n=1$, for values of n within the limits specified above.

'o different tubes were used to facilitate accurate measurement of both long time behavior (amplitude envelope) and short time behavior (individual pulse waveforms) of the sound field. Because of the high pulse density and slow decay rate, the long tube data [see Fig. 1.2(a)] are most useful in an analysis of the amplitude envelope. The pulse density is lower in the short tube waveforms (all pulses are resolved in time), but the envelope decays rapidly [see Figs. 1.2(b), 1.3]. The short tube was therefore used to investigate individual pulse shapes, and the long tube to study the amplitude envelope.

3. Microphone and Preamplifier. The condenser microphone and preamplifier used in this study were developed by Cornet[25] after designs by Wright.[37] Anderson[30] improved the construction process and was able to obtain a high degree of consistency from one microphone to the next. A diaphragm of 3.2 μ (1/8 mil) aluminized mylar is laid directly on a microscopically rough, conducting back plate. The transducer has a large bandwidth and a broad (low Q) resonance. While the outside diameter of the microphone cartridge used in this experiment is 1.3 cm, the back plate (and hence the active area) is just 0.20 cm in diameter. Because of the large bandwidth the transducer is relatively insensitive (sensitivity = -67.5 dB re 1 $V/N/m^2$) in relation to most commercially produced condenser microphones. However, the pressure waves produced in the tube were of sufficient amplitude that the microphone insensitivity presented no problems. Although the microphone was nearly a point receiver for low frequencies, its directivity characteristics profoundly influenced measurements of shock waves incident at oblique angles. The rise time of the transducer was measured from its response to moderately strong N waves (traveling in a direction perpendicular to the microphone face) and found to be approximately 0.4 μsec. The microphone sensitivity, directivity, and frequency response are addressed in greater detail in Section B, "Microphone Calibration." For further details of the general properties and construction of this type of transducer, the reader is referred to the work of Cornet.[25]

It was necessary to baffle the microphone to obtain accurate measurements. When a sound wave is incident on a freely suspended circular microphone, a diffracted wave propagates from the edge of the microphone toward the center. If all points on the circumference are

insonified by the incident wave at the same time, as is the case for normally incident and axisymmetric waves, the signals from all points superpose at the center.

The diffracted wave arrives at the active area later than the incident wave by a time corresponding to the difference in travel path lengths ΔR. If ΔR is less than or equal to the signal duration Δt, the two waves overlap. If, on the other hand, $\Delta R > \Delta t$, the signals are separated in time. A reflective baffle may be used to extend the face of the microphone to ensure separation of the signals. The pressure of the incident wave sensed at the surface of the microphone is twice the freefield pressure.

A special flange assembly was constructed for the purpose of mounting the microphone on the tube axis [see Fig. 2.1(b)]. Approximately 6.5% of the tube section area was occupied by the microphone cartridge. In order to minimize the effects of diffracted waves, a 12.8 μ (1/2 mil) mylar baffle was stretched loosely over the remaining area. The baffle is quite rigid at the high frequencies of interest.[†] The calculated reflection coefficient is nearly equal to unity for frequencies greater than 50 kHz, and falls to 0.7 at approximately 10 kHz. Lateral positioning of the microphone/baffle within the tube was accomplished through adjustment of two pairs of diametrically opposed setscrews.

The microphone preamplifier was mounted on the outside of the receiver assembly, and was connected to the microphone cartridge through the tube wall by a 15 cm length of low capacitance cable. The hole

---

[†]The baffle was originally designed to simultaneously reflect high frequency ($f > 10$ kHz) waves and pass low frequency ($f < 10$ kHz) waves. We are interested in frequencies between 10 kHz and 1 MHz.

in the tube wall, 6.4 mm in diameter, was located behind the baffle. Both calculation and measurement showed that the effect of the extra cable capacitance on the sensitivity was insignificant. Anderson measured the frequency response characteristic of the preamplifier as flat within ±0.16 dB from 250 Hz to 2 MHz.

4. Data Capture and Storage. The signal from the preamplifier was input directly to a Nicolet Model 2090-III digital oscilloscope, which was equipped with a Model 206-2 plug-in unit. Because the instrument's maximum digitizing rate is 2 MHz, its useful bandwidth is 1 MHz. Use of the entire 4096-point memory permitted the storage of 2 msec of data with a time resolution of 0.5 μsec/point and 12-bit accuracy. The transient capture capabilities of this unit were especially well suited to our task. Electromagnetic radiation from the spark discharge, picked up by a loop antenna, was used to indirectly trigger the oscilloscope. The trigger signal opened the gate of an EH Model 130 pulse generator set in single pulse mode. The oscilloscope was triggered some time later by the negative going edge of the pulse. By varying the pulse width one could delay the oscilloscope trigger until the acoustic wave arrived at the receiver. Captured waveforms were saved by either of two methods. Long waveforms (>100 points) were plotted directly on a Barry Research Model 5002 x-y recorder. Individual pulses (<100 points) were read out visually, point by point, and typed into computer memory for plotting at a later time.

B. Microphone Calibration

Several microphones fabricated by Cornet and Anderson were available for use. The rise time, overshoot, and sensitivity of each in

response to N waves of equal amplitude were measured with a Tektronix Model 5403 analog storage oscilloscope (an analog oscilloscope was used in this instance because its higher bandwidth allowed more accurate determination of the rise time and overshoot parameters).

The bandwidth of a transducer can be determined from measurements of its rise time. The high frequency limit to the response of a conventional condenser microphone is set by the mechanical resonance of the diaphragm mass against the stiffness of the air cavity between the diaphragm and backplate. Above the resonance frequency the response rolls off at 12 dB/octave. The bandwidth of a simple resonant system of this sort may be inferred from step response measurements according to a relation stated by Wallman,[38]

$$2\tau f_c = 0.69 \quad , \tag{2.1}$$

where τ is the 10-90% rise time and f_c is the -3 dB rolloff frequency. Our rise time measurements, however, were based on an N wave input, not a step input. Nonetheless, it may be demonstrated that when τ is much smaller than the N wave half-duration, the response of a low pass filter or damped oscillator to an N-shaped signal is closely approximated in the neighborhood of the head shock by the response to a step function of equal amplitude. The diaphragm of our microphone is placed directly on the backplate, and air is trapped in the microscopic cavities thus formed. The transducer, then, is a parallel combination of many small microphones of different sizes and, hence, different resonance frequencies. Cornet has shown that the frequency response of a parallel combination of microphones whose resonance frequencies are randomly distributed in a decade $f_o \leq f \leq 10\ f_o$ is similar to that of a single microphone whose resonance frequency is f_o. The major difference between the two cases is that

the multi-element system has a lower Q than the single microphone. Equation (2.1) was derived for a single microphone, but in light of the similarity just noted, it may be used to estimate the bandwidth of the multi-element microphone. Using Wallman's relation and the measured value of $\tau = 0.4$ μsec, one finds that the bandwidth is approximately 860 kHz. (A similar problem, the response of a Gaussian filter--the atmosphere--to an N wave, is discussed in Appendix B of this work.)

Microphone ringing was apparent in measurements of high amplitude N waves at short distances. The initial overshoot was of the order of 8%. Wallman's calculations show that the corresponding ratio of gain at resonance to gain at midband (this ratio is proportional to Q) is 1.05, or 0.4 dB. It is thus inferred that the frequency response of our microphone is flat within +0.5, -3.0 dB from near 0 Hz to 860 kHz.

Amplitude calibration of these transducers, which is done in the freefield, remains a rather tedious process. Cornet, Anderson, Cobb, and others have used a technique first described by Davy and Blackstock.[23] The method is based on certain amplitude dependent effects caused by nonlinear propagation distortion of finite amplitude N waves. The peak pressure amplitude P and half-duration T of a spherically divergent (ideal) N wave at radial distance r are related to the pressure P_o and half-duration T_o at some reference position r_o by the following:

$$rP = r_o P_o \left[1+\sigma_o \ln(r/r_o)\right]^{-1/2} , \tag{2.2}$$

$$T = T_o \left[1+\sigma_o \ln(r/r_o)\right]^{1/2} , \tag{2.3}$$

where

$$\sigma_o = \frac{(\gamma+1)}{2\rho_o c_o^3} \frac{r_o P_o}{T_o} \quad , \tag{2.4}$$

and ρ_o, c_o, and γ are the density, small-signal sound speed, and ratio of specific heats, respectively. Multiplying Eq. (2.2) by Eq. (2.3), one finds that the product TrP is constant, i.e.,

$$TrP = T_o r_o P_o \quad . \tag{2.5}$$

If Eq. (2.3) is squared, the result is

$$T^2 = T_o^2 + \sigma_o T_o^2 \ln(r/r_o) \quad . \tag{2.6}$$

Let the microphone sensitivity be defined as S=e/p, where e is the measured voltage and p is the free-field pressure (the pressure that would exist in the absence of the microphone). Equations (2.4) and (2.5) may be combined to yield

$$S^{-1} = \frac{2\rho_o c_o^3}{(\gamma+1)} \frac{\sigma_o T_o^2}{TrE} \quad , \tag{2.7}$$

where E is the voltage corresponding to the peak pressure P. The two parameters $\sigma_o T_o^2$ and TrE may be determined from measurements of the N wave amplitude and half-duration at various distances. The first is just the slope of T^2 versus $\ln(r/r_o)$ [see Eq. (2.6)], and the second may be accurately determined by calculating the average value of TrE over the various measurement positions.

A special procedure was used to determine T and P at each measurement distance r. The procedure was designed to reduce variability

caused by lack of repeatability in the spark production process. The transient capture capability of the digital oscilloscope allowed us to record N wave data much faster than was possible with an analog oscilloscope. The following method was used to determine the average peak voltage and half-duration at each measurement position. First, the breakdown voltage for each spark discharge was monitored with the dc voltmeter, and only those waveforms whose breakdown voltage was within 0.1 kV of the desired value were stored in the oscilloscope memory; approximately 25% of the discharges were within these limits. Ten acceptable N waveforms were stored for each measurement position, and average values of E and T were computed (typical standard deviations were between 2% and 5%). The spark source was then allowed to discharge until a waveform was captured whose amplitude and half-duration values were equal to the average values for that location. This waveform was called an "average waveform". The effects of microphone overshoot and finite rise time were identified in the measured N waves. A least-squares fit of the measured points in the first half of the waveform was performed in order to smooth the ripple caused by microphone ringing. The idealized head shock was located at a point midway between the foot and peak of the measured waveform. The idealization procedure is illustrated in Fig. 2.3. When the measured rise time (10-90%) τ was greater than 2 μsec, ringing was absent and the ripple smoothing step was omitted. The peak voltage E determined from the idealized waveform was used in all subsequent calculations. For more detailed descriptions of this idealizing procedure, see Refs. 19, 30.

N waveforms were recorded at eight source-receiver distances from 5 to 125 cm for a spark energy of 0.42 J and temperature 25°C

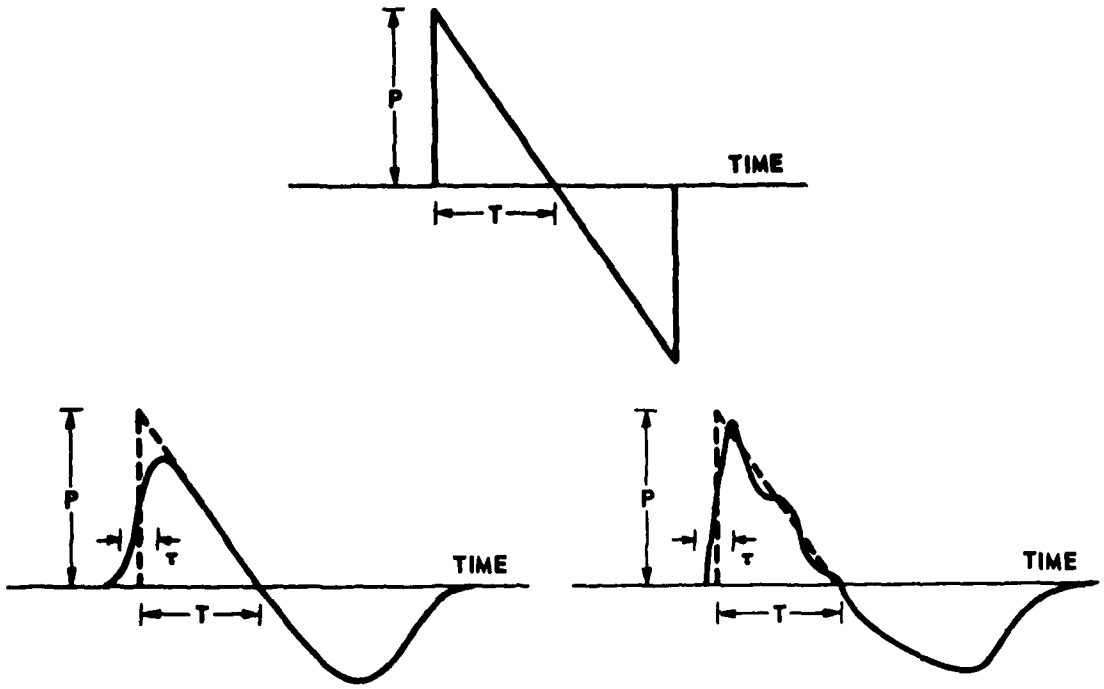

FIGURE 2.3
IDEAL N WAVE (ABOVE) AND IDEALIZATIONS OF MEASURED N WAVES (BELOW)

ARL:UT
AS-80-1282
RDE-GA
6-13-80

The standard deviation of each of the 10-term averages of E and T was less than 5%. Data for large distances (r = 90, 125 cm) was discarded because it clearly departed from the general trend. It is believed that the waves at these points were too weak to be adequately described by weak shock theory. The value of $\sigma_o T_o^2$ was computed from a linear regression of T^2 versus $\ln(r/r_o)$. The results are summarized as follows (see Fig. 2.4):

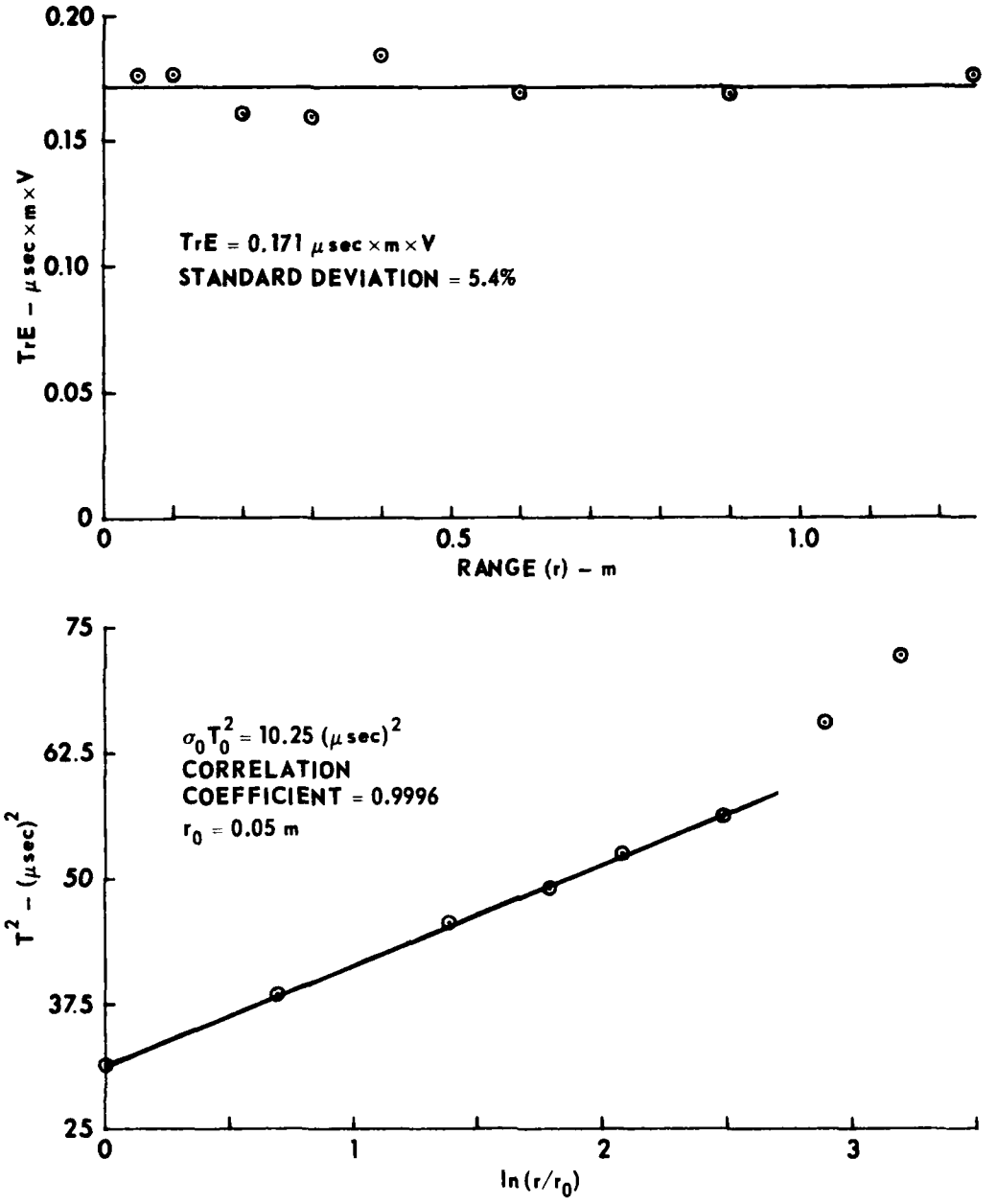

FIGURE 2.4
MICROPHONE CALIBRATION DATA

ARL:UT
AS-80-1283
RDE-GA
6-13-80

$$\overline{TrE} = 0.171\ \mu sec \cdot m \cdot V \quad , \quad \text{standard deviation} = 5.4\% \quad ,$$

$$\sigma_o T_o^2 = 10.25\ \mu sec^2 \quad , \quad \text{correlation coefficient} = 0.9996 \quad ,$$

and finally,

$$S^{-1} = 23.85\ mbar/V \quad .$$

It should be noted that S is the sensitivity of the overall receiver, including pressure doubling and preamplifier gain. The high degree of correlation is attributed to careful monitoring of the spark breakdown voltage, the accuracy of the oscilloscope, and the procedure of obtaining an average rather than a single measurement at each distance.

The amplitude linearity of this type of wideband transducer had not been previously studied. We compared the response of our microphone to that of a Brüel & Kjaer (B&K) Type 4138 1/8 in. condenser microphone and B&K Type 2619 preamplifier using normal incidence, spark produced N waves. The B&K combination has a specified distortion at 100 kHz of less than 4% for sound pressure levels below 177 dB (re 2×10^{-5} N/m^2). It was therefore assumed that the B&K unit is a linear receiver for N waves whose peak overpressures are less than 142 mbar. The rise time of the B&K microphone was found to be approximately 2 μsec; hence, it was necessary to base the amplitude comparison on the negative pressure peaks of the N wave signatures, where the waveforms are more slowly varying. Twelve peak voltage measurements were averaged for each transducer at each position and spark energy. Linearity of the wideband transducer was confirmed up to a peak pressure of 28 mbar. While making measurements of large amplitude waves in the tube, we found that the transducer or the preamplifier was overloaded (i.e., the output was temporarily open circuited) by pressures in excess of 75 mbar.

C. System Alignment and Experimental Procedure

Because we were attempting to focus and reproduce sound waves of very high frequency, proper alignment of the source, waveguide, and receiver was critical. The same general assembly procedure was followed for both the short tube and long tube systems. This procedure was satisfactory for alignment of the long tube. However, measurements made in the short tube indicated that not all pulses were optimally focused; so additional adjustments were made for waveform measurements in the short tube.

The general procedure was as follows. First the spark gap and microphone were centered in their respective flange assemblies, and the flanges were bolted onto one of the tubes. Care was taken to make the joints as smooth as possible. Fine adjustment of the microphone in the lateral direction was accomplished by turning the adjustment screws (located on the outside of the receiver assembly) until the recorded pulses were as large in amplitude as possible. For the long tube all pulse amplitudes were maximized when the microphone was located on the axis.

No single alignment of the short tube optimized focusing (maximized pulse amplitude) for all pulses. Apparently, the source and/or receiver was not positioned precisely on the tube axis. In order to obtain accurate measurements in the short tube, we adjusted the lateral microphone placement for each individual reflected wave, thus ensuring that each pulse was optimally focused. This multi-step procedure required that a different spark be used for each observation. An averaging routine, similar to the one discussed in the section on microphone calibration, was used to suppress the variability in pulse amplitude. After the

alignment was optimized for a particular pulse, twenty waveforms, whose associated spark discharge voltages were restricted to a specified narrow range, were captured in the oscilloscope memory. The average peak amplitude was then computed, and the spark source was allowed to discharge repeatedly until an "average waveform" having the same amplitude as the computed mean was received. Average waveforms were transcribed from the oscilloscope point by point and typed into a computer for plotting at a later time. Results obtained using this method were more consistent and, presumably, more accurate than those obtained from a single spark discharge.

D. Preliminary Results: Sample Waveforms

Waveforms measured in the long and short tubes were presented in Chapter I (see Figs. 1.2, 1.3). Recall that the spark energy was 0.16 J, and the microphone remained stationary as it received an entire series of pulses. It is likely that not all of the individual pulses in the short tube waveforms [Figs. 1.2(b), 1.3] are optimally focused.

The direct N wave and the first four reflected pulses, measured in the short tube according to the special short tube alignment procedure outlined in Section C above, are shown in Fig. 2.5. The ubiquitous averaging procedure was used to reduce the results of twenty measurements for each n to a single "average waveform." The spark voltage was 1.0 ±0.1 kV.

Peak sound pressures of the direct and reflected signals were large enough to motivate a test for nonlinear propagation distortion. The test results proved negative, however. The breakdown voltage was reduced (the spark gap shortened) so that the peak pressure of the direct wave was reduced from 3.25 mbar to 1.0 mbar. The shapes of the reflected

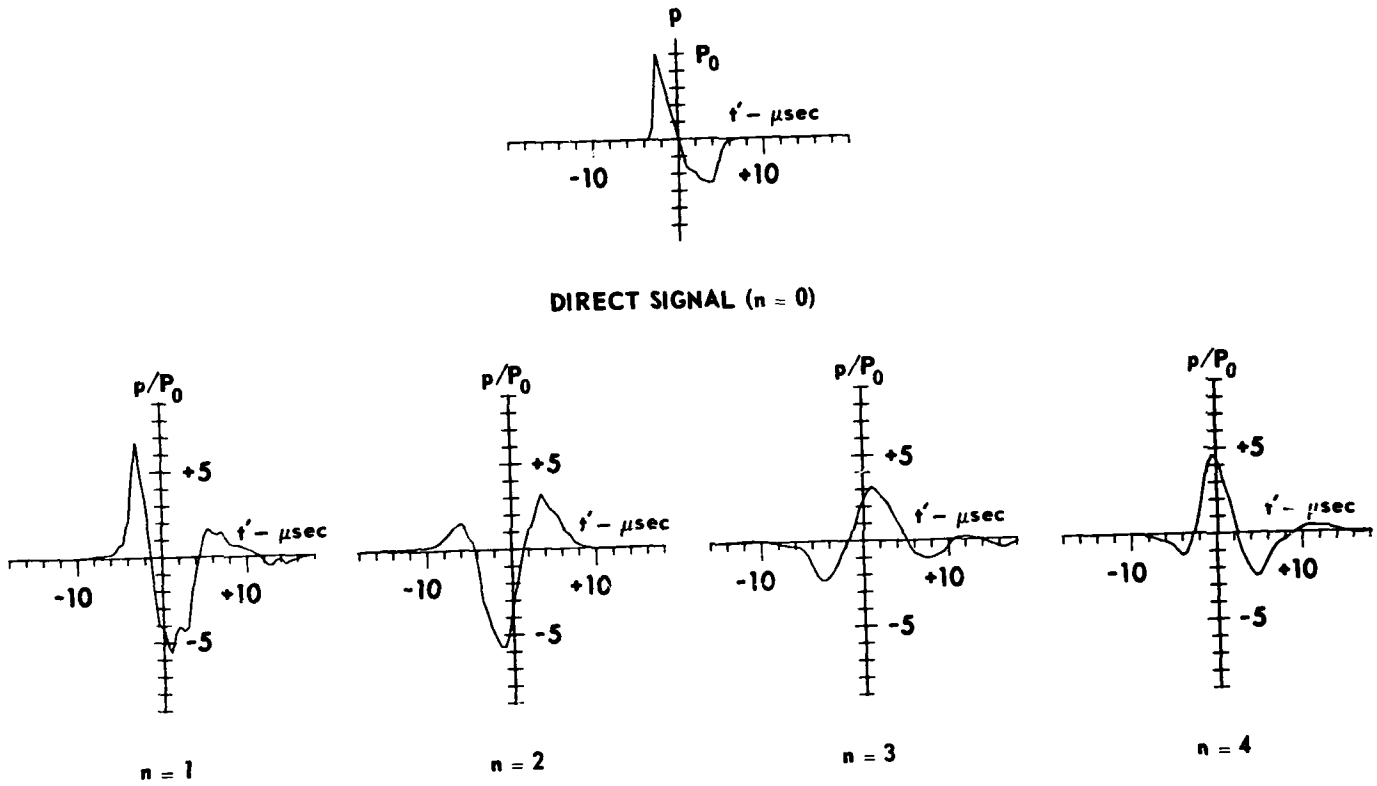

FIGURE 2.5
MEASURED WAVEFORMS, SHORT TUBE
SPARK ENERGY = 0.04 J
P_0 = 3.25 mbar

ARL:UT
AS-80-1156
RDE-GA
5-12-80
REV 6-16-80

pulses remained basically unchanged; we are therefore confident that nonlinear propagation distortion is of little consequence in the 1 kV (0.04 J) data. Since (as will be shown in Chapter III) the wave amplitude decreases as it propagates down the tube, it is assumed that distortion is also negligible in the long tube, for a 0.04 J spark. Still, propagation distortion may be significant at higher source levels. Consider, for example, the waveform for a 0.16 J spark in the short tube (see Fig. 1.3). The second reflected pulse has a (negative) peak pressure amplitude of 55 mbar. Waves of such high amplitude may become distorted over very short distances. Clearly, nonlinear effects in this problem merit serious consideration.

Further experimental results are presented later in this work. Low amplitude waveforms are compared with theoretical predictions in Chapter IV. Measurements of high amplitude pressure fields in the tube are discussed in Chapter V.

CHAPTER III

THEORETICAL ANALYSIS

In this chapter a mathematical analysis of the experiment is given. The tube is modeled as a rigid cylindrical waveguide of infinite length, the spark as a point source. An approximate form of the inhomogeneous thermoviscous wave equation is solved by Fourier transform methods. The result is a frequency domain expression for the pressure field as a sum of direct and reflected signals. Focusing and refocusing of the reflected waves on the axis cause a cumulative phase shift, which sequentially alters the shapes of the received waveforms. An explicit solution for the time waveform received on-axis is determined analytically for the special case in which (i) the medium is lossless and nondispersive, (ii) the microphone is an ideal point receiver, and (iii) the source signal is an ideal N wave. Finally, the effects of finite receiver size and atmospheric absorption are included in the frequency-domain solution, and the reflected pulse time waveforms are computed by application of a digital fast Fourier transform (FFT) routine. Waveforms determined from the analytical results are presented in this chapter, while results from the digital computations are delayed until Chapter IV.

A. Mathematical Formulation of the Problem

The experiment is analyzed mathematically as a boundary-value problem. The tube is considered a rigid boundary, infinite in length, and the spark is assumed to be a point source located on the tube axis. The medium, air, is a relaxing, thermoviscous (i.e., viscous, heat conducting) fluid. Sound propagation is assumed to obey the linear

thermoviscous wave equation. Molecular relaxation, which causes dispersion and absorption, is omitted from the initial statement of the problem. Dispersion is small enough to be neglected. Absorption, on the other hand, which depends on frequency, humidity, temperature, and ambient pressure, is important and must be included in the analysis. It is accounted for ad hoc: After the problem is solved for a nonrelaxing fluid, the effects of relaxation absorption are simply added to the result. First, however, the inhomogeneous, thermoviscous wave equation is derived from the inhomogeneous equation for a lossless medium and the homogeneous equation for a thermoviscous medium.

The linear homogeneous wave equation for a lossless fluid is

$$\nabla^2 p - c_o^{-2}\, p_{tt} = 0 \quad , \tag{3.1}$$

where $p=p(\vec{R},t)$ is the acoustic pressure, $\vec{R}$ is the vector propagation path, c_o is the small-signal sound speed, and subscript t denotes differentiation with respect to time. The solution of Eq. (3.1) for spherically symmetric outgoing waves is

$$Rp = f(t-R/c_o) \quad , \tag{3.2}$$

where f is an arbitrary function of its argument and $R\equiv|\vec{R}|$. The pressure radiated from a point source located at $R\equiv 0$ satisfies the following inhomogeneous wave equation:[39]

$$\nabla^2 p - c_o^{-2}\, p_{tt} = -4\pi\, f(t)\, \delta(\vec{R}) \quad , \tag{3.3}$$

where δ is the Dirac delta function and f satisfies the homogeneous equation, Eq. (3.1), as above. If the amplitude and time dependence of the pressure at radius R_o are defined by P_o and N(t), respectively, then we may write

$$f(t-R_o/c_o) = R_o P_o \, N(t-R_o/c_o) \quad . \tag{3.4}$$

Furthermore, if we let $R_o \to 0$ and $P_o \to \infty$ in such a way that the product $R_o P_o$ remains constant, then we obtain

$$f(t-R_o/c_o) \to f(t) = R_o P_o \, N(t) \qquad (R_o \to 0) \quad .$$

The inhomogeneous wave equation for a lossless fluid containing a point source may now be expressed thus:

$$\nabla^2 p - c_o^{-2} \, p_{tt} = -4\pi P_o R_o \, N(t) \, \delta(\vec{R}) \quad . \tag{3.5}$$

The linear, homogeneous wave equation for propagation in a thermoviscous gas is[†,40]

$$\nabla^2 p - \frac{1}{c_o^2} \, p_{tt} + \left[\frac{\lambda + 2\mu}{\mu} + \frac{\gamma - 1}{Pr}\right] \frac{\mu}{\rho_o c_o^2} \, \nabla^2 p_t = 0 \quad , \tag{3.6}$$

where

λ and μ are the dilatational and shear coefficients of viscosity, respectively,

γ is the ratio of specific heats,

Pr is the Prandtl number, and

ρ_o is the ambient density.

It is assumed that the point source expression derived for the lossless medium and given by the right hand side (RHS) of Eq. (3.5) is also

---

[†]Note that Eq. (3.6) is approximate; thermal and viscous terms have been combined.

applicable in the case of a thermoviscous medium. The inhomogeneous, thermoviscous wave equation is therefore

$$\nabla^2 p - \frac{1}{c_o^2} p_{tt} + \frac{\nu\Gamma}{c_o^2} \nabla^2 p_t = -4\pi P_o R_o \, N(t) \, \delta(\vec{R}) \quad , \tag{3.7}$$

where

$\nu = \mu/\rho_o$ is the kinematic viscosity, and

$\Gamma = \dfrac{\lambda + 2\mu}{\mu} + \dfrac{\gamma - 1}{Pr}$.

Let us now specialize Eq. (3.7) to our particular boundary value problem. We choose an axisymmetric cylindrical coordinate system in r and x [see Fig. 3.1(a)]; then we have

$$p = p(r,x,t) \quad ,$$

and

$$\nabla^2 = \frac{1}{r}\frac{\partial}{\partial r}\left(r \frac{\partial}{\partial r}\right) + \frac{\partial^2}{\partial x^2} \quad .$$

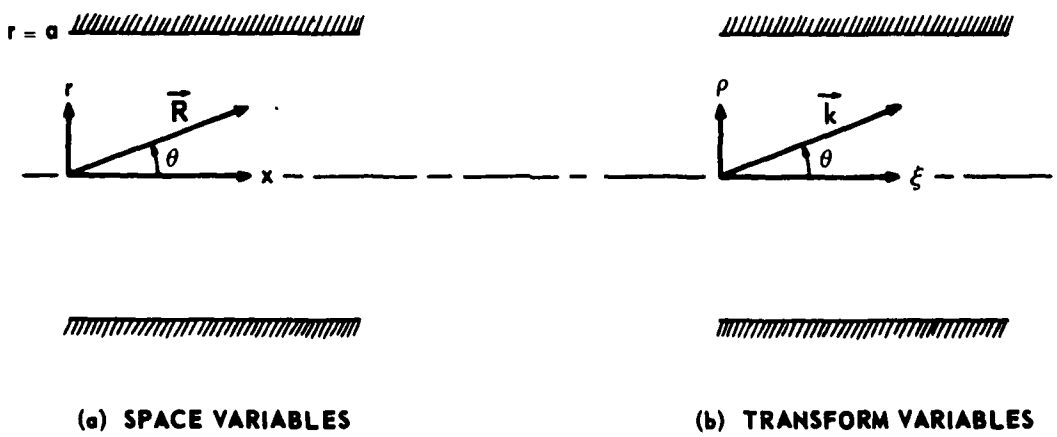

FIGURE 3.1
AXISYMMETRIC COORDINATE SYSTEM

ARL:UT
AS-80-1363
RDE-GA
7-8-80

Noting that by definition the integral of $\delta(\vec{R})$ over all space is equal to unity, one may easily verify that the axisymmetric delta function located at r=0, x=0 is given by†

$$\delta(\vec{R}) = \frac{\delta(r)\ \delta(x)}{\pi r} \quad . \tag{3.8}$$

Finally, the linear thermoviscous wave equation, with a point source of amplitude $P_o R_o$ and time dependence N(t), is

$$\nabla^2 p - \frac{1}{c_o^2} p_{tt} + \frac{\nu\Gamma}{c_o^2} \nabla^2 p_t = -4P_o R_o\ N(t)\ \frac{\delta(r)\ \delta(x)}{r} \quad . \tag{3.9}$$

Our experimental system is bounded by a rigid tube of finite length. One end is terminated by the rigid microphone baffle, the other end by an absorptive fiberglass plug. Forward traveling waves are reflected once by the baffle and then absorbed by the fiberglass; backward traveling waves are absorbed directly. The microphone actually senses each wavefront more than once. First the "primary" wave sweeps across the baffle. Then a "secondary" reflected signal, generated by the incident wave at the junction of the baffle and the tube wall, sweeps back across the baffle. When the reflected wave again reaches the tube wall, it in turn generates a twice-reflected wave, and so on. It turns out that the secondary waves reflected from the baffle/tube junction are of little consequence. They appear as noise between or added to the primary pulses.

---

† Note that $\int_0^\infty \delta(r)\,dr = \frac{1}{2}$, because the radial coordinate r cannot be negative.

Although they have some effect on the measurements, we choose, for the sake of simplicity, to neglect their presence in our theoretical analysis. Hence, the waves of interest (the primary waves) are equivalent to the waves that would be observed in an infinitely long tube. The simpler case, an infinitely long tube of radius a, is chosen for our mathematical model. Boundary conditi s are given as follows:

$$p \text{ finite at } r = 0 \text{ (in the absence of sources)} \tag{3.10a}$$

$$p_r = 0 \text{ at } r = a \text{ (rigid wall condition)} \tag{3.10b}$$

$$p_x = 0 \text{ at } r = a \text{ (no slip condition).} \tag{3.10c}$$

where subscripts denote partial differentiation. Since we have decided to neglect boundary layer absorption, we will neglect the axial boundary condition, Eq. (3.10c), and retain only conditions (3.10a) and (310b).

Our method of solution hinges on the fact that only in the radial direction is there a boundary; both x and t are infinite in domain. Fourier transform techniques are used to reduce Eq. (3.9) to an ordinary differential equation in r. The boundary conditions Eqs. (3.10a,b) are then applied, and finally the inverse transforms are performed.

B. <u>Fourier Transform $t \to \omega$, $x \to \xi$</u>

Let P be the Fourier transform of p with respect to time,

$$P(r,x,\omega) = \mathfrak{F}[p(r,x,t)] \equiv \int_{-\infty}^{\infty} p(r,x,t)\, e^{-j\omega t}\, dt \quad . \tag{3.11}$$

If we transform Eq. (3.9) according to Eq. (3.11), we find that P is a solution of the inhomogeneous Helmholtz equation†

$$\nabla^2 P + k^2 P = -4P_o R_o \; F(\omega) \; \frac{\delta(r)\;\delta(x)}{r} \quad , \tag{3.12a}$$

in which

$$k^2 = \left(\omega/c_o\right)^2 \Big/ \left(1 + j\omega\nu\;\Gamma/c_o^2\right) \tag{3.12b}$$

and

$$F(\omega) = \mathcal{F}\,[N(t)] \Big/ \left(1 + j\omega\nu\;\Gamma/c_o^2\right) \quad . \tag{3.12c}$$

We may similarly define the Fourier transform of P with respect to the axial coordinate x by

$$\bar{P}(r,\xi,\omega) = \int_{-\infty}^{\infty} P(r,x,\omega)\; e^{j\xi x}\; dx \quad . \tag{3.13}$$

Transforming Eq. (3.12a), we obtain an inhomogeneous form of Bessel's equation of order zero

$$\frac{1}{r}\left(r\bar{P}_r\right)_r + \rho^2\bar{P} = -4P_o R_o \; F(\omega)\; \frac{\delta(r)}{r} \quad , \tag{3.14}$$

where the radial wave number ρ is defined in terms of the axial wave number ξ by $\rho^2 = k^2 - \xi^2$. The transformed boundary conditions are

$\bar{P}$ finite at $r = 0$ [for the homogeneous solution of Eq. (3.14)] , (3.15a)

$\bar{P}_r = 0$ at $r = a$. (3.15b)

---

†It can be seen by inspection that if other agencies of dissipation, e.g., relaxation, are included in the original wave equation (3.9), the expressions for k and F would have been more complicated. Such a possibility is considered in Section E.

The propagation constants ξ and ρ may be thought of as the projections of the vector wave number $\vec{k}$ on the axis and the source plane, respectively. If θ is the angle $\vec{k}$ makes with the axis, then $\xi = k \cos\theta$ and $\rho = k \sin\theta$ [see Fig. 3.1(b)].

C. Solution of the Radial Equation

The general solution of Eq. (3.14) is the sum of a particular solution $\bar{P}_p$, which satisfies the inhomogeneous equation, Eq. (3.14), and a complementary solution $\bar{P}_c$, which satisfies the associated homogeneous equation. The total solution must satisfy the boundary conditions on $\bar{P}$ at r=a and r=0. The complementary solution may be written at once:

$$\bar{P}_c = A\, H_o^{(1)}(\rho r) + B\, H_o^{(2)}(\rho r) \quad ,$$

where $H_o^{(1)}(z)$ and $H_o^{(2)}(z)$ are zero order Hankel functions of the first and second kinds, respectively, and A and B are constants to be determined from the boundary conditions.

The inhomogeneous equation has a singularity at the point r=0. We now proceed to determine a Green's function solution which has the correct behavior near the origin, as well as in the farfield. Our method closely follows that of Morse and Feshbach [Ref. 41, pp. 808-811]. Let $G(\vec{r})$ be the solution of the following dimensionless form of Eq. (3.14):

$$\nabla^2 G + \rho^2 G = -4\pi\, \delta(\vec{r}) \quad . \tag{3.16}$$

In the present case, the axisymmetric, two-dimensional Laplacian and the radial delta function are defined by

$$\nabla^2 = \frac{1}{r}\frac{\partial}{\partial r}\left(r\frac{\partial}{\partial r}\right)$$

$$\delta(\vec{r}) = (2/r)\, \delta(r) \quad , \quad r = |\vec{r}| \quad .$$

It is evident that, since the source is omnidirectional, the behavior of G for small $|\vec{r}|$ must also be omnidirectional, i.e.,

$$G(\vec{r}) \to g(r) \qquad (|\vec{r}| \to 0) \quad .$$

First let us integrate Eq. (3.16) over a small circular area of radius ε. Since the integral of the delta function is unity, we have

$$\int_A \nabla^2 G \, dA + \rho^2 \int_A G \, dA = -4\pi \quad . \tag{3.17}$$

In the limit of vanishingly small ε, we may replace G with g. If it is assumed that the Laplacian of a singularity is more singular than the singularity itself, the second integral may be neglected, and we are left with

$$\int_A \nabla^2 g \, dA = -4\pi \qquad (\varepsilon \to 0) \quad . \tag{3.18}$$

Next, Gauss' theorem is employed to transform the area integral into a line integral around the perimeter of the circle,

$$\oint_C \nabla g \cdot d\vec{r} = -4\pi \qquad (\varepsilon \to 0) \quad . \tag{3.19}$$

Since g depends only on r, $\nabla g = g_r$ is everywhere parallel to $d\vec{r}$. We can now solve for the behavior of g near the origin by evaluating the line integral,

$$2\pi r \, g_r = -4\pi \qquad (\varepsilon \to 0) \quad ,$$

or

$$g(r) = -2\ln(r) \qquad (r \to 0) \quad . \tag{3.20}$$

Apparently, we were justified in neglecting the area integral of g.

Since Eq. (3.14) is a form of Bessel's equation whose RHS denotes a source, we wish to find a Bessel-type solution for outgoing

waves that has a logarithmic singularity at r=0. In fact, the zero order Hankel function for outgoing waves has the required properties [see, for example, Ref. 41, pp. 890-891]:

$$H_o^{(2)}(z) \to \frac{-2j}{\pi} \ln(z) \qquad (|z| \to 0) \quad , \tag{3.21a}$$

$$H_o^{(2)}(z) \to \left(\frac{2}{\pi z}\right)^{1/2} \exp[-j(z-\pi/4)] \qquad (|z| \to \infty) \quad . \tag{3.21b}$$

Hence, the particular solution of Eq. (3.14) is†

$$\bar{P}_p = -j\pi P_o R_o \; F(\omega) \; H_o^{(2)}(\rho r) \quad . \tag{3.22}$$

The general solution is given by the sum of $\bar{P}_c$ and $\bar{P}_p$, i.e.,

$$\bar{P} = A \; H_o^{(1)}(\rho r) + B \; H_o^{(2)}(\rho r) - j\pi P_o R_o \; F(\omega) \; H_o^{(2)}(\rho r) \quad , \tag{3.23}$$

and the boundary conditions, Eqs. (3.15). The behavior required by Eq. (3.15a) is already satisfied by the third term on the RHS of Eq. (3.23). The first two terms must therefore cancel each other as $r \to 0$. The small argument behavior of $H_o^{(2)}(\rho r)$ is given by Eq. (3.21a). Similarly, $H_o^{(1)}(\rho r)$ behaves thus:

$$H_o^{(1)}(\rho r) \to \frac{2j}{\pi} \ln(\rho r) \qquad (|\rho r| \to 0) \quad .$$

The first boundary condition therefore becomes

$$A \ln \rho r - B \ln \rho r = 0 \qquad (r \to 0) \quad ,$$

or

$$B = A \quad . \tag{3.24}$$

---

†Had the forcing function on the RHS of Eq. (3.16) been $4\pi\delta(\vec{r})$ instead of $-4\pi\delta(\vec{r})$ (i.e., a "sink" instead of a source), the correct solution would have been the Hankel function for incoming waves $j\pi P_o R_o F(\omega) H_o^{(1)}(\rho r)$.

The pressure is

$$\bar{P} = A\left[H_o^{(1)}(\rho r)+H_o^{(2)}(\rho r)\right] - j\pi P_o R_o\ F(\omega)\ H_o^{(2)}(\rho r) \quad . \tag{3.25}$$

The matching coefficient A is determined from the boundary condition at the tube wall. Substituting Eq. (3.25) into Eq. (3.15b), we obtain

$$A = \frac{2\pi j P_o R_o\ F(\omega)}{1 + \left[H_1^{(1)}(\rho a)/H_1^{(2)}(\rho a)\right]} \quad . \tag{3.26}$$

The transformed pressure $\bar{P}(r,\xi,\omega)$ is completely determined by Eqs. (3.25) and (3.26). Noting that

$$J_m(z) = \frac{1}{2}\left[H_m^{(1)}(z)+H_m^{(2)}(z)\right] \quad , \tag{3.27}$$

we find for the exact solution,

$$\bar{P} = P_o R_o\ F(\omega)\left\{- j\pi H_o^{(2)}(\rho r) + 2\pi j J_o(\rho r)\left[1 + H_1^{(1)}(\rho a)\Big/H_1^{(2)}(\rho a)\right]^{-1}\right\} . \tag{3.28}$$

Alternatively, the expression for A may be expanded as a power series

$$A \approx -2\pi j P_o R_o\ F(\omega) \sum_{n=1}^{\infty} (-1)^n\left[H_1^{(2)}(\rho a)\Big/H_1^{(1)}(\rho a)\right]^n \quad . \tag{3.29}$$

Then Eq. (3.25) assumes the form

$$\bar{P} = P_o R_o\ F(\omega)\left\{-j\pi H_o^{(2)}(\rho r) + 2\pi j J_o(\rho r) \sum_{n=1}^{\infty} (-1)^n\left[H_1^{(2)}(\rho a)\Big/H_1^{(1)}(\rho a)\right]^n\right\} . \tag{3.30}$$

No technique has been found by which to calculate the exact inverse transform of $\bar{P}$. We must therefore make some sort of approximation

prior to attempting the inversion. One approach is to invoke the short wavelength assumption upon which any "geometric acoustics" model is based. Specifically, we require that $|\rho a| >> 1$. The validity of this assumption will be investigated later. Here it is sufficient to note that the range of $|ka|$ important to the present problem lies above 5. Given the large argument behavior of the Hankel functions,

$$H_m^{(1)}(z) \sim \left(\frac{2}{\pi z}\right)^{1/2} e^{j[z-(2m+1)\pi/4]} \qquad (|z| >> m)$$

$$H_m^{(2)}(z) \sim \left(\frac{2}{\pi z}\right)^{1/2} e^{-j[z-(2m+1)\pi/4]} \qquad (|z| >> m) \quad ,$$

one may easily show that

$$\frac{H_1^{(2)}(\rho a)}{H_1^{(1)}(\rho a)} \sim -j\ e^{-j2\rho a} \qquad (|\rho a| >> 1) \quad . \tag{3.31}$$

This relation is substituted into Eq. (3.30) to yield the following approximate solution for the transformed pressure:

$$\bar{P} = P_o R_o\ F(\omega)\left[-j\pi H_o^{(2)}(\rho r) + 2\pi J_o(\rho r) \sum_{n=1}^{\infty} j^{n-1}\ e^{-j2n\rho a}\right] \quad . \tag{3.32}$$

At this stage in the analysis, a correspondence between the experimental and theoretical results becomes apparent. The first term in Eq. (3.32) can be recognized as the direct wave; it is the only term with a singularity at r=0. It turns out that the terms in the series represent the sequence of reflected signals observed at the microphone. The presence of the factor j^{n-1} indicates that the phase changes by $\pi/2$ from one reflected signal to the next. The implication of the factor $\exp(-j2n\rho a)$ is

that the distance traveled increases with n. We shall return to this point in the analysis after a brief digression, in which Eq. (3.30) is rederived via a more physical approach, the method of images.

D. Alternative Derivation of the Guided Pressure Field--The Method of Images [see Ref. 41, pp. 812-816]

The guided pressure field may be built up as a superposition of waves that originate at ring-shaped image sources and propagate in an unbounded medium (see Fig. 3.2). Let the microphone (M) be located a distance L from the real source. The image sources lie in the plane x=0, and their radii r_n are integer multiples of the tube diameter, i.e., $r_n=2na$. All of the ring sources "fire" simultaneously, but the waves emitted are not all the same. Indeed, the relative amplitude and phase of the signals emitted by each pair of adjacent rings is determined from the boundary condition at r=a. For r<a the field produced by the image waves is the same as the actual reflected field.

Each of the signals emitted by the image sources corresponds to a real wavefront that is confined by the tube. For example, the signal originating at the first image source S_1 corresponds to the wave that is reflected once from the tube wall at the point r=a, x=L/2 (denoted by A_{11} in Fig. 3.2). In fact, the real and image waves coincide on the ray segment $\overline{A_{11}M}$. Like the real wave, the image wave focuses at the microphone; the angle of incidence is denoted by θ_1. The wave emitted by the second image source S_2 corresponds to a wave that is reflected at the points A_{21} (r=a, x=L/4) and A_{22} (r=a, x=3L/4). Between reflections the real wave passes through an intermediate focus, labeled O_1. The reflected wave and the second image wave meet at A_{22} and impinge on the microphone at angle

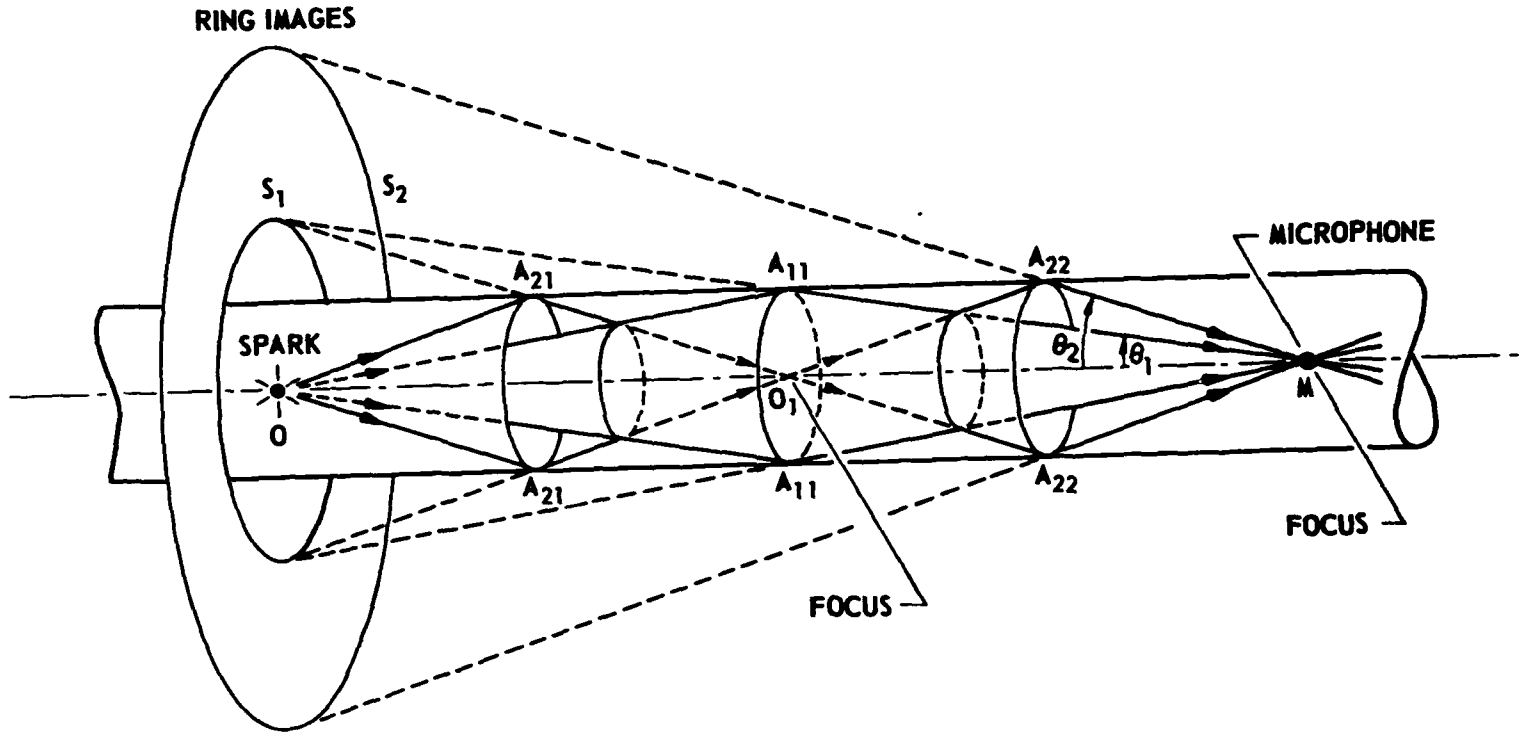

FIGURE 3.2
REAL AND IMAGE SOURCES

θ_2. The twice-reflected wave and the first image wave intersect at A_{21}. In general, the nth arrival after the direct wave undergoes n reflections and passes through n-1 foci before it reaches the receiver, and at each reflection point A_{ni} (i=1,2,...,n) the nth reflected wave meets the ith image wave. Both leave the point A_{ni} at angle θ_n with respect to the axis, focus at O_i, and diverge to $A_{n(i+1)}$. There, the ith image wave continues to diverge, but the bounded wave takes the value of the (i+1)th image wave. The nth reflected wave travels along the path of each image wave (i=1,2,...,n) in succession until it reaches the microphone.

The total signal received at the microphone is equal to the sum of the signals received from the real source and from the ring sources. The transformed pressure may be written in the form

$$\bar{P}(r) = B_o\psi_o(r) + \sum_{n=1}^{\infty} B_n\psi(r) \quad , \tag{3.33}$$

where $\psi=\psi_{in}+\psi_{out}$ denotes the behavior of the incoming and outgoing image waves in the radial direction, and the B_n are constants to be determined from the boundary conditions. The first term (n=0) corresponds to the direct wave, and the rest of the series (n>0) corresponds to the sequence of image waves. The functions ψ_{in} (incoming waves) and ψ_{out} (outgoing waves) are solutions of the inhomogeneous form of Bessel's equation, Eq. (3.14). It has already been shown that the solutions for incoming and outgoing waves are proportional to $H_o^{(1)}(\rho r)$ and $H_o^{(2)}(\rho r)$, respectively, and that the direct wave is given by the particular solution of Eq. (3.14), i.e.,

$$B_o\psi_o = -j\pi P_o R_o \; F(\omega) \; H_o^{(2)}(\rho r) \quad . \tag{3.34}$$

The boundary conditions at r=0 and r=a are used to determine the coefficients B_n and the function ψ. The particle velocity must vanish at r=a; alternatively, the pressures of the incoming and outgoing waves must be equal there. Consider the case n=1. At the point A_{11} the wave diverging from O meets the wave converging from S_1. The outgoing pressure wave is of the form $B_o H_o^{(2)}(\rho r)$, and the incoming wave is $B_1 H_o^{(1)}(\rho r)$. Equating the pressures at r=a, we find that the signals emitted by the first ring source and the real source are related by

$$B_1/B_o = H_o^{(2)}(\rho a)/H_o^{(1)}(\rho a) \quad .$$

Similar use of the boundary condition at A_{22} results in an expression that relates the waves emitted by the first and second ring sources,

$$B_2/B_1 = H_o^{(2)}(\rho a)/H_o^{(1)}(\rho a) \quad ,$$

whence

$$B_2/B_o = \left[H_o^{(2)}(\rho a)/H_o^{(1)}(\rho a)\right]^2 \quad .$$

In general the signal originating at the nth image source is related to the signal leaving the real source by

$$B_n/B_o = \left[H_o^{(2)}(\rho a)/H_o^{(1)}(\rho a)\right]^n \quad . \tag{3.35}$$

Since both incoming and outgoing waves are present in the tube, ψ must be a linear combination of $H_o^{(1)}(\rho r)$ and $H_o^{(2)}(\rho r)$. The only such combination that satisfies both of the boundary conditions is

$$\psi = H_o^{(1)}(\rho r) + H_o^{(2)}(\rho r) \quad ,$$

or, by Eq. (3.27),

$$\psi = 2J_o(\rho r) \quad . \tag{3.36}$$

Substituting Eqs. (3.34), (3.35), and (3.36) into Eq. (3.33), we obtain for the pressure

$$\tilde{P} = - P_o R_o F(\omega) \left\{ j\pi H_o^{(2)}(\rho r) + 2\pi j J_o(\rho r) \sum_{n=1}^{\infty} \left[H_o^{(2)}(\rho a)/H_o^{(1)}(\rho a) \right]^n \right\} \quad , \tag{3.37}$$

which may, with a little algebra, be put in the form of Eq. (3.30), section C.

E. <u>Inverse Fourier Transform $\xi \to x$: Method of Stationary Phase</u>

Having found a solution in r subject to the boundary conditions at r=a and r=0, we now compute the inverse Fourier transform $\xi \to x$ to recover the pressure as a function of space and frequency. The inverse transform of Eq. (3.32) is

$$P(r,x,\omega) = P_o R_o \; F(\omega)(-j/2) \int_{-\infty}^{\infty} H_o^{(2)}\left[r\left(k^2-\xi^2\right)^{1/2} \right] e^{-j\xi x} \, d\xi + \sum_{n=1}^{\infty} P_n \quad , \tag{3.38a}$$

where

$$P_n = P_o R_o \; F(\omega) \; j^{n-1} \int_{-\infty}^{\infty} J_o\left[r\left(k^2-\xi^2\right)^{1/2} \right] \exp\left[-j\xi x - j2na\left(k^2-\xi^2\right)^{1/2} \right] d\xi \quad . \tag{3.38b}$$

Evaluation of the first integral in Eq. (3.38a) yields the following expression for the direct wave:

$$P_o R_o \; F(\omega) \; \frac{e^{-jkR}}{R} \quad ,$$

where

$$R = \left(x^2+r^2\right)^{1/2} \quad .$$

In order to compute P_n we make the substitution $\xi = k\cos\theta$, where θ is the angle between the propagation vector k and the tube axis [see Fig. 3.1(b)] and $0 \le \theta \le \pi$. With this change of variables Eq. (3.38b) becomes

$$P_n = P_o R_o F(\omega)\, j^{n-1} \int_0^{\pi} e^{-jk(x\cos\theta + r_n \sin\theta)} J_o(kr\sin\theta) k \sin\theta \, d\theta \quad , \tag{3.39}$$

where $r_n \equiv 2na$. The expression for P_n contains an integral of the general form

$$I = \int_a^b f(\theta)\, e^{k\beta(\theta)}\, d\theta \quad ,$$

where $\mathrm{Im}[k\beta] \neq 0$ and $\mathrm{Re}[k\beta] < 0$ (recall that $\mathrm{Im}[k] < 0$). This integral is now evaluated for values of $|k\beta| >> 1$ by the method of stationary phase. For a concise description of the method the reader is referred to the work of Sneddon.[42] Observation points very close to the axis are considered first; later the case of off-axis points is treated.

Let us assume $\mathrm{Im}[k\beta]$ is large enough that $\exp[k\beta(\theta)]$ varies much faster than $f(\theta)$. Then the integrand oscillates rapidly over most of the domain of integration. However, when θ is equal to θ_n, which satisfies the equation

$$\beta'(\theta_n) = 0 \quad , \tag{3.40}$$

the exponential is constant. For this reason θ_n is called a "stationary point" of the integrand. It turns out that for large values of $|k\beta|$ the dominant contribution to the integral is accrued in the immediate vicinity of θ_n. The result of the integration is[†]

[†] There is an error in Sneddon's final calculation. The integral $\int_{-\infty}^{\infty} e^{-u^2} du$ is equal to $\sqrt{\pi}$.

$$I = e^{k\beta(\theta_n)} f(\theta_n)\left[-2\pi/k\beta''(\theta_n)\right]^{1/2} \qquad (|k\beta| \to \infty) \quad . \tag{3.41}$$

The amplitude and phase functions specific to our problem are

$$f(\theta) = k \sin\theta \, J_o(kr \sin\theta)$$

and

$$\beta(\theta) = -j(r_n \sin\theta + x \cos\theta) \quad .$$

Both f and β oscillate rapidly when $|k\beta|$ is large. In the present problem kr_n and kx are much larger than kr. The assumption that $\exp[k\beta(\theta)]$ varies more rapidly than $f(\theta)$ is therefore valid. Separate consideration of the integrand for $0 \leq \theta \leq \pi/2$ and $\pi/2 < \theta \leq \pi$ leads to a solution of Eq. (3.40) that defines two stationary points. For values $0 \leq \theta \leq \pi/2$, which implies that the receiver is located at a range $x>0$, there is one stationary point, defined by

$$\theta_n = \tan^{-1} \frac{r_n}{x} \quad . \tag{3.42}$$

Equations (3.41) and (3.42) are used to reduce Eq. (3.39) to

$$P_n(r,x,\omega) = P_o R_o \, F(\omega)(2\pi jk)^{1/2} \, j^{n-1} \, R_n^{-1/2} \sin\theta_n \, J_o(kr \sin\theta_n) \, e^{-jkR_n} \quad , \tag{3.43}$$

where $R_n = \left(x^2+r_n^2\right)^{1/2}$, and $j^{1/2} = e^{j\pi/4}$.

In essence, the method of stationary phase is a vehicle by which we can determine the trajectory θ_n of each reflected wave and the contribution P_n of each reflected wave to the total signal received by the microphone. Although the source radiation is uniform in all directions, only those rays for which $\theta=\theta_n$ [given by Eq. (3.42)] contribute appreciably to the received signal.

The implications of Eq. (3.43) are most interesting. The nth reflected wave travels a total distance R_n, which is the distance between the receiver and the nth image source (see Fig. 3.3). The signal is diminished by cylindrical spreading and atmospheric absorption over the entire travel distance. At the same time, its amplitude varies with r according to the Bessel function factor. The amplitudes of successive reflections increase as $\sin\theta_n$, and as has been noted, the phase lag increases in increments of $\pi/2$.

Consider the functional dependence of P on k as $r \to 0$. The Bessel function tends to a constant, and the wave number appears only in the

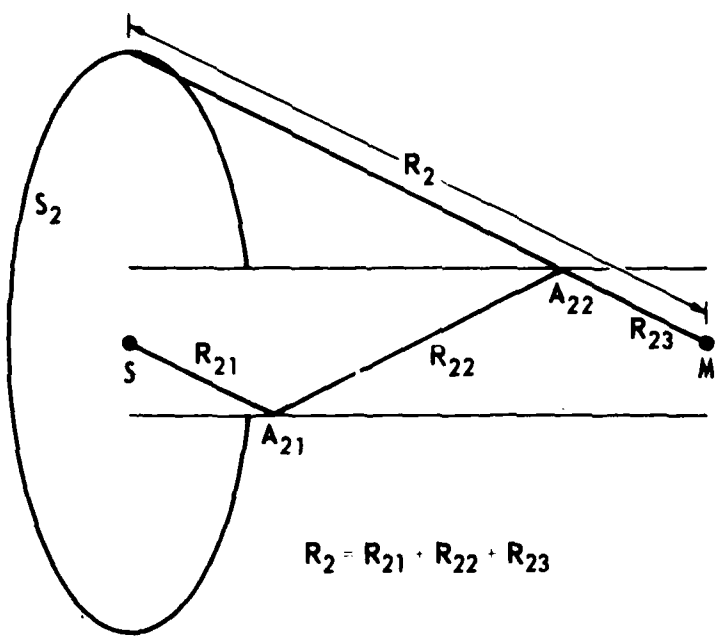

FIGURE 3.3
TRAVEL PATHS OF REAL AND IMAGE WAVES
n 2

factor $(jk)^{1/2}$. Here the relationship between spherical and cylindrical focusing is brought to light. It is well known that the waveform that exists at the focus of a three-dimensional mirror is equal to the derivative of the convergent reflected signal (see, for example, Cornet, Ref. 25). The Fourier transform of the derivative of a function g(R) is given by

$$\mathfrak{F}\left[\frac{\partial}{\partial R}\, g(R)\right] = jk\, G(k) \qquad ,$$

where R is the distance from the focus, and G(k) is the Fourier transform of g(R). Blackstock[43] has described an analogous "half-derivative" operator whose Fourier transform has the following property:

$$\mathfrak{F}\left[\frac{\partial^{1/2}}{\partial R^{1/2}}\, g(R)\right] = (jk)^{1/2}\, G(k) \qquad .$$

One may thus speculate that a general focusing factor for the transform space is expressed by $(jk)^{\iota}$, where $\iota = 1/2$ for two-dimensional waves and $\iota = 1$ for three-dimensional waves.

When the observation point is far enough off-axis that $kr \sin\theta \gg 1$ (which requires $r \gg 0.3$ cm when f = 30 kHz and $\theta = \theta_1$ in the long tube), the stationary phase integration must be redone because the phase information in the Bessel function must be included in $k\delta$. Consider the integral solution given by Eq. (3.39). The Bessel function may be replaced by its large argument, asymptotic expansion

$$J_o(z) \sim (2\pi z)^{-1/2}\left[e^{j(z-\pi/4)} + e^{-j(z-\pi/4)}\right] \qquad (|z| \gg 1) \qquad .$$

Then Eq. (3.39) becomes

$$P_n = P_o R_o F(\omega)\ j^{n-1} (2\pi j r)^{-1/2}$$

$$\times \int_o^{\pi} \left\{ e^{-jk[x\cos\theta + (r_n - r)\sin\theta]} \right.$$

$$\left. + j\ e^{-jk[x\cos\theta + (r_n + r)\sin\theta]} \right\} (k\ \sin\theta)^{1/2}\ d\theta \quad .$$

The integral is evaluated by the method of stationary phase. The two terms in the integrand have different stationary points θ_{n1} and θ_{n2}, respectively, given by

$$\tan\theta_{n1} = \frac{r_n - r}{x} = \tan\theta_n - \frac{r}{x}$$

$$\tan\theta_{n2} = \frac{r_n + r}{x} = \tan\theta_n + \frac{r}{x} \quad .$$

The result for the pressure is

$$P_n = P_o R_o F(\omega)\ j^{n-1}\ r^{-1/2}$$

$$\times \left[\left(\frac{\sin\theta_{n1}}{R_{n1}} \right)^{1/2} e^{-jkR_{n1}} + j \left(\frac{\sin\theta_{n2}}{R_{n2}} \right)^{1/2} e^{-jkR_{n2}} \right] \quad , \qquad (3.44)$$

where

$$R_{n1} = (x\ \cos\theta_{n1} + (r_n - r)\ \sin\theta_{n1})$$

$$R_{n2} = (x\ \cos\theta_{n2} + (r_n + r)\ \sin\theta_{n2}) \quad .$$

The RHS of Eq. (3.44) represents a sum of pre-focus and post-focus waves (see Fig. 3.4). The focusing factor $(jk)^{1/2}$ found in Eq. (3.43) is not present in the off-axis solution. Instead there is an amplitude dependence of $r^{-1/2}$.

For small values of r/x and r/r_n, it can be seen that $\tan\theta_{n1} \simeq \tan\theta_{n2} \simeq \tan\theta_n$ and, furthermore, that $R_{n1} \simeq R_{n2} \simeq R_n$. Under such conditions Eq. (3.44) may be rewritten in the form

$$P_n = P_o R_o \; F(\omega) \; j^{n-1} \left(r r_n\right)^{-1/2} \sin\theta_n \left[e^{-jk(R_n - R')} + j \; e^{-jk(R_n + R')} \right] . \tag{3.45}$$

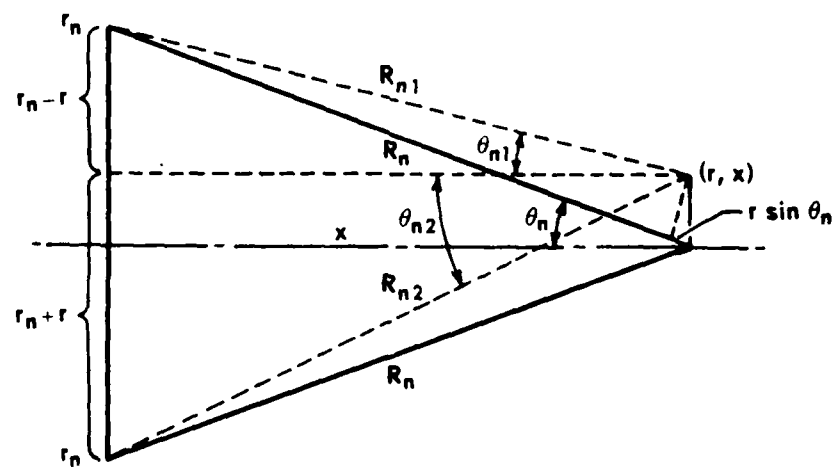

FIGURE 3.4
OFF-AXIS GEOMETRY

Now let us determine the importance of the fact that k is complex. The main effect of Im[k] is to produce attenuation of the waves as they travel along their respective rays. For waves traveling away from the source, the complex wave number may be expressed thus:

$$k = \omega/c_o - j\alpha(\omega) = (\omega/c_o)(1-j\alpha c_o/\omega) \quad , \tag{3.46}$$

where use has been made of the fact that the phase velocity is very nearly equal to c_o for f << 100 MHz. The absorption coefficient $\alpha(\omega)$ includes the effects of viscosity, heat conduction, and molecular relaxation. For the frequencies of interest, $\alpha(\omega) \ll \omega/c_o$. Equation (3.46) is now introduced into Eq. (3.43). The complete expression for k as given above is substituted directly into the phase delay term $\exp(-jkR_n)$. The two factors $\exp(-j\omega R_n/c_o)$ and $\exp(-\alpha R_n)$ thus obtained represent phase delay and attenuation, respectively, over the path length R_n. Since Im[k]<<Re[k] we neglect Im[k] in the argument of the Bessel function.

Next consider the dependence of $k^{1/2}F(\omega)$ on $\alpha(\omega)$:

$$k^{1/2}\ F(\omega) = \left(\frac{\omega}{c_o}\right)^{1/2} \mathfrak{F}[N(t)]\left(1+j\ \frac{\omega\nu\Gamma}{c_o^2}\right)^{-1}\left(1 - j\ \frac{c_o\alpha(\omega)}{\omega}\right)^{1/2}$$

$$\simeq \left(\frac{\omega}{c_o}\right)^{1/2} \mathfrak{F}[N(t)]\left[1 - \frac{\nu\Gamma\alpha}{2c_o} - j\left(\frac{c_o\alpha}{2\omega} + \frac{\omega\nu\Gamma}{c_o^2}\right) + \ldots\right] \quad ,$$

where terms of greater than first order in $c_o\alpha/\omega$ and $\nu\omega/c_o^2$ have been neglected inside the brackets. For f < 1 MHz only the first term in the brackets is appreciable. The following substitution is therefore made in Eq. (3.43):

$$k^{1/2}\, F(\omega) = \left(\omega/c_o\right)^{1/2} \mathfrak{F}[N(t)] \qquad (f < 1 \text{ MHz}) \quad .$$

The general solution for the pressure field now assumes the form

$$P(r,x,\omega) = P_d + \sum_{n=1}^{\infty} P_n \quad , \tag{3.47a}$$

where

$$P_d = \frac{P_o R_o}{R} \mathfrak{F}[N(t)]\, e^{-jkR} \quad , \tag{3.47b}$$

$$P_n = P_o R_o \left(\frac{2\pi j\omega}{c_o}\right)^{1/2} j^{n-1}\, R_n^{-1/2} \sin\theta_n\, J_o\left(\frac{\omega}{c_o}\, r \sin\theta_n\right) \mathfrak{F}[N(t)]\, e^{-jkR_n} \quad , \tag{3.47c}$$

and k is given by Eq. (3.46).

The approximate frequency domain solution given by Eqs. (3.47) is valid under the assumptions that $|ka| >> 1$ and $f < 1$ MHz. For our tube ($a = 2.54$ cm) these conditions are roughly equivalent to $2 \times 10^4 < f < 10^6$ Hz. The solution is valid for <u>any</u> signal, broadband or pure tone, whose spectrum falls principally in this frequency range.

F. <u>Inverse Fourier Transform $\omega \to t$: Analytical Evaluation</u>

Under certain conditions the inverse Fourier transform of Eqs. (3.47) can be calculated analytically. The inversion formula is

$$p(r,x,t) = \frac{1}{2\pi} \int_{-\infty}^{\infty} P(r,x,\omega)\, e^{j\omega t}\, d\omega \quad . \tag{3.48}$$

As a first approximation to the measurement conditions it is assumed that the medium is lossless [$\alpha(\omega)=0$] and the microphone is an ideal point receiver (microphone radius$\to$0). The pressure signal p_d corresponding to

the direct wave is readily obtained. Substitution of Eq. (3.47b) into Eq. (3.48) yields

$$p_d(r,x,t) = \frac{P_o R_o}{R} N(t-R/c_o) \quad , \tag{3.49}$$

a result that is valid both on and off the axis. Calculation of the reflected signals p_n is somewhat more difficult. First, the pulse waveforms that would be measured by a point receiver on the axis (i.e., at a focus) are computed; then the results are compared with computed off-axis waveforms.

We wish to find the on-axis time waveform for the nth reflected wave by evaluating the inverse Fourier transform of Eq. (3.47c) for r=0. Setting r=0 and rearranging terms, we can write Eq. (3.47c) in the form

$$P_n = P_o R_o \sin\theta_n \left(2/c_o R_n\right)^{1/2} j^{n-1} (\pi/j\omega)^{1/2} j\omega \mathcal{F}[N(t)] e^{-j\omega R_n/c_o} \quad . \tag{3.50}$$

We first proceed to find the inverse transform of

$$j^{n-1} (\pi/j\omega)^{1/2} j\omega \mathcal{F}[N(t)]$$

as a function of t, and then note that if we include the factor $\exp(-j\omega R_n/c_o)$, the result is unchanged except for a time shift $t \to t-R_n/c_o \equiv t'$ (t' is the retarded time).

Notice that the phase shift factor j^{n-1} is real for odd n and imaginary for even n. In particular,

$$j^{n-1} = (-1)^{(n-1)/2} \quad , \quad n \text{ odd} \quad ,$$

$$j^{n-1} = j(-1)^{(n-2)/2} \quad , \quad n \text{ even} \quad .$$

Moreover, in order for p_n (n even) to be a real function of time, the 90° phase shift j must be interpreted as +j for positive frequencies and as -j for negative frequencies, or vice versa (this fact is proved in Appendix A). In other words, let

$$j \rightarrow j\ \mathrm{sgn}(\omega) \quad ,$$

where

$$\mathrm{sgn}(\omega) \equiv \begin{cases} 1 & , \quad \omega > 0 \\ 0 & , \quad \omega = 0 \\ -1 & , \quad \omega < 0 \end{cases} \quad .$$

Now consider the function

$$G_n(\omega) = j^{n-1}\ (\pi/j\omega)^{1/2}\ j\omega\, \mathfrak{F}[N(t)] \quad . \tag{3.51}$$

It is convenient to write the inverse Fourier transform of $G_n(\omega)$ as a convolution of time functions. The following transform pairs are used:

$$(\pi/j\omega)^{-1/2} \leftrightarrow t^{-1/2}$$

$$j\omega\, \mathfrak{F}[N(t)] \leftrightarrow N'(t)$$

$$j\ \mathrm{sgn}(\omega) \leftrightarrow -(\pi t)^{-1} \quad .$$

For odd values of n Eq. (3.51) takes the form

$$G_n(\omega) = (-1)^{(n-1)/2}(\pi/j\omega)^{1/2}\, j\omega\, \mathfrak{F}[N(t)] \quad ,$$

whose inverse Fourier transform is given in integral form by

$$\mathfrak{F}^{-1}[G_n(\omega)] = (-1)^{(n-1)/2} \int_{-\infty}^{\infty} (t-\tau)^{-1/2}\ N'(\tau)\ d\tau \quad . \tag{3.52}$$

If we introduce the dimensionless times $\phi = t/T_o$ and $\tau' = \tau/T_o$, where T_o is a characteristic time, then Eq. (3.52) becomes

$$\mathcal{F}^{-1}[G_n(\omega)] = (-1)^{(n-1)/2}\, T_o^{-1/2}\, \Lambda_1(\phi) \quad (n \text{ odd}) \quad , \tag{3.53a}$$

where

$$\Lambda_1(\phi) = \int_{-\infty}^{\infty} \frac{N(\tau')}{\sqrt{\phi - \tau'}}\, d\tau' \quad . \tag{3.53b}$$

For even values of n Eq. (3.51) takes the form

$$G_n(\omega) = (-1)^{(n-2)/2}\, j\, \mathrm{sgn}(\omega)\, (\pi/j\omega)^{1/2}\, j\omega\, \mathcal{F}[N(t)] \quad , \tag{3.53c}$$

and its inverse transform is

$$\mathcal{F}[G_n(\omega)] = (-1)^{n/2}\, T_o^{-1/2}\, \Lambda_2(\phi) \quad (n \text{ even}) \quad , \tag{3.54a}$$

where

$$\Lambda_2(\phi) = \frac{1}{\pi T_o} \int_{-\infty}^{\infty} \frac{\Lambda_1(\phi)}{\phi - \tau'}\, d\tau' \quad . \tag{3.54b}$$

Finally, we use the time shift property of the Fourier transform

$$\mathcal{F}[A(t)]\, e^{-j\omega R_n/c_o} \leftrightarrow A(t - R_n/c_o) \quad ,$$

where A is an arbitrary function, to obtain the on-axis pressure

$$p_n(0,x,t) = P_o R_o \left(2/c_o T_o R_n\right)^{1/2} \sin\theta_n\, (-1)^{(n-1)/2}\, \Lambda_1(\phi) \quad (n \text{ odd}) \tag{3.55a}$$

$$p_n(0,x,t) = P_o R_o \left(2/c_o T_o R_n\right)^{1/2} \sin\theta_n\, (-1)^{n/2}\, \Lambda_2(\phi) \quad (n \text{ even}) \quad , \tag{3.55b}$$

where now ϕ denotes the dimensionless retarded time

$$\phi = t'/T_o \quad . \tag{3.55c}$$

Up to this point the two functions Λ_1 and Λ_2 are perfectly general, since N(t) has not yet been defined. Regardless of the waveform, it may be observed that (1) the amplitude depends on $R_n^{-1/2} \sin\theta_n$, which is a function of the tube radius and the receiver location, and (2) there is a 180° phase shift every time n changes by 2. The 90° phase shift between consecutive arrivals, given in the frequency domain as j sgn(ω), is manifested in the time domain as a convolution with $-1/\pi T_o \phi$ [see Eq. (3.54b)].

To illustrate the changes in shape and amplitude suffered by a small-signal N wave, we evaluate p_n for the ideal N wave function

$$N(t) = -(t/T_o)\ \mathrm{rect}[t/2T_o] \quad , \tag{3.56}$$

where T_o is the half-duration and

$$\mathrm{rect}[t/2T_o] \equiv \begin{cases} 1 \ , & |t| < T_o \\ 0 \ , & |t| > T_o \\ 1/2 \ , & |t| = T_o \end{cases} \quad .$$

In terms of the retarded time ϕ, N is given by

$$N(\phi) = -\phi\ \mathrm{rect}[\phi/2] \quad , \tag{3.57}$$

and the derivative of N by

$$N'(\phi) = -\frac{1}{T_o}\ \mathrm{rect}\ [(\phi-1)/2] + \delta(\phi-1) + \delta(\phi+1) \quad . \tag{3.58}$$

Because $N(\phi)$ is discontinuous at $\phi=\pm 1$, each of the integrals defining Λ_1 and Λ_2 must be evaluated over the three regions $\phi<-1$, $-1<\phi<1$, and $\phi>1$. Substituting Eq. (3.58) into Eqs. (3.53b) and (3.54b), we obtain

$$\Lambda_1(\phi) = \begin{cases} 0 \quad , & \phi < -1 \\ (\phi+1)^{-1/2} - 2(\phi+1)^{1/2} \quad , & -1 < \phi < 1 \\ (\phi-1)^{-1/2} + (\phi+1)^{-1/2} + 2(\phi-1)^{1/2} - 2(\phi+1)^{1/2} \quad , & \phi > 1 \quad , \end{cases} \tag{3.59a}$$

and

$$\Lambda_2(\phi) = \begin{cases} (-1-\phi)^{-1/2} + (1-\phi)^{-1/2} + 2(-1-\phi)^{1/2} - 2(1-\phi)^{1/2} \quad , & \phi < -1 \\ (1-\phi)^{-1/2} - 2(1-\phi)^{1/2} \quad , & -1 < \phi < 1 \\ 0 \quad , & \phi > 1 \quad . \end{cases} \tag{3.59b}$$

The solution for the pressure signal $p_n(0,x,t)$ is given by Eqs. (3.55) and (3.59).

Pressure waveforms corresponding to the first four reflected pulses in the short tube ($x = 0.074$ m) are plotted in Fig. 3.5. The direct arrival is an ideal N wave whose half-duration is 4.0 μsec and whose peak pressure amplitude is P_o at the receiver (for simplicity we have chosen $R_o=x$). The amplitudes of the computed waveforms have been normalized with respect to P_o. It is immediately apparent that the focusing process produces waveforms differing considerably in shape and amplitude from the direct N wave. First of all, in each reflected wave the amplitude is infinite at $\phi=\pm 1$. We should expect the pressure to be limited in a real medium by finite amplitude effects and absorption. Because for our particular geometry the amplitude factor $\sin\theta_n/R_n^{1/2}$ varies little over the range $1 \leq n \leq 4$, the amplitudes of the four pulses are nearly the same. Finally, it is most interesting to observe that each pulse has either a precursor

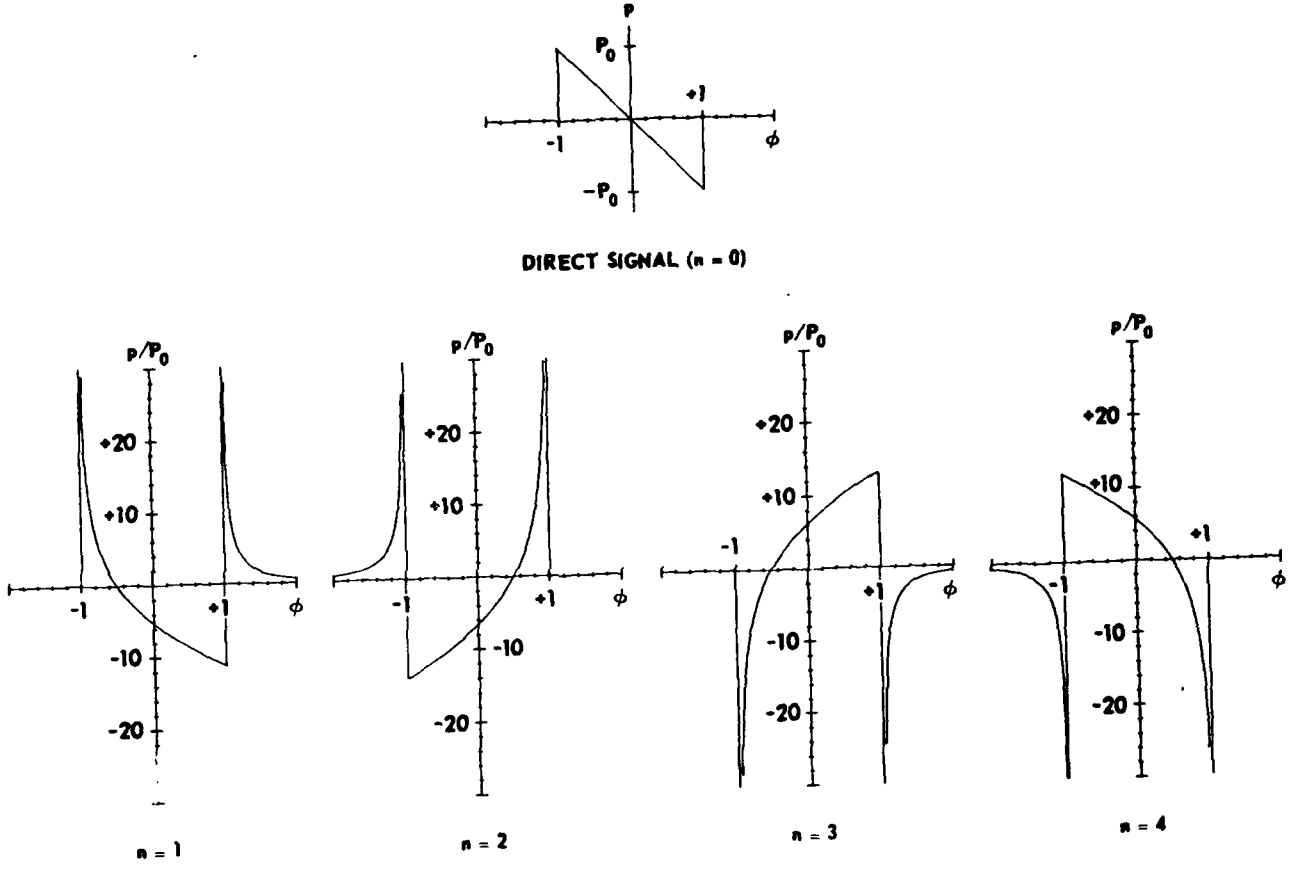

FIGURE 3.5
CALCULATED ON-AXIS WAVEFORMS FOR A LOSSLESS MEDIUM
DIRECT SIGNAL IS AN IDEAL N WAVE
$\phi = t/T_0$

ARL:UT
AS-80-1157
RDE-GA
5-12-80
REV 6-16-80

or a tail. Nonzero pressure is predicted for either $\phi < -1$ or $\phi > 1$, depending on n. Even-numbered waveforms have precursors and odd-numbered waveforms have tails. It will presently be shown that at off-axis receiver positions every pulse has a precursor and a tail.

The off-axis solution given by Eq. (3.45) is a good approximation if $kr \sin\theta_n >> 1$. Let us now calculate the inverse transform of Eq. (3.45). We observe that the signal at (r,x) is composed of an incoming wave, which crosses the axis at some position $x_{in} > x$, and an outgoing wave, which has already passed through a focus at $x_{out} < x$. Consider the wave corresponding to n=1. The incoming signal is an N wave, and the outgoing signal is shifted by $\pi/2$ radians. Recall that a phase shift of $\pi/2$ corresponds to convolution with $-1/\pi t$. If the time dependence of the incoming signal is

$$N(\phi) = -\phi \text{ rect}[\phi/2] \quad ,$$

then the outgoing signal is proportional to

$$N_{\pi/2}(\phi) = -\pi^{-1} \int_{-\infty}^{\infty} (\phi-\tau)^{-1} N(\tau)\, d\tau$$

$$= \frac{1}{\pi}\left(\phi \ln\left|\frac{\phi+1}{\phi-1}\right| - 2\right) \quad , \qquad (3.60)$$

where $\mathfrak{F}[N_{\pi/2}] = j\,\mathfrak{F}[N]$. Now consider the off-axis waveforms associated with the signal identified by n=2. An observer sees a pre-focus wave proportional to $N_{\pi/2}$ followed by a post-focus wave proportional to N_{π}, i.e., an inverted N wave. Similar arguments may be advanced to determine the waveforms for each pair of ray paths corresponding to the general index n.

The effect of a pure phase lag on an ideal N waveform is illustrated in Fig. 3.6 for phase lags equal to integer multiples of $\pi/4$.

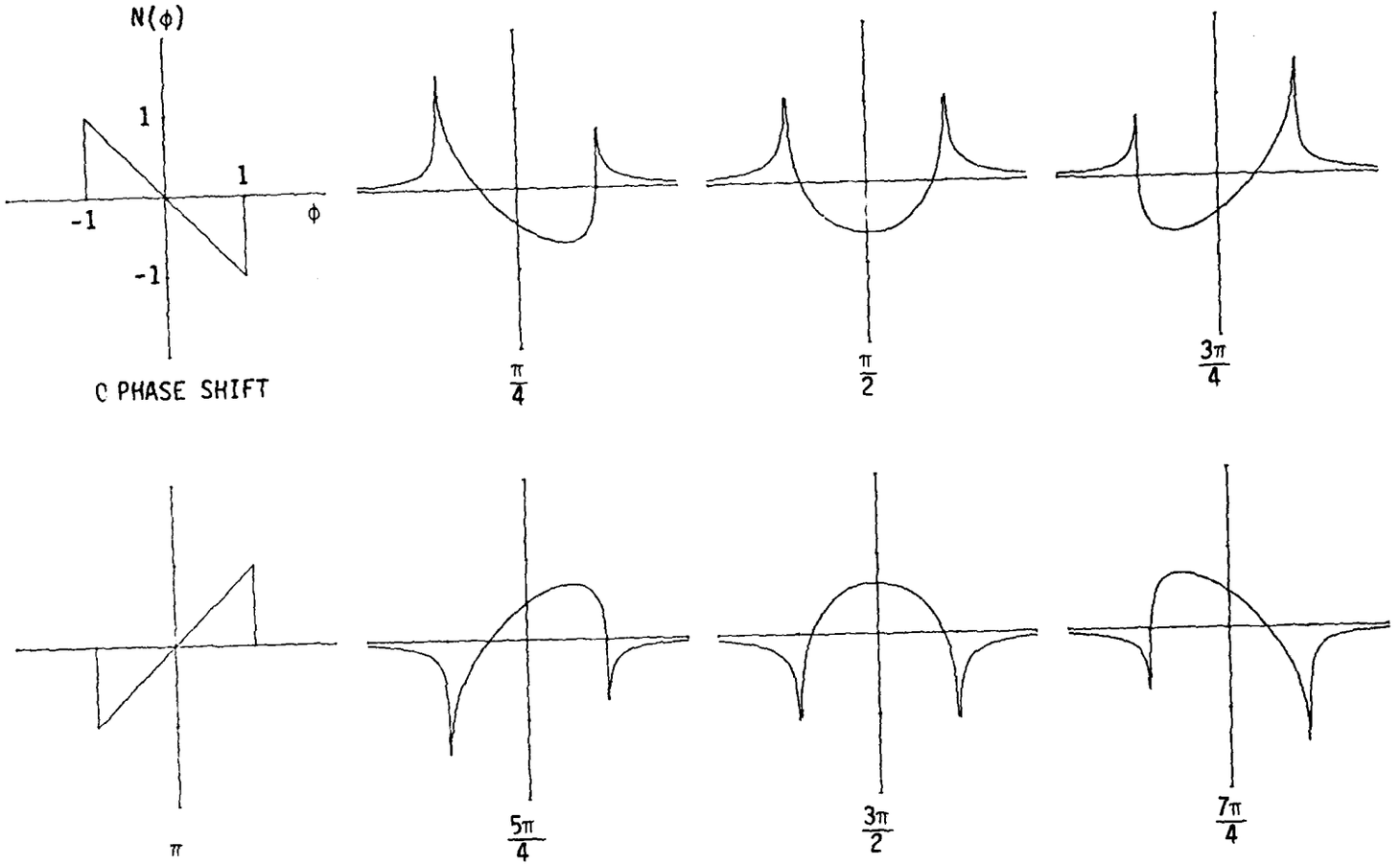

FIGURE 3.6

IDEAL N WAVE AFTER SUCCESSIVE PHASE SHIFTS

The odd multiples are included for comparison with the on-axis waveforms (see Fig. 3.5). Noting that

$$\exp(j\pi/4)\,\mathfrak{F}[N] = 2^{-1/2}(1 + j)\,\mathfrak{F}[N] = 2^{-1/2}\,\mathfrak{F}[N + N_{\pi/2}] \ ,$$

one sees that waveforms computed for the odd multiples of $\pi/4$ are just scaled superpositions of N and $N_{\pi/2}$. In every case both precursor and tail exist and are symmetric about the origin. Although the figure may seem to indicate otherwise, the amplitude is infinite at $\phi=\pm 1$. There are, however, no jump discontinuities like those present in the on-axis waveforms; the signal increases (or decreases) smoothly to ∞ (or $-\infty$).

It is not really appropriate to compare the measured waveforms presented in Fig. 2.5 with the waveforms predicted here. Recall that in the interest of simplicity medium losses were neglected and the microphone was assumed to be a point receiver. Furthermore, the direct signal was taken to be an ideal N wave, small enough in amplitude that nonlinear distortion could be neglected throughout the tube. In the following section, atmospheric absorption and microphone directivity are included in a computer routine developed to calculate more realistic waveforms.

G. Inverse Fourier Transform $\omega \to t$: Digital Evaluation

In this section, a computer routine is developed which, given the asymptotic solution in the frequency domain, Eqs. (3.47), enables one to calculate and plot the reflected waves for an arbitrary direct waveform.[†] The effects of atmospheric absorption and microphone

[†]The direct waveform cannot be completely arbitrary. It must still satisfy the limitations on ka which were noted at the beginning of the previous section.

directivity are included in the calculation. Results for both ideal and measured direct N wave inputs are presented in Chapter IV.

1. Receiver of Finite Dimensions. Let us consider what happens to the observed waveforms when the receiver is a baffled piston of finite size (recall that our microphone is baffled to avoid the problem of diffraction from the edge of the housing; see Section A.3, Chapter II). A pressure front incident on the face of the microphone at an angle $\theta>0$ takes a short time to traverse the active area. The instantaneous output of the microphone is proportional to the integral of the instantaneous pressure over the entire active area. Calculation of this integral in the time domain is entirely equivalent to calculation of the frequency directivity characteristic in the frequency domain. We pursue the latter course for the case in which the pressure field is symmetric about the axis of the piston.

An axisymmetric pressure field incident on the microphone face at angle θ referred to the axis may be expressed in the form

$$P(r,x,\omega) = P_o J_o(kr \sin\theta)\, e^{jkx \cos\theta} \quad . \tag{3.61}$$

The voltage output of the transducer is proportional to the average pressure $\hat{P}$ on the face, which is, for a microphone of radius σ,

$$\hat{P} = \frac{1}{\pi\sigma^2} \int_0^\sigma P(r,0,\omega)\, 2\pi r\, dr$$

$$= P_o \frac{2J_1(k\sigma \sin\theta)}{k\sigma \sin\theta} \equiv P_o D(\theta) \quad . \tag{3.62}$$

Thus, it turns out that the directivity function $D(\theta)$ is the same as that of a piston in a plane wave field.

Now the axisymmetric reflected wave field described by Eq. (3.47c) is of the form postulated in Eq. (3.61). Integrating Eq. (3.47c) with respect to r, one may conclude that if a baffled microphone of radius σ is used to sense the pressure on the axis of the tube, the pressure response $\hat{P}$ to the nth reflected pulse will be

$$\hat{P}_n(0,x,\omega) = P_o R_o \, \mathfrak{F}[N(t)] \, (2\pi j)^{1/2} \, j^{n-1} \, (kR)^{-1/2} \, (2/\sigma) \, J_1(k\sigma \sin\theta_n) \, e^{-jkR_n}$$

$$= P_n(0,x,\omega) \, D(\theta_n) \quad , \tag{3.63}$$

where P_n and $D(\theta)$ are given by Eqs. (3.47c) and (3.62), respectively. This exceedingly simple result suggests that one may account for the finite size of the microphone by multiplying the on-axis, frequency domain solution by the microphone directivity factor $D(\theta_n)$. If the microphone is not centered on the axis, $D(\theta)$ must be expressed as a sum of higher order Bessel functions, and the result for the pressure is not so simple.

2. Atmospheric Absorption. The effects of absorption and dispersion on the propagating signal were introduced in Section E. There it was argued that the complex wave number k could be written

$$k = (\omega/c_o) - j\alpha(\omega) \quad , \tag{3.64}$$

where absorption α includes relaxation as well as thermoviscous effects. Recently, the American National Standards Institute (ANSI) published a "Standard Method for the Calculation of the Absorption of Sound by the Atmosphere" (Ref. B.1), by which one can compute α for given frequency, ambient temperature, ambient pressure, and relative humidity. A digital implementation of the method is stored in the user library at

Applied Research Laboratories, The University of Texas at Austin, under the function name ABSORP.

Extensive experimental and theoretical documentation pertaining to the atmospheric absorption of small-signal N waves is presented in Appendix B. There a digital method is developed which allows one to compute the attenuation of broadband signals according to the ANSI absorption. Comparison of computed and measured N waveforms reveals excellent agreement for the range of travel path lengths R_n encountered in the tube experiment. Appendix B also includes an analytical approximation for α, valid at very high frequencies, and an analytical solution for an attenuated ideal N waveform based on that approximation. It was hoped that a method similar to that used in Appendix B could be incorporated into the analysis for focused, ideal N waves advanced in Section F of this chapter, but when a straightforward approach failed, this method of attack was shelved.

3. Program NTUBE. The computer program NTUBE computes waveforms detected by a piston microphone centered on the axis of the tube. The effects of both atmospheric absorption and microphone directivity are included in the program. A simplified flow chart for the program is shown in Fig. 3.7. The input is the direct time waveform $p_d(t')$ received at position x. First the FFT of the input waveform is calculated in order to obtain a frequency domain representatition of the signal $P_d(f_i)$, where f_i is the ith frequency component. Next $\hat{P}_n(x,f_i)$ is computed according to Eqs. (3.62) and (3.47c): The phase of $P_d(x,f_i)$ is shifted by $(n/2 + 1/4)\pi\ \mathrm{sgn}(f_i)$; then the focusing factor $k^{1/2}$ and the microphone directivity and atmospheric absorption factors are computed for each f_i and multiplied by $P_d(x,f_i)$ (absorption is applied over the difference in

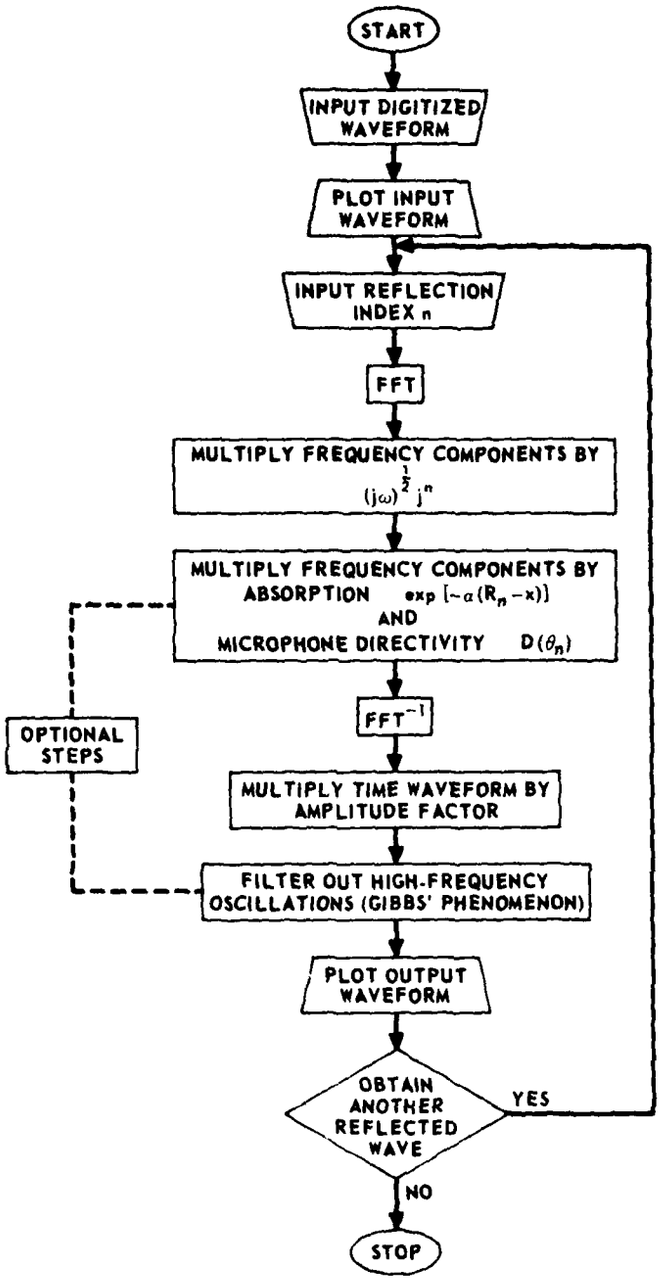

FIGURE 3.7
SIMPLIFIED FLOW CHART OF PROGRAM NTUBE

distance traveled by the direct and reflected waves). The inverse FFT of the resulting signal is computed and multiplied by a frequency-independent amplitude factor to yield the time waveform of the nth pulse. Finally the subroutine PLTWAVE is called to plot the waveform.

The program has been used for ideal as well as measured N wave inputs, although it is applicable to other pulse inputs as well.† The absorption and microphone directivity subroutines are optional so that the digital and analytical solutions for an ideal N wave can be compared under "ideal" propagation and measurement conditions [$\alpha(\omega)=0$, $D(\theta_n)=1$]. Gibbs' phenomenon (see Ref. 41, pp. 745-748) was evident near the discontinuities of computed ideal waveforms. Its amplitude of oscillation was objectionably large, presumably because of the presence of the frequency-dependent gain factor $k^{1/2}$. The oscillations were damped by the time domain filter that precedes the plotting routine. Use of the filter is also optional.

All of the programming was done in FORTRAN on a CDC Cyber Series 170 computer. Listings for Program NTUBE, Subroutine PLTWAVE, and Function ABSORP (which calculates atmospheric absorption at each frequency f_i) are provided in Appendix C. Results for ideal and measured input N waves are presented in the following chapter.

---

†Note that each reflected wave is computed independently; i.e., no attempt is made to superpose several appropriately delayed pulses.

CHAPTER IV

COMPARISON OF EXPERIMENTAL AND THEORETICAL RESULTS: SMALL-SIGNAL WAVES

The computer program NTUBE was used to calculate reflected pulse waveforms. In this chapter results of the calculations are compared with waveforms measured in the tube. First, however, the effects of microphone directivity and atmospheric absorption on ideal waveforms are investigated in order that the relative effect of each on the measured waveforms may be assessed. Then a measured direct N wave is used as an input in waveform computations for the first four reflections in the short tube; atmospheric absorption and microphone directivity are included in the calculations. Measured and predicted wave shapes are in agreement, but the amplitudes of the measured waves are consistently lower than those of the computed waves.

Next, the long time behavior of the mathematical solution is analyzed by computing the "amplitude envelope" discussed in Chapter II. The peak-to-peak pressures of measured and computed pulse waveforms are plotted versus reflection number n for propagation in the long tube. The amplitude discrepancy observed in the comparison of the first four measured and computed waveforms persists throughout the range of n considered (n=1-35). It is postulated that the disparity is due to misalignment of the apparatus, boundary layer losses (which have been neglected in the analysis), nonlinear propagation distortion, or to a combination of all three. Quantitative evidence is given in this chapter that suggests

(1) that a very slight misalignment can cause a discrepancy of the same order as is observed, and (2) that by neglecting boundary layer losses, we probably underestimate total absorption. Discussion of nonlinear distortion is delayed until Chapter V.

Finally, a sample off-axis waveform is presented. Pulses corresponding to pre-focus and post-focus waves are observed.

A. Influence of Absorption and Microphone Directivity on the Pulse Waveforms

The results described in this section include computations of the first four ideal waveforms for cases in which the atmospheric absorption and microphone directivity are significant. Program NTUBE is used to carry out the computations, and the direct signal is an ideal N wave. To begin, however, the relative importance of boundary layer and mainstream absorption effects are briefly discussed.

After giving much thought to the problem of how to include boundary layer absorption in our theory, we decided to dispense with it altogether and include only mainstream absorption. Consider the magnitudes of the plane wave boundary layer absorption α_{BL} and the mainstream absorption α_{MS} (which includes both thermoviscous and relaxation absorption) for frequencies between 10 kHz and 1 MHz. Weston[43] gives solutions of the full Kirchhoff dispersion relation for "narrow", "wide", and "very wide" tubes and for the "transition" regions in between. The sound attenuation in a majority of practical duct acoustics problems is governed by the "wide tube" formula (given first by Kirchhoff)

$$\alpha_{BL} = [1 + (\gamma-1)/\sqrt{Pr}]\left(ac_o\right)^{-1}(\nu\omega/2)^{1/2} \quad . \tag{4.1}$$

The restrictions on Eq. (4.1) are given by Blackstock[39] in terms of the boundary layer thickness $\delta=(2\nu/\omega)^{1/2}$,

$$\frac{\omega}{c_o}\,\delta \ll \frac{\omega a}{c_o} \ll \frac{c_o}{\delta\omega} \quad . \tag{4.2}$$

The meaning of the inequality is that the radius of the tube must be large enough that the boundary layer thickness is a small fraction of the tube radius but the boundary layer absorption is much larger than mainstream absorption. For the present problem a = 2.54 cm and $\nu = 1.5\times10^{-5}$ m^2/sec; the "wide tube" formula is thus valid for frequencies f such that

$$7.6\times10^{-3}\ \text{Hz} \ll f \ll 144\ \text{kHz} \quad . \tag{4.3}$$

The frequencies of interest lie between 10 kHz and 1 MHz. Evidently, the "wide tube" formula is not applicable here.

Our particular problem is best served by Weston's result for attenuation in the "transition" region between the "wide tube" and the "very wide tube",

$$\alpha = \alpha_{MS} + \alpha_{BL} + \alpha_{BL}^{+} \quad , \tag{4.4}$$

where

$$\alpha_{BL}^{+} = \left(1 + \frac{\gamma-1}{\sqrt{Pr}}\right)^2 \frac{\nu\omega^2}{2c_o^3} \quad . \tag{4.5}$$

The term α_{BL}^{+} arises because the fluid is bounded, but it is not clear how α_{BL}^{+} is associated with the boundary layer. Actually, Weston's result is valid for a <u>nonrelaxing</u> thermoviscous fluid (i.e., α_{MS} is the mainstream thermoviscous absorption only). We assume that relaxation absorption does

not depend on the presence of a boundary and, hence, that it may be added to the classical thermoviscous absorption to yield the total mainstream absorption α_{MS}. The three terms α_{MS}, α_{BL}, and α_{BL}^{+} are evaluated for three frequencies in Table IV.1. The terms α_{BL} and α_{BL}^{+} are computed from Eqs. (4.1) and (4.5), respectively, and the values of α_{MS} are obtained from Program ABSORP (see also Fig. B.1, Appendix B). The atmospheric conditions are typical conditions for our laboratory: T=25°C, RH=48%, and p_o = 1.0 atm. For the lowest frequencies α_{BL} is the largest of the three terms, and between 100 kHz and 1 MHz α_{MS} is the most significant term. The extra absorption α_{BL}^{+} is significant only in the higher decade.

TABLE IV.1

CONTRIBUTIONS (Np/m) TO PLANE WAVE ABSORPTION IN "TRANSITIONAL" TUBE

f(Hz)	α_{MS}	α_{BL}	α_{BL}^{+}
10^4	1.45×10^{-2}	1.17×10^{-1}	8.06×10^{-4}
10^5	4.67×10^{-1}	3.74×10^{-1}	8.06×10^{-2}
10^6	18.9	1.17	8.06

Equation (4.4) is valid only for the propagation of plane waves in the tube. We have not been able to extend it to explain the attenuation of higher order modes propagating in the same tube. It seems plausible, however, that the boundary layer absorption terms are collectively of the same order of magnitude as the mainstream absorption, at least for

the first few modes. Boundary layer effects are neglected in the present analysis. As a result the total attenuation of the pulse train is undoubtedly underestimated.

The effects of atmospheric absorption and microphone directivity on computed waveforms were investigated independently to give some indication of the importance of each in the measured waveforms. The direct signal, an ideal N wave with half-duration T_o = 4.0 μsec, was digitized at the rate of 4 points/μsec over the interval $-2.5 \leq \phi \leq 2.5$. The program NTUBE was used to compute the first four reflected pulses in the short tube for the following three cases: (1) lossless medium, point receiver [$\alpha(\omega)=0$, $D(\theta_n)=1$]; (2) atmospheric absorption, point receiver [$\alpha(\omega)$ given by ABSORP, $D(\theta_n)=1$]; (3) lossless medium, finite piston receiver [$\alpha(\omega)=0$, $D(\theta_n)$ given by Eq. (3.62)]. Typical measured values were chosen for the relative humidity RH, temperature T, and ambient pressure p_o, and the receiver radius σ was chosen to equal the radius of the active area of our microphone. Waveforms computed for σ = 1.0 mm, RH=50%, T=25°C, and p_o = 1.0 atm are presented in Fig. 4.1. The amplitude of Gibbs' oscillations have been reduced by means of the time-domain filter routine. The results for case (1) were, except for the presence of some residual Gibbs' oscillations, precisely the same as those plotted directly from the analytical solution (see Fig. 3.5). Hence the analytical results are repeated in the first column of Fig. 4.1.

In Fig. 4.1 one may observe that microphone directivity produces a much more noticeable change in the waveform than does atmospheric absorption. Because later arriving reflections impinge on the microphone at more oblique angles, the distortion due to directivity increases with n.

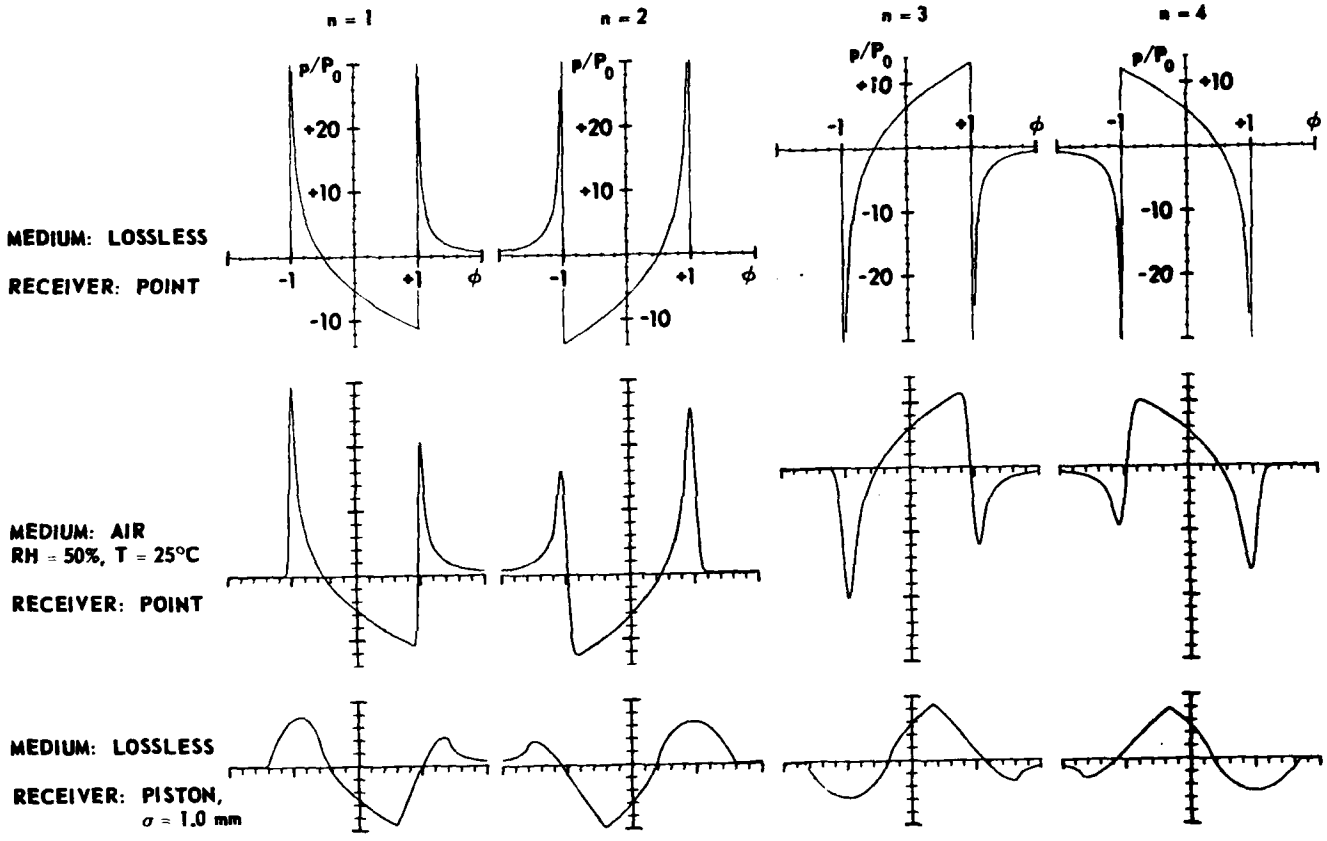

FIGURE 4.1
EFFECTS OF ATMOSPHERIC ABSORPTION AND MICROPHONE DIRECTIVITY ON WAVEFORMS MEASURED ON-AXIS (SHORT TUBE)

DIRECT SIGNAL IS AN IDEAL N WAVE WITH PEAK AMPLITUDE P_0

$\phi = t'/T_0$, $T_0 = 4.0\ \mu sec$

ARL:UT
AS-80-1285
RDE-GA
6-13-80

Total atmospheric absorption likewise increases with n because higher order reflected waves travel greater distances. However, for our specified conditions of humidity, temperature, microphone size, and for our particular tube geometry, microphone directivity is more important than absorption for the first four reflected pulses.†

B. Computer Solution For a Nonideal Input Waveform

We are now ready to present theoretical results that may be directly compared to the measured waveforms shown in Fig. 2.5. The "average" direct N waveform measured in the short tube (spark energy 0.04 J) was digitized at a rate of 2 points/μsec by the digital oscilloscope. Waveforms for the first four reflected pulses were computed by means of Program NTUBE. The effects of atmospheric absorption and microphone directivity were included in the computations. The geometric and atmospheric parameters were assigned their measured values: RH=48%, T=25°C, p_o = 1.0 atm, x = 0.074 m, a = 0.0254 m, and σ = 1.0 mm. Computed waveforms are shown along with corresponding measured waveforms in Fig. 4.2 (the measured waveforms are from Fig. 2.5). The basic shapes of the two sets of waveforms are similar: corresponding peaks and zero crossings are located at nearly the same points in time. In general, however, the peak amplitudes of the measured pulses are less than those of their computed counterparts. It is surmised that the discrepancy has three possible causes: (1) our neglect of possibly significant boundary layer

†This result is not surprising when one realizes that for a large part of our frequency range, a 1 mm radius piston is not an omnidirectional receiver. For example, the 3 dB beamwidth is 62° at 100 kHz and 5° at 1 MHz, and in the short tube the angles θ_{1-4} are 34°, 54°, 64°, and 70°, respectively.

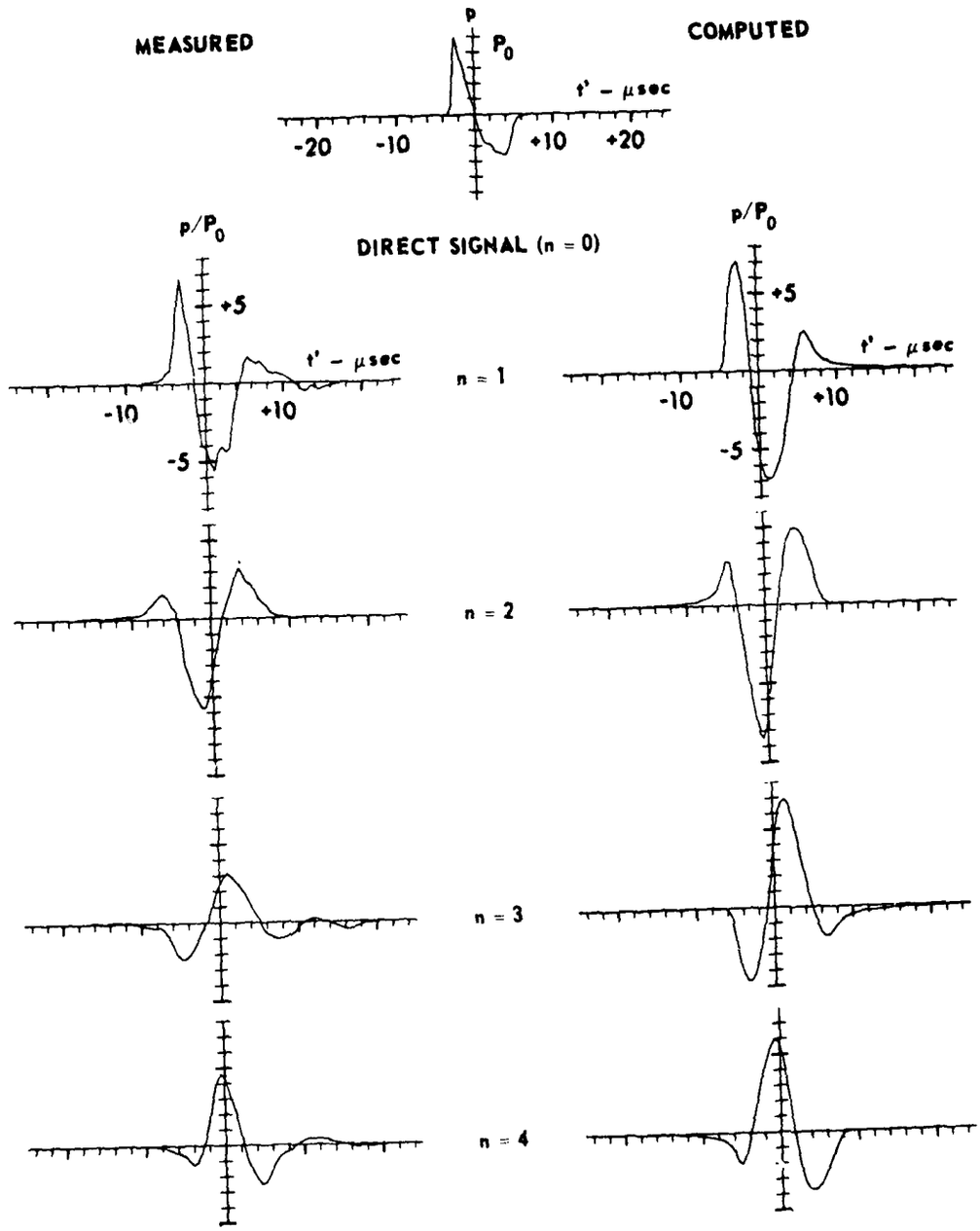

FIGURE 4.2
COMPARISON OF MEASURED AND COMPUTED WAVEFORMS
SHORT TUBE

SPARK ENERGY = 0.04 J
P_0 = 3.25 mbar

ARL:UT
AS-80-1286
RDE-GA
6-13-80

losses, (2) apparatus misalignment, which tends to defocus the waves, (3) nonlinear propagation distortion, which causes excess attenuation of the waveforms (over and above geometric spreading and atmospheric absorption).† The first possible cause has been explored already. We were unable to come up with a quantitative estimate of the error introduced by neglecting boundary layer absorption. The latter two possibilities are discussed in the present and subsequent chapters.

Let us for the moment argue that the difference in amplitude between measured and computed waveforms is primarily due to inaccurate placement of the microphone. We have observed experimentally that moving the microphone off axis by as little as 0.25 mm can grossly affect the measurements. Our argument is given further support by the fact that the best agreement between measurements and theory is found for the case n=1. The first reflected wave is reflected from the tube wall only once and focused only once (at the microphone). It is much easier to accurately align a simple source-mirror-receiver system than to align a system in which the wave undergoes several reflections. The special short tube alignment procedure described in Chapter II was designed to minimize misalignment error, but apparently its use met only limited success.

It has been found that experimental error may also be introduced by imperfections in the interior surface of the tube. The misfit at the tube/microphone junction was varied, and a positive correlation was noticed between increasing misfit and waveform degradation. When care was

---

†In Chapter II it was determined from experimental data that finite amplitude effects are negligible for a spark energy of 0.04 J. This conclusion was based on the fact that wave shapes were the same for spark energies of 0.04 J and lower. The dependence of pulse amplitude on spark energy has not been investigated.

taken to ensure the smoothest surface possible, the misfit was less than 0.1 mm; still, its effect may be manifested as aberrations of the focused waves.

C. Amplitude Envelope

We can gain some insight into the long-time pressure behavior by considering the amplitude envelope of the pulse train measured in the long tube. By "amplitude envelope" we mean a curve connecting the points on a plot of peak-to-peak (p-p) pressure amplitudes. Because alternate pulses differ in phase by 180°, their shapes are similar but inverted. Either of the envelopes constructed from the odd or even numbered pulses gives an excellent indication of the long time pulse amplitude behavior, without introducing undesired phase information. The two envelopes are displaced from, but are essentially parallel to, each other.

Measured and computed p-p amplitudes are plotted versus odd values of n in Fig. 4.3. The measured values were taken from a pulse train similar to the one pictured in Fig. 1.2(a). The solid curve was computed by repeated application of NTUBE with x = 0.762 m (long tube). The spark energy for this run was 0.16 J, and the atmospheric conditions were the same as those noted in Section B. The direct N wave had a half-duration of 5 μsec and a peak pressure equal to 1.3 mbar.

The overall amplitude of the computed envelope is considerably larger than the amplitude of the measured envelope; however, the percent difference between the computed and measured data sets is not constant with respect to n. Variation between the two data sets may be shown more clearly if the computed curve is multiplied by a constant K<1. The value of K that yields the best fit of the computed curve to the measured data

AD-A099 990 TEXAS UNIV AT AUSTIN APPLIED RESEARCH LABS F/G 20/1
AXISYMMETRIC PROPAGATION OF A SPHERICAL N WAVE IN A CYLINDRICAL--ETC(U)
MAY 81 R D ESSERT N00014-75-C-0867
UNCLASSIFIED ARL-TR-81-22 NL

END
DATE
FILMED
6 81
DTIC

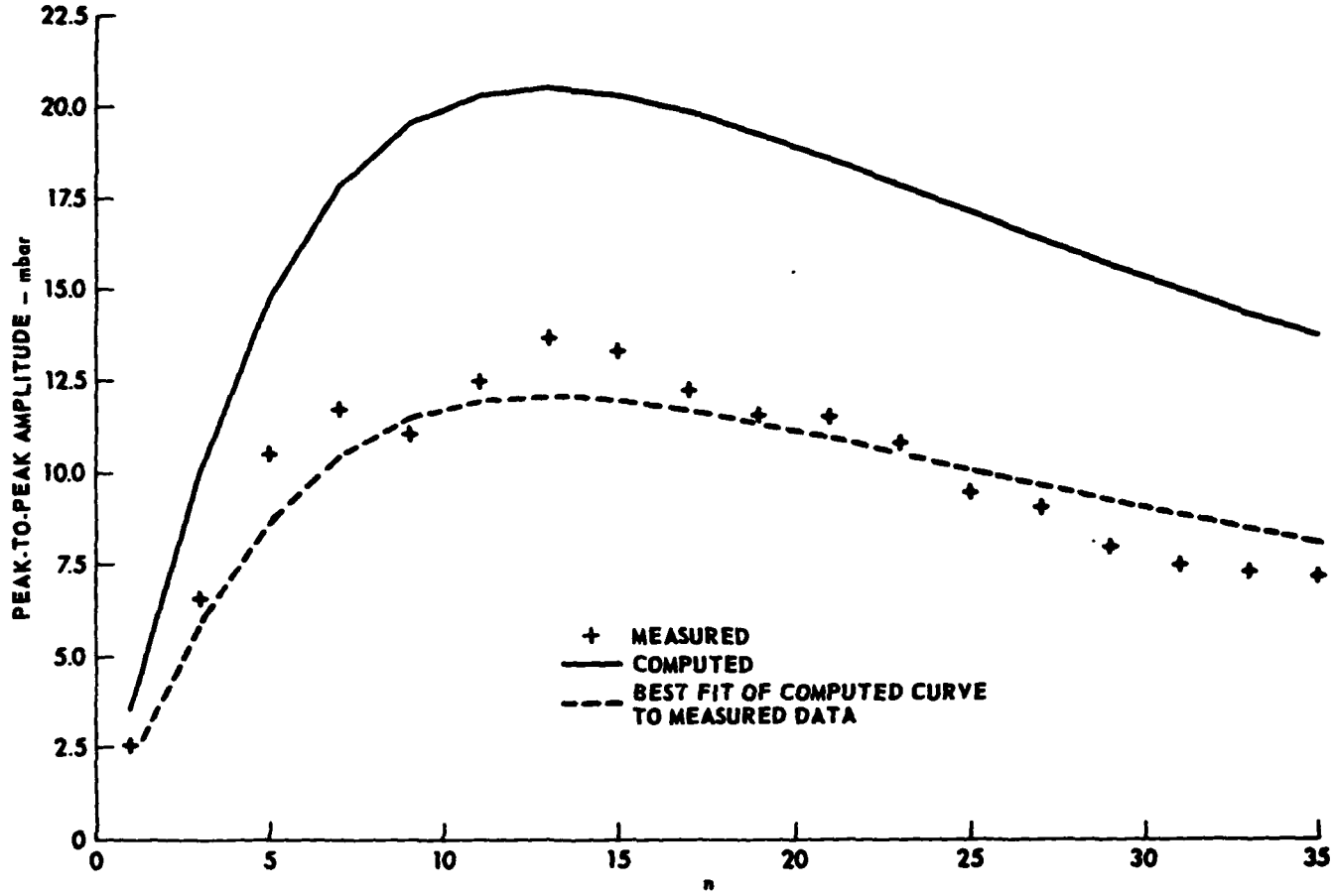

FIGURE 4.3
AMPLITUDE ENVELOPE – ODD NUMBERED REFLECTIONS
LONG TUBE

points (n=1 to 35, odd) is 0.587. The best-fit curve is given by the product of K and the computed curve, and is denoted in the figure by the dashed line. Comparison of the best-fit curve and the measured data reveals that the measured amplitude falls off with n more rapidly than does the computed amplitude.

In the previous section it was asserted that disagreement between measured and computed amplitudes is due, at least in part, to misalignment of the experimental apparatus. We are now in a position to estimate the microphone offset distance r from measurements of the amplitude envelope. Our estimate is based on the frequency domain pressure solution, Eq. (3.34), evaluated at the peak frequency ω_p of the direct wave spectrum. Now the largest peak in the spectrum $|\mathfrak{F}[N(t)]|$ of an ideal N wave is located at the frequency $\omega_p \simeq 2.1/T_o$ (see Appendix B, Section 1). To a rough approximation, the same is true for a real N wave. Let us assume that the amplitude of each reflected pulse is proportional to the amplitude of its largest spectral component.† Substituting the measured values of the p-p pressure into the LHS of Eq. (3.47c) and letting $\omega=\omega_p$ and $R=x=R_o$ in the RHS, one may find the radial receiver displacement $r=r(n)$ that could cause the observed reduction in measured amplitude.

Because the microphone directivity factor $D(\theta_n)$ is valid only for a transducer centered on the axis, it must be assumed that the

†This assumption is not as rash as it may at first seem. The spectrum of an ideal N wave falls off at 6 dB/octave on either side of ω_p. The reflected wave spectra are similar in shape to the spectrum of the direct N wave. For $D(\theta_n,\omega)\simeq 1$, $\omega_p/7<\omega<7\omega_p$, and $\alpha(\omega_p)R_n<<1$, the amplitude of p_n is nearly independent of frequency. The pulse amplitude is then roughly proportional to the spectrum amplitude at ω_p.

receiver is omnidirectional, i.e., that $D(\theta_n)=1$. The general effect of the finite size of a microphone (located at <u>any</u> radial position) on a received waveform is one of attenuation. Since the measurements were performed with a microphone of finite size, the measured amplitudes are less than the actual ones; the estimated values of r(n) are therefore too large. Furthermore, $\sin\theta_n$ is nearly constant for large n (the rate at which $\sin\theta_n$ approaches 1 depends on the tube geometry), and it follows that $D(\theta_n)$ tends to a constant as $n\to\infty$. Hence, for n large enough that $\sin\theta_n\simeq 1$, we should expect to find that r(n) approaches a constant value r, which is somewhat greater than the actual displacement of the microphone.

Estimated values of r(n) (n odd) have been calculated from the measured p-p amplitudes and Eq. (3.47c) for an ideal N wave whose half-duration is 5 μsec and whose spectral peak therefore falls at $f_p = \omega_p/2\pi = 67$ kHz. Atmospheric absorption at 67 kHz is 0.306 Np/m. The results are presented in Fig. 4.4. For $n \geq 15$ ($\theta_n \geq 45°$), the constancy of r(n) is quite remarkable, in light of the numerous approximations made in the above analysis and the considerable possibility for experimental error. From the curve it is estimated that an upper bound of the system misalignment is given by $r \simeq 1.5$ mm.

D. <u>Off-Axis Measurements</u>

An investigation of off-axis signals yields results which both support our ray theory solution and provide physical insight into the problem of misalignment. On-axis and off-axis waveforms measured in the short tube are pictured in Fig. 4.5. The axial distance (x = 0.074 m) and spark energy (0.06 J) were the same in each case.

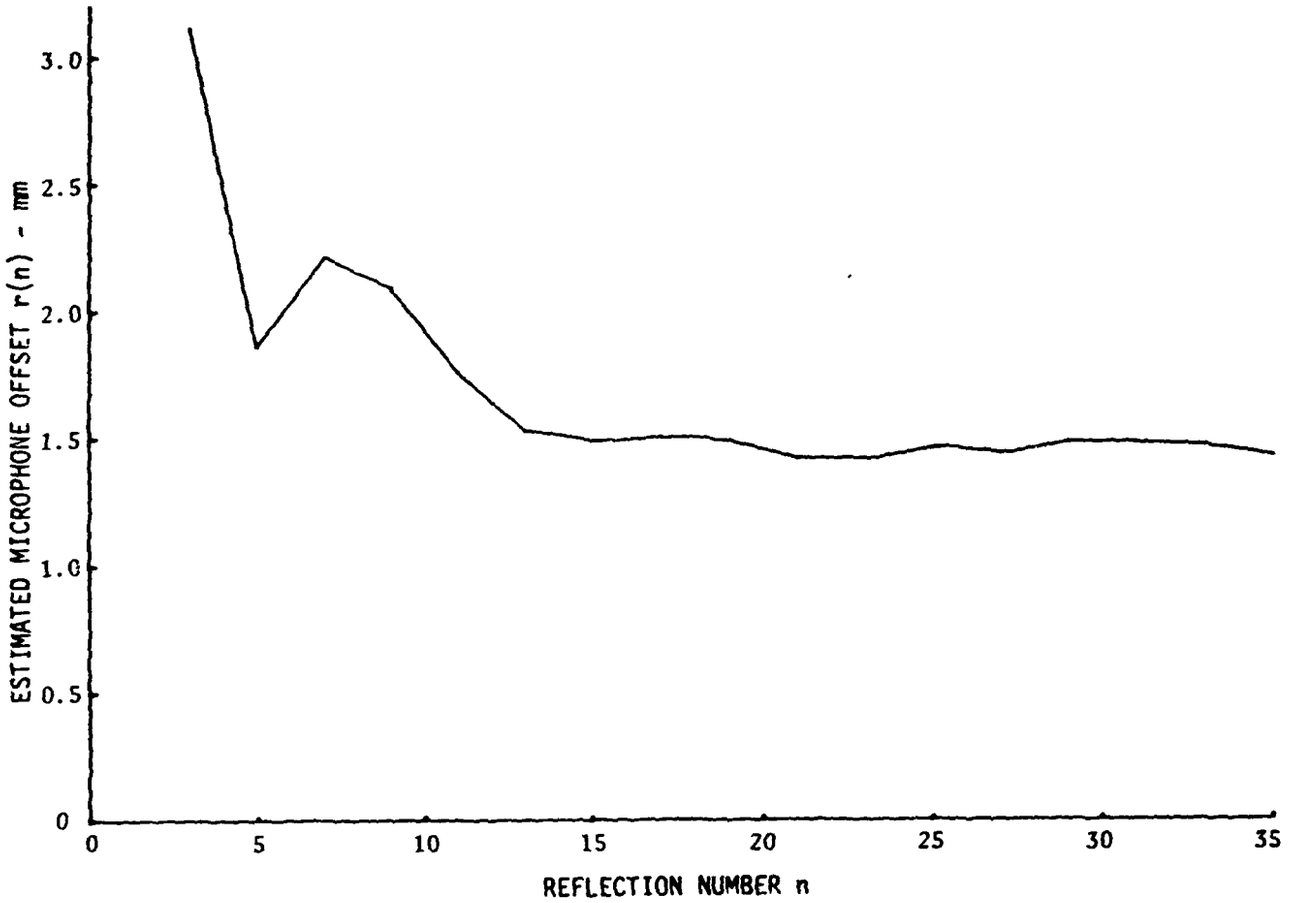

FIGURE 4.4

ESTIMATED MICROPHONE OFFSET - ODD NUMBERED REFLECTIONS
(LONG TUBE)

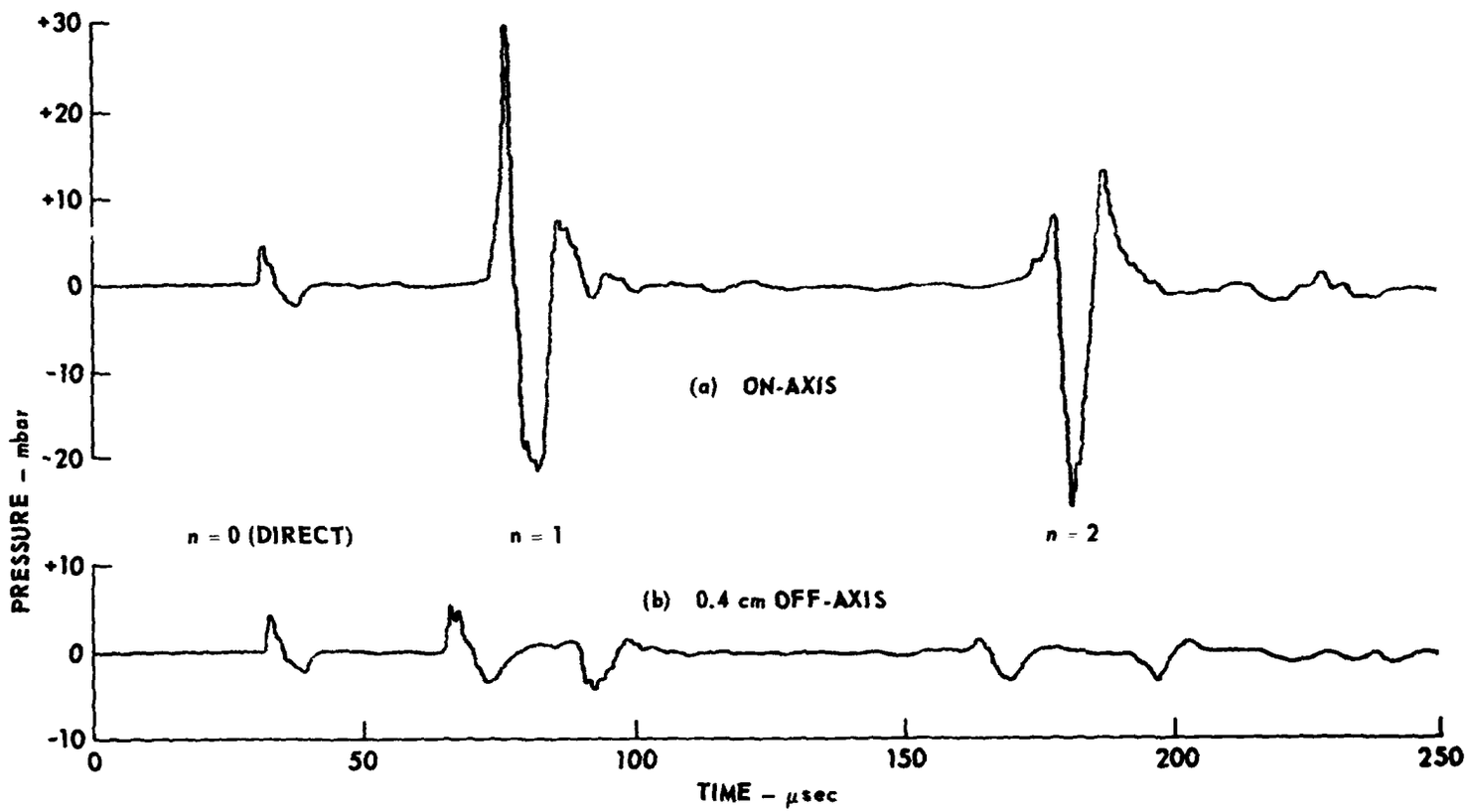

FIGURE 4.5
WAVEFORMS MEASURED ON AND OFF-AXIS

ARL:UT
AS-80-1288
RDE - GA
6 - 13 - 80

The figure shows how incoming and outgoing waves are combined at a focus. It also permits identification of the phase of each component wave. The off-axis waveform is described by Eq. (3.45): the incoming and outgoing signals for n=1 are shifted 0° and 90°, respectively, with respect to the direct wave. Those for n=2 are shifted by 90° and 180°, and so on, for each n. The shapes are in qualitative agreement with what one would expect from the shapes shown in Fig. 3.2.

E. Summary

In this chapter waveforms computed from the theoretical results have been compared with measured waveforms. The measured wave shapes have been accurately predicted, but the amplitudes have been overestimated by approximately 40%. Three possible explanations for the error have been suggested: neglect of boundary layer effects; misalignment of the experimental apparatus, which results in the measurement of incompletely focused waves; and nonlinear propagation distortion, which causes the sound wave to suffer excess attenuation. Boundary layer absorption has been discussed in some detail, and a quantitative estimate of the degree of misalignment has been given. Nonlinear distortion is discussed in the following chapter.

CHAPTER V

PROPAGATION OF FINITE AMPLITUDE WAVES IN THE TUBE

In the preceding chapters an investigation of the propagation of small-signal waves in a cylindrical tube was described. The spark energy was kept below 0.2 J. In this chapter results are presented which suggest that finite amplitude effects may be important for higher spark energies. The shapes of the individual waveforms in the pulse train change dramatically as the spark energy is increased from 0.04 J to 2.3 J.

The experimental results are investigated by means of a numerical ray tracing algorithm. The algorithm is synthesized from basic tenets of nonlinear acoustics and from results described in the previous chapters for propagation of small-signal waves in the tube. Because of time constraints the algorithm has not yet been implemented as a computer program. It is regrettable that no quantitative results can be given. However, qualitative results indicate that a solution of this type may adequately account for the observed change in pulse shape.

A. Measurements

Waveforms were recorded on the axis of the long tube for seven spark energies between 0.04 J and 2.28 J. The spark energy was increased by adjusting the length of the electrode gap; the longest gap, which corresponded to the highest energy, was approximately 2 mm. The experimental apparatus was unchanged from that used to make the low amplitude measurements. It was not possible to measure finite amplitude waves in the short tube because the microphone was overloaded by the extremely high pressures encountered close to the source.

Measured waveforms are presented in Fig. 5.1. Two preliminary observations are in order. First, the direct N wave, identified by the letter "D" in oscillograms (a)-(d), is in all cases at least partially obscured by the first reflected wave. As the spark energy is increased, the time lag between the direct and first reflected arrivals is diminished. The direct wave is not at all visible in oscillograms (e)-(g), which correspond to the highest spark energies. The amplitude of the first reflected wave is evidently large enough over at least part of its travel path to form a shock front capable of overtaking the direct wave. In a similar manner the second reflected pulse, which is larger in amplitude than the direct wave and the first reflected wave, overtakes them both when the source energy is large enough [e.g., 2.28 J, (g)]. Second, pulse duration increases with increasing source amplitude. This is to be expected because the length of the N wave, which forms the basis for each train of pulses, increases with spark energy (see Wright, Ref. 20).

The main conclusion to be drawn from Fig. 5.1 is that the apparent phase shift is amplitude dependent. As the source amplitude is increased, the shape of each pulse changes; yet for large n there appears to be a constant 90° phase shift between pulses. The shape is stable for spark energies less than about 0.04 J (as noted in Chapter II), but at higher energies the phase advances so that the nth high amplitude pulse has the same basic shape as the (n-1)th low amplitude pulse. Consider, for instance, pulse No. 8. As the spark energy is increased, the waveform gradually departs from its initial shape (a8). In (d) the shape more nearly resembles (a7). Moreover, the departure from shape (a8) continues to increase with spark energy so that in (g) pulse No. 8 resembles (a6),

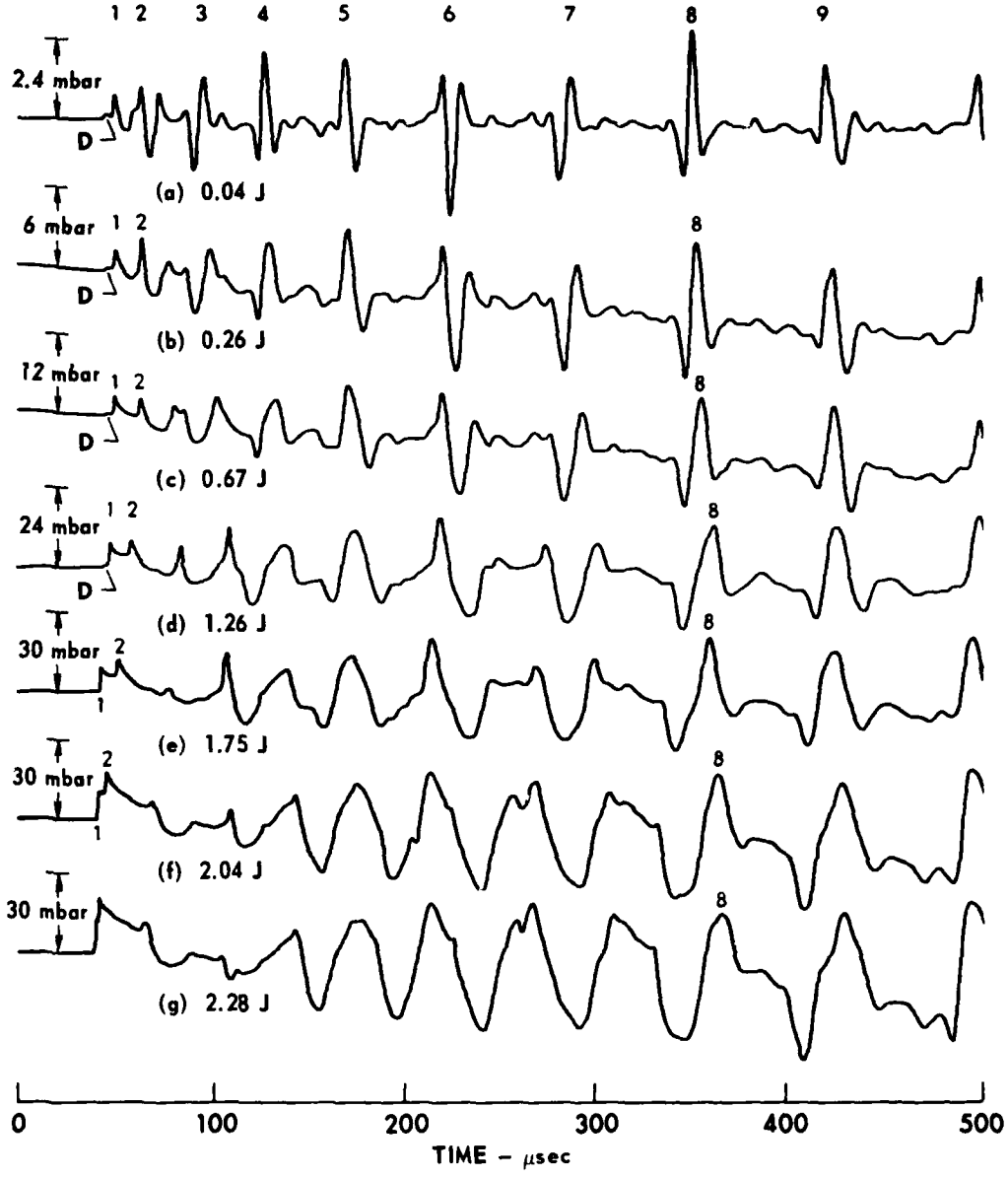

FIGURE 5.1
EFFECT OF FINITE AMPLITUDE ON MEASURED WAVEFORMS

ARL:UT
AS-80-1318
RDE - GA
6 - 30 - 80

a U-shaped wave. Similar progressions can easily be seen for all pulses arriving more than 100 μsec after the direct wave (unfortunately, at earlier times, overlapping of the pulses obscures the evidence). It is postulated that the reduction of phase shift is induced by nonlinear propagation distortion. In the following sections a numerical model is developed with which to test this hypothesis.

B. A General Propagation Algorithm

As a wave front propagates down the tube, it alternately converges and diverges in the radial direction. The wave amplitude therefore alternately increases and decreases along a ray. Because nonlinear propagation distortion increases with amplitude, the rate of distortion increases with distance for a converging wave and likewise decreases for a diverging wave. Approximate analytical solutions of the nonlinear wave equation are known for spherical and cylindrical waves, but none are applicable to the present problem. Numerical solutions have proven useful under circumstances similar to ours. In this section we discuss a general form of an algorithm developed by Anderson[30] to model free propagation of finite amplitude spherical waves in a lossy medium. It is shown that one may apply Anderson's algorithm to finite amplitude waves with arbitrary space and time dependence, given the geometric spreading factor for infinitesimal waves and the time dependence at some reference position.

Let us first define what is meant by "nonlinear propagation distortion," a term that has been used rather loosely up to this point. Simply put, nonlinear propagation distortion of a wave is manifested as a change in wave shape that arises because different points on a wave (called wavelets) travel with different velocities. A wavelet associated

with a particle velocity $u>0$ has a propagation speed greater than c_o (the small-signal propagation speed), while a wavelet with particle velocity $u<0$ travels at a speed less than c_o. In a lossless gas, the total velocity of a wavelet is

$$\left.\frac{dR}{dt}\right|_{u\,=\,\mathrm{const}} = c_o + \beta u \quad , \tag{5.1}$$

where $\beta=(\gamma+1)/2$. When the amplitude of the wave is infinitesimal, i.e., $u_{peak}\to 0$, all wavelets travel with approximately the same speed, and the wave does not distort significantly. However, when the wave is of finite amplitude ($u_{peak}>0$), the difference in speed between wavelets causes the wave to distort as it travels. The distortion is cumulative with distance.

Now consider the propagation of a finite amplitude wave from position R_o to position R_q. Each wavelet may be identified by the time Φ at which it leaves R_o; at this time the associated particle velocity is $u_o(\Phi)$. The wavelet arrives at position R_q at time[45]

$$t = \Phi + \int_{R_o}^{R_q} \frac{dt}{dR}\, dR \quad . \tag{5.2}$$

Combining Eqs. (5.1) and (5.2), one obtains

$$t = \Phi + \int_{R_o}^{R_q} \frac{dR}{c_o + \beta u} \quad . \tag{5.3}$$

Let us consider only waves for which $u<<c_o$. The denominator of Eq. (5.3) may then be expanded in a power series to yield an approximate expression for the integrand. If terms of second order and higher in u are neglected, the expression for t becomes

$$t = \Phi + \frac{1}{c_o} \int_{R_o}^{R_q} \left(1 - \frac{\beta u}{c_o}\right) dR \quad , \tag{5.4}$$

or

$$t' = \Phi - \frac{\beta}{c_o^2} \int_{R_o}^{R_q} u \, dR \quad , \tag{5.5}$$

where $t'=t-(R_q-R_o)/c_o$ is the retarded time. Explicit solutions of Eq. (5.5) may be readily obtained for plane ($u=u_o$), cylindrical ($u \propto u_o R^{-1/2}$), and spherical ($u \propto u_o R^{-1}$) waves.

The use of an iterative algorithm permits evaluation of Eq. (5.5) for a function u whose amplitude varies arbitrarily with distance, say, $u=u_o f(r)$. One can also include the effects of absorption in such an algorithm. *Absorption and geometric spreading* are computed in the frequency domain over a small step ΔR, and distortion is computed in the time domain over the same step. First, the particle velocity of wavelet Φ is specified at initial position R_o by $u_o(\Phi)$. Then the FFT is used to obtain $U_o(\omega)$, the Fourier transform of $u_o(\Phi)$. Absorption and geometric spreading are applied over ΔR in order to find the particle velocity $U_1(\omega)$ at $R_1=R_o+\Delta R$,

$$U_1(\omega) = \frac{f(R_1)}{f(R_o)} U_o(\omega) \; e^{-\alpha(\omega)\Delta R} \quad .$$

Finally, the inverse FFT is computed, and the arrival time t_1' at point R_1 is computed by means of Eq. (5.5). The step size ΔR is chosen small enough that $u(\Phi)$ may be considered constant over the entire step; for the first step, that constant is $u_1(\Phi)$. Thus, we have

$$t_1' = \Phi - \beta u_1(\Phi)\Delta R/c_o^2 \quad .$$

For successive distances $R_m = R_o + m\Delta R$ the attenuation and time shift are computed from the following:

$$u_m(\Phi) = u_o(\Phi) f(R_m)/f(R_o)\ e^{-\alpha(\omega) m\Delta R} \quad , \tag{5.6a}$$

$$t_m' = t_{m-1}' - \beta u_m(\Phi)\Delta R/c_o^2 \quad . \tag{5.6b}$$

Since ΔR has been chosen small enough that u_m may be considered constant, and since $u_m \ll c_o$, it may be assumed that the linear plane wave impedance relation $p = \rho_o c_o u$ is valid. Hence, Eq. (5.6b) may be rewritten in the form†

$$t_m' = t_{m-1}' - \frac{\beta p_o(\Phi) f(R_m)\Delta R}{\rho_o c_o^3\ f(R_o)} \quad . \tag{5.7}$$

Equations (5.6) and (5.7) describe the distortion suffered by a finite amplitude wave as it propagates in a lossy medium. Absorption and geometric spreading are computed in the frequency domain over the interval (R_{m-1}, R_m), and distortion is computed in the time domain over the same step. Then m is increased by one, and the absorption-distortion pair is repeated. The iteration is repeated until m=q, i.e., until the wave reaches the receiver.

---

†Here $p_o(\Phi)$ is the acoustic pressure at R_o and is not to be confused with the ambient pressure.

Equations (5.6) and (5.7) are valid as long as the waveform remains single valued. Anderson asserts that atmospheric absorption is sufficiently strong to keep the wave from becoming multivalued, and that in practice we need only choose a step size small enough that distortion does not cause the wave to become multivalued.

C. An Algorithm for the Propagation of Axisymmetric Waves in a Tube

Up to this point a general method has been described by which to numerically model the propagation of finite amplitude waves in a lossy medium. The algorithm is now specialized to the problem at hand. The presence of the tube complicates matters in three respects. (1) A wave propagating along one of the eigenrays (but not the direct ray) alternately converges and diverges. In order to use the propagation algorithm we must divide the travel path into sections on which the wave amplitude varies monotonically. (2) As a wave passes through a focus, its shape changes abruptly. It is assumed that the phase shift may be applied independently from the distortion and absorption. (3) It must also be assumed that the incoming and outgoing signals propagate independently of each other, i.e., that there is no standing wave nonlinear interaction. This algorithm may therefore be better adapted for pulses, for which the overlap of incoming and outgoing waves is quite limited, than for cw waves.

Between its emission by the source and its reception by the microphone, a wave is reflected from the tube wall n times and focused on the axis n times (the final focus occurs at the microphone). For purposes of computation we subdivide the propagation path into segments bounded by the points of reflection. On each segment the wave converges, focuses, and diverges. For the ith segment the focus is chosen as the origin of

the coordinate system. The wave is computer propagated between the ith and (i+1)th reflection points, through the ith focus; then the coordinate origin is shifted to the (i+1)th focus and the process is repeated. The coordinate system is pictured in Fig. 5.2 for i=1 and n=2. The ith focus O_i, is located a distance x_i from the source, and the points at which the wave reflects from the tube wall are labeled A_i, where i = 1, 2, ..., n. The wave converges as it travels along the ray segment $\overline{A_iO_i}$, suffers a 90° phase shift at O_i, and then diverges along $\overline{A_iA_{i+1}}$. At any point on $\overline{A_iA_{i+1}}$ the wave appears to have originated at the ith ring image source S_i, whose radius is r_i and whose distance from the focus is $R_i=(x_i^2+r_i^2)^{1/2}$. Since $r_i=(i/n)r_n$ and $x_i=(i/n)x_n$, the triangles OS_iO_i and OS_nO_n are similar triangles, and $\theta_i=\theta_n$.

The geometric spreading function $f_n^i(R)$ for propagation along the ith segment of the nth eigenray may be derived in a readily usable form from Eq. (3.44), which in terms of our new coordinate system may be written

$$P_n(r,x,\omega) = P_oR_oF(\omega)\ j^{n-1}\ e^{-jkR_n}\left(\frac{\sin\theta_n}{r}\right)^{1/2} \times \left[\frac{e^{jkr\sin\theta_n}}{(R_n - r\sin\theta_n)^{1/2}} + j\,\frac{e^{-jkr\sin\theta_n}}{(R_n + r\sin\theta_n)^{1/2}}\right] . \tag{5.9}$$

Recall that this equation describes the propagation of a small-signal wave in a lossy medium from the nth ring image source S_n to the receiver, which is situated at x_n. By replacing n with i we obtain an expression which describes propagation between the ith ring source and the ith focus along the nth eigenray,

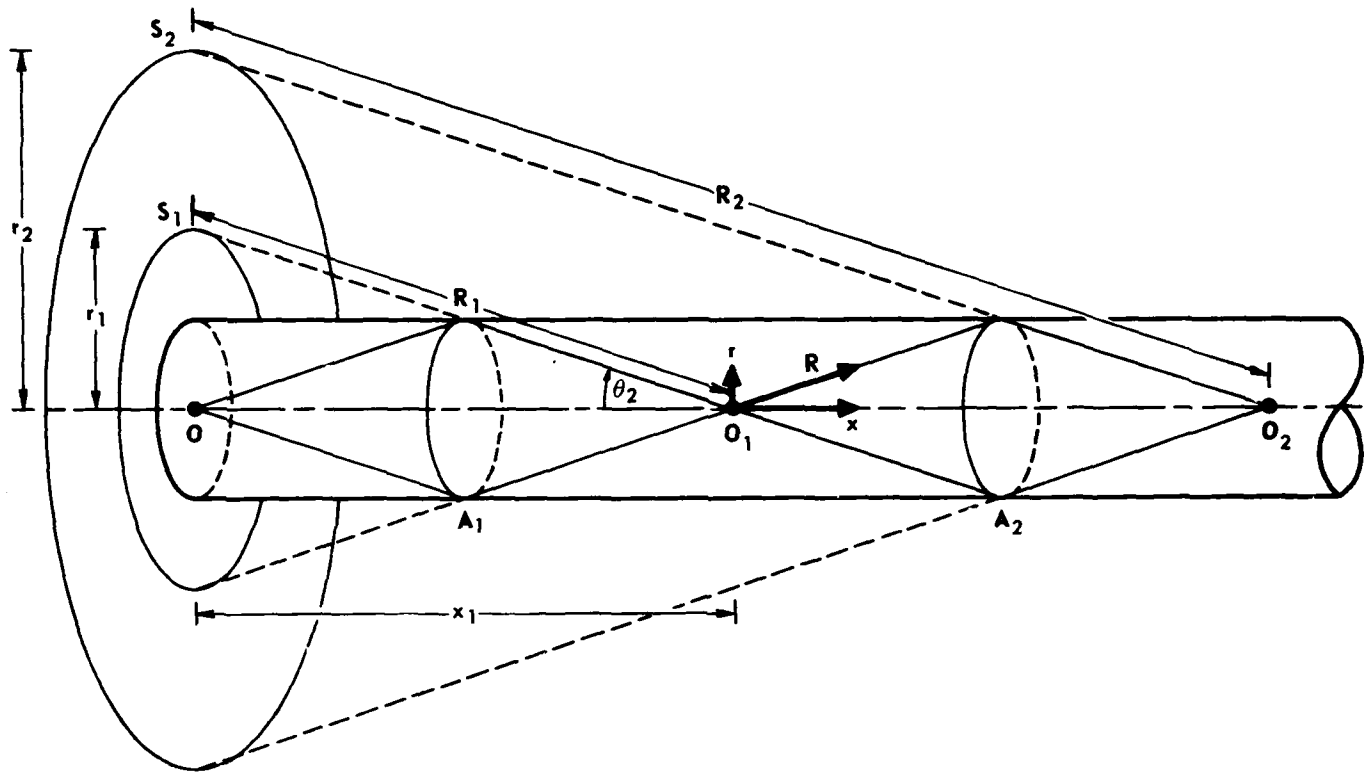

FIGURE 5.2
TRANSLATED COORDINATE SYSTEM
i = 1, n = 2

$$P_n^i(R',\omega) = P_o R_o F(\omega)\, j^{i-1}\, e^{-jkR_i} \frac{\sin\theta_n}{\sqrt{R'}} \left[\frac{e^{jkR'}}{(R_i-R')^{1/2}} + j\, \frac{e^{-jkR'}}{(R_i+R')^{1/2}} \right] \quad (5.10)$$

where $R' = r \sin\theta_n$. The geometric spreading factor for propagation along the nth eigenray is found by inspection from Eq. (5.10),

$$f_n^i(R') = \frac{\sin\theta_n}{\sqrt{R'(R_i-R')}} \qquad \text{(incoming waves)} \qquad (5.11a)$$

$$f_n^i(R') = \frac{\sin\theta_n}{\sqrt{R'(R_i+R')}} \qquad \text{(outgoing waves)} \quad . \qquad (5.11b)$$

By computing the inverse Fourier transform of Eq. (5.10), it can be shown that $p_n^i(R',t)$ is the sum of an incoming and outgoing wave. The former corresponds to a convergent front, which travels from A_i to O_i, and the latter corresponds to the divergent front that subsequently propagates from O_i to A_{i+1}. The factor j in the second term of Eq. (5.10) indicates that the phase of the outgoing wave lags that of the incoming wave by 90°. The cumulative phase factor $j^{i-1} \exp(-jkR_i)$ keeps a running total of the distance traveled by the wave and the number of times it has crossed the axis.

The special case i=0 corresponds to propagation along the first segment of the ray path, which lies between the real source O and the first reflection point A_1; on this segment the wave front spreads spherically. The segment length OA_1 is equal to $R_n/2n$. The input waveform for the propagation algorithm is measured on the axis at a distance $R_n/2n$ from the source. This reference waveform is "launched" from the point A_1 to propagate as a convergent wave along $\overline{A_1O_1}$.

The waveform is computed at positions R' on the nth eigenray according to the following two procedures. (1) For each R' absorption and geometric spreading are computed in the frequency domain, and distortion is computed in the time domain. The combination is referred to as a propagation step. (2) Each time the wave crosses the axis, its phase is shifted by 90°. A flow chart for the procedure is presented in Fig. 5.3.

A more elaborate description of the algorithm is now presented. The reader who is not interested in details may proceed to Section C without loss of continuity. To begin, the waveform is specified on a sphere of radius R_o. As we have already noted, it is convenient to specify the initial waveform at the tube wall (point A_1); then $R_o=R_n/2n$. In general the waveform at any reflection point A_i is given by the end result from propagation over the (i-1)th segment.

Consider then the general case in which a wave leaves A_i on $\overline{A_iO_i}$. The wave is propagated inward along the ray in small steps $\Delta R=\Delta r \sin\theta_n$. The position of the wave in relation to the ith focus is identified by the step index m, and the distance R'(m) from the ith focus is given by

$$R'(m) = R_o - m\Delta R \qquad \text{(incoming waves)} \quad , \qquad (5.12a)$$

$$R'(m) = m\Delta R \qquad \text{(outgoing waves)} \quad , \qquad (5.12b)$$

where m = 1, 2, ..., M, and $M\Delta R=R_n/2n$.

Incremental spreading, absorption, and distortion are computed at each position R'(m). Linear spreading and absorption are computed in the frequency domain from the formula

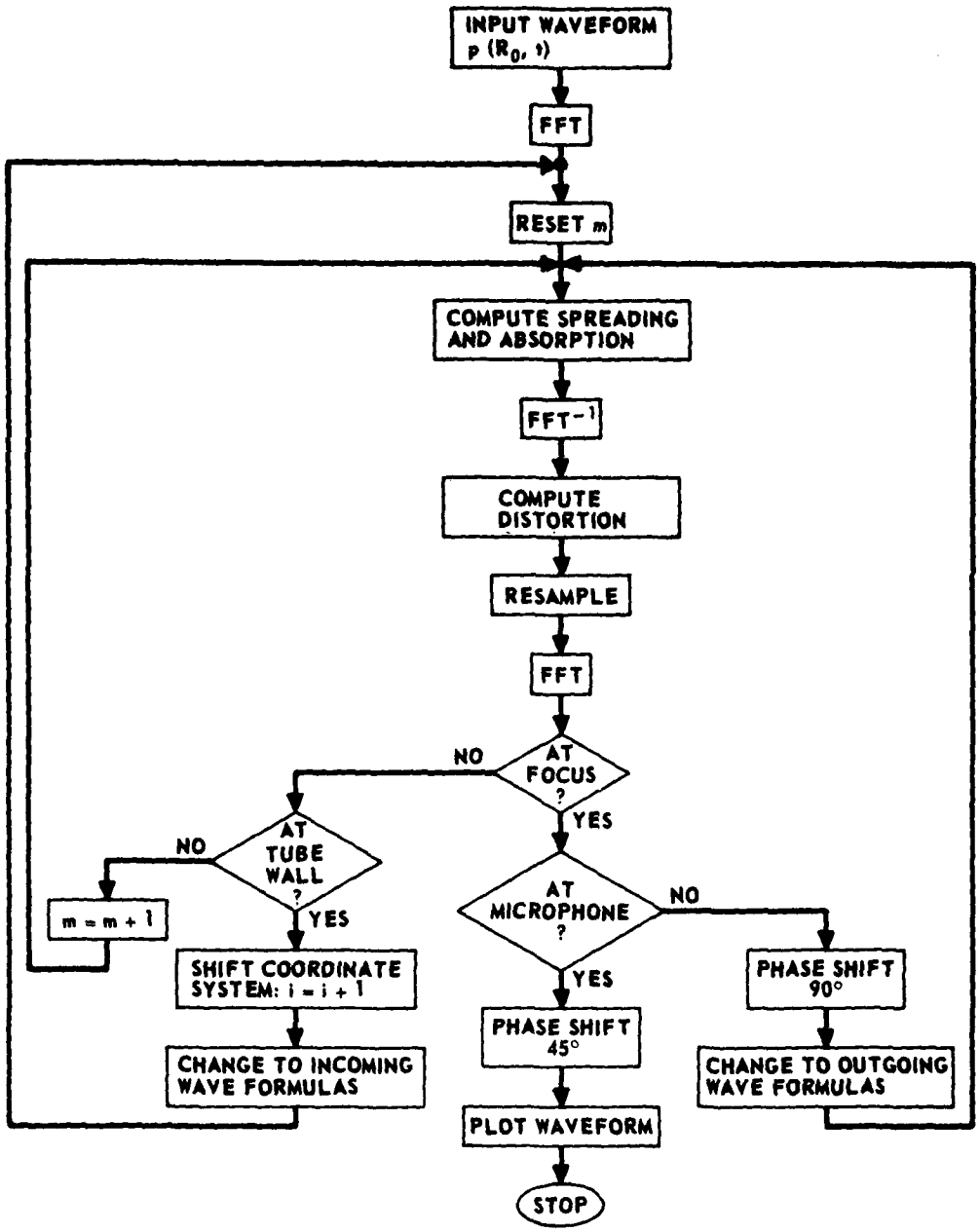

FIGURE 5.3
SIMPLIFIED FLOW CHART FOR PROPOSED PROPAGATION ALGORITHM

ARL:UT
AS-80-1320
RDE - GA
7 - 1 - 80

$$P[R'(m),\omega] = P[R'(m-1),\omega] \frac{f_n^i[R'(m)]}{f_n^i[R'(m-1)]} e^{-j\alpha(\omega)\Delta R} \quad , \tag{5.13}$$

where $R'(0)=R_o$. Function ABSORP is used to determine the absorption coefficient α at each component frequency. Distortion is computed in the time domain according to the equation

$$t'(m) = t'(m-1) - \frac{\beta\, p[R'(m-1),t'(m-1)]\Delta R,}{\rho_o c_o^3} \quad , \tag{5.14}$$

where $t'(0)=\Phi$.

The FFT routine used between the absorption and distortion steps requires that the time waveform be specified in equal time increments. However, the distorted waveform that results from the use of Eq. (5.14) does not satisfy this requirement. Subroutine RESAMPLE provides an equal time increment sample of the distorted waveform. A listing of RESAMPLE is given in Appendix B of the work by Anderson.[30]

Propagation is halted at a point R_n^- close to the focus. A 90° phase shift is then applied to $P(R_n^-,\omega)$. Propagation is resumed on the other side of the focus at $R=R_n^+=R_n^-$; the new reference is $P(R_n^+,\omega)$. It is assumed that the principal effect in going from R_n^- to R_n^+ is the phase shift due to focusing, i.e., nonlinear distortion is assumed small over this small distance. For the divergent front, the spreading factor f_n^i is specified by Eq. (5.11b) and the retarded time by

$$t' = t - (R_i-R_o+R_m)/c_o \quad .$$

Propagation is continued until the wave reaches the tube wall at point A_{i+1}. At this point the index i is increased by 1, the origin is moved

from O_i to O_{i+1}, and the propagation/phase shift/propagation sequence is repeated. As the wave front progresses down the tube, i increases sequentially from 1 to n. Propagation is complete when the signal arrives at the nth focus. Because the receiver is located at the nth focus, only a 45° phase shift is applied there. Finally, the waveform is plotted as a function of the retarded time $t'=t-(R_n-R_o)/c$.

The radius R_n^- at which the propagation sequence is temporarily halted has not yet been determined. We suggest that it be optimized so as to provide the best possible agreement between measured and computed results. Since the linear solution [Eq. (5.10)] upon which this algorithm is based is valid only for $kR'>>1$, it seems reasonable that, as a first try, R_n^- be chosen as small as possible but still large enough to satisfy $kR_n^->>1$.

C. Qualitative Results

The algorithm described above has not yet been implemented. However, using our knowledge of the three basic processes at work--absorption and spreading, distortion, and phase shift--we can sketch qualitative results. It is assumed that the phase shift happens very quickly; the wave shape therefore changes radically over a very short distance. Spreading-absorption and distortion, on the other hand, are cumulative processes: their effects increase with travel distance. Distortion tends to steepen the leading edges of positive pressure regions and the trailing edges of negative pressure regions. Absorption tends to smooth rapid changes in pressure and pressure gradient. Approximate waveforms sketched according to these three basic processes indicate that the proposed

algorithm may help to explain the extra phase shift noted for the waveforms observed at high spark energies.

Waveforms are sketched in Fig. 5.4 for various positions on a single eigenray. The points A_i correspond to points of reflection at the tube wall, the points O_i to successive foci (see Fig. 5.2). It is assumed in this example that n>3. The cumulative phase shift is noted directly to the right of each waveform. The apparent phase shift, found by comparing each of these waveforms with the results from linear theory (see Figs. 3.4, 3.5), is noted in parentheses. The sketches are quite rough, and the apparent phase shifts were determined only by visual comparison with the small-signal waveforms. Nevertheless, the results show that the time shift induced by nonlinear distortion can be interpreted as a phase shift.

The difference between the linear theory phase shift and the apparent phase shift increases as the wave propagates down the tube. Because the wave amplitude decreases with distance, finite amplitude effects become less important at large distances from the source. In the limit that the wave becomes a small-signal wave, the difference between the actual and apparent phase shifts becomes constant, and any further convergence or divergence is described by linear theory. The same type of behavior was observed in the measured waveforms.

In summary, finite amplitude sound waves have been measured on the axis of a cylindrical tube. The waveforms differ from small-signal waveforms obtained under otherwise equal conditions. We have postulated that nonlinear propagation distortion is responsible for the difference, and have proposed a numerical model to test our hypothesis. Qualitative results show that nonlinear propagation distortion alters the wave shape

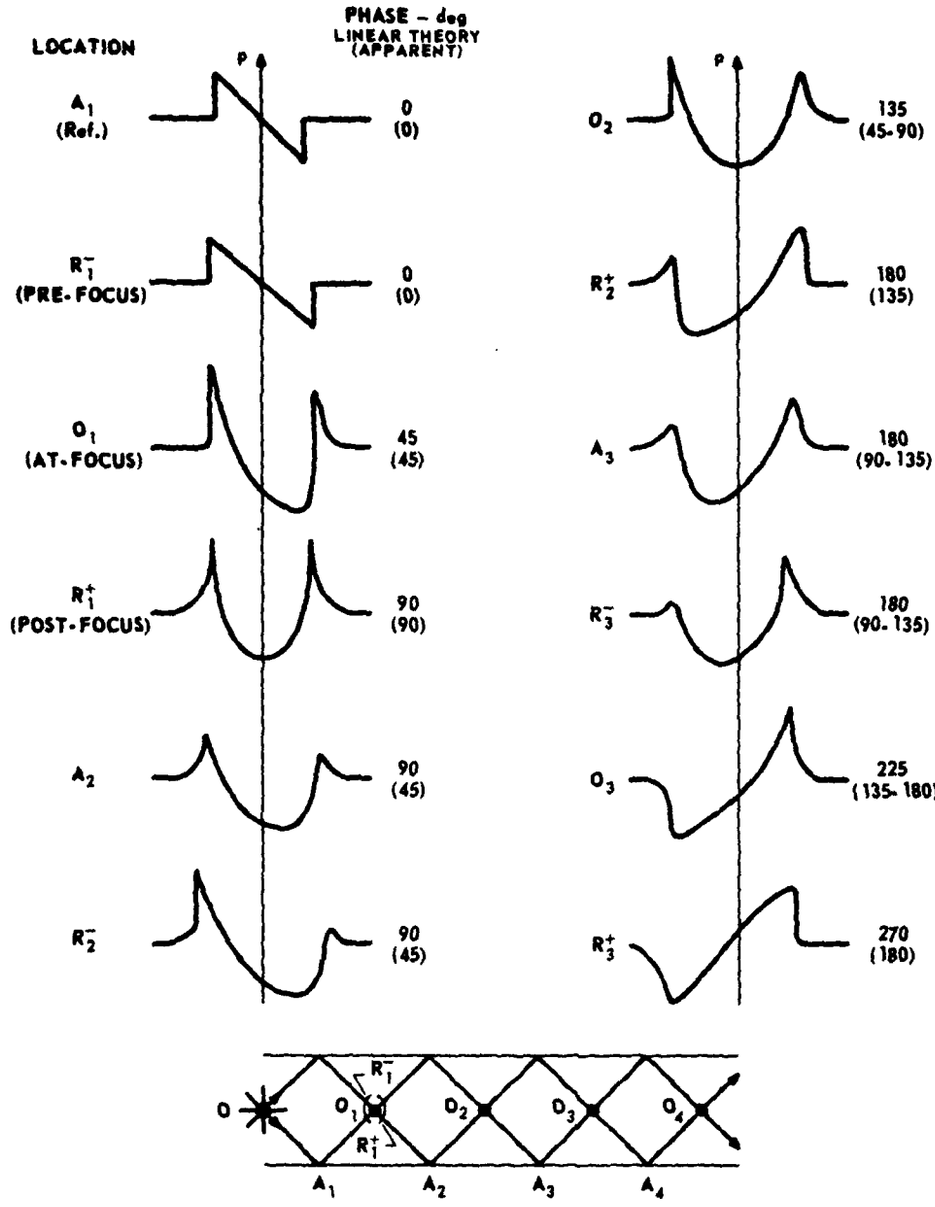

FIGURE 5.4
FINITE AMPLITUDE PRESSURE WAVEFORMS
SKETCHED ACCORDING TO PROPOSED PROPAGATION
ALGORITHM (NOT TO SCALE)

ARL:UT
AS-80-1321
RDE - GA
7 - 1 - 80

in accord with experimental observations. Actual implementation of this model will be necessary to more completely determine its validity.

CHAPTER VI

SUMMARY AND CONCLUSIONS

Experimental and theoretical means have been used to study the propagation of a spherically diverging pressure pulse in a rigid cylindrical tube. Both source and receiver were located on the tube axis, and the pulse was an N wave produced by an electric spark. Results have been obtained for both small-signal and finite amplitude waves.

In the experiment, N waves are produced by means of an electric spark, whose gap length was much shorter than the length of the N wave. Small-signal waveforms were measured on axis with a baffled condenser microphone and a digital oscilloscope. Measured waveforms indicate that the pressure observed at the receiver is a combination of direct and reflected waves. The shapes of the reflected waves vary periodically with reflection number n; the period is four pulses. It is surmised that the change in wave shape is caused by 90° phase shifts suffered as the waves focus on the axis. The envelope of the pulse amplitudes increases and then slowly decays. Most of the reflected waves are larger in amplitude than the direct wave. Measurements were also made with the microphone located off axis. The received signals were composed of pre- and post-focus waves, whose amplitudes were much smaller than those of the on-axis signals. Finally, the spark energy was increased, and finite amplitude waves were measured on the tube axis. The shape of each high amplitude pulse differed considerably from that of its corresponding low amplitude pulse.

Because of variation in spark amplitude and difficulty encountered in aligning the apparatus, individual pulse amplitudes were averaged over several spark discharges. An "average waveform", whose amplitude was the same as the computed mean, was then captured and stored. Use of this procedure permitted accurate measurement of each pulse in the series.

We have presented a theoretical analysis in which we account for thermoviscous and relaxation absorption and the finite size of the microphone, but assume that the source is an ideal point source, the tube wall is perfectly rigid, and boundary layer absorption is negligible. The linear, inhomogeneous wave equation for propagation in a thermoviscous medium has been solved by means of Fourier transforms. A general solution has been given in the full transform domain (r,ξ,ω). Approximate frequency domain (r,x,ω) solutions valid for "high frequency" $(ka \sin\theta_n >> 1)$ have been derived from the general solution for on- and off-axis observation points. The frequency domain solution shows that the signal received is the sum of direct and reflected waves, and that focusing, absorption, and microphone directivity contribute to the observed changes in wave shape and amplitude from one arrival to the next.

Time waveforms of the individual reflected pulses have been found by computing the inverse Fourier transform of the frequency domain solution. On- and off-axis waveforms have been calculated analytically for a case in which the direct wave is an ideal N wave, the medium lossless, and the receiver an ideal point probe. Waveforms have also been computed digitally for less restrictive conditions. The input waveform for the computer program was determined from measurements. Mainstream

thermoviscous and relaxation absorption were included, and the microphone was assumed to be a baffled piston of finite size. Computed and measured waveforms are similar in shape, but they differ substantially in amplitude. It has been postulated that the amplitude discrepancy is caused by one or more of three possible factors: misalignment of the apparatus, our neglect of boundary layer effects, or nonlinear propagation distortion.

The effect of finite amplitude on the measured waveforms has been investigated in some detail. Measured data suggested that the accumulated phase shift of each pulse is reduced by nonlinear propagation distortion. A numerical propagation algorithm, modeled after one developed by Anderson, has been devised to account for distortion, absorption, and focusing of the guided wave fronts. The algorithm has not yet been implemented. However, qualitative results sketched according to the basic principles involved suggest that use of the algorithm should yield improved theoretical predictions for finite amplitude waves. It is hoped that the algorithm will be implemented in the near future.

It is concluded from the experimental and theoretical results that when a point pressure source is placed on the axis of a cylindrical tube, the pressure elsewhere on the axis is equal to the sum of a direct wave, which propagates straight down the axis, and a series of reflected waves, which alternately bounce off the tube wall and focus on the axis. The time waveforms of the received signals are determined in large part by (1) the time history of the wave emitted by the source, (2) a cumulative phase shift, which is increased by 90° each time a wave front crosses the axis, (3) atmospheric absorption, (4) microphone directivity, and

(5) for larger source levels, nonlinear propagation distortion. Off axis the amplitudes of the received pulses are considerably reduced and the phase factors are different from their on-axis values.

The experimental and analytical techniques described herein, in addition to the results presented, may find application in problems similar to this one. A few related problems were mentioned in Chapter I. Further application of our results for the focusing of guided waves may be fruitful in areas such as array development and ultrasonic imaging. The digital implementation of atmospheric absorption may easily be adapted for use in architectural and environmental acoustics problems. Finally, this work should provide a foundation on which to begin study of the nonlinear interaction of multiple sound waves in a tube.

APPENDICES

APPENDIX A

90° PHASE SHIFT OF A BROADBAND SIGNAL

The phase properties of a broadband signal are most easily addressed in the frequency domain. It has been shown in a frequency domain analysis that two-dimensional focusing results in a 90° phase shift, or multiplication by $j(=\sqrt{-1})$. Let us assume that the pre-focus wave is a real function of time. In this appendix it is shown that the post-focus output is real if and only if the positive frequency components are shifted +90° and the negative components -90°, or vice versa.

First, let us establish some symmetry properties of Fourier transforms. The Fourier transform of f(t) is defined by

$$F(\omega) = \int_{-\infty}^{\infty} f(t)\, e^{-j\omega t}\, dt \quad .$$

If f and t are real, the complex conjugate of the transform is

$$F^*(\omega) = \int_{-\infty}^{\infty} f(t)\, e^{j\omega t}\, dt = F(-\omega) \quad . \tag{A.1}$$

Hence, if f(t) is real, F(ω) is <u>Hermitian</u> and therefore satisfies the following:

$$\begin{aligned} |F(-\omega)| &= |F^*(\omega)| \\ &= |F(\omega)| \\ \arg F(-\omega) &= \arg F^*(\omega) \\ &= -\arg F(\omega) \quad . \end{aligned}$$

That is, the amplitude of the transform is even and the phase is odd. It can be shown similarly that if $f(t)$ is pure imaginary, then $F(\omega)$ is <u>skew Hermitian</u>, i.e., $F(-\omega)=-F^*(\omega)$.[A.1]

Now let us postulate that $f_1(t)$ is real and that the transfer function of a "black box" which shifts all spectral components by 90° is $jG(\omega)$, where $G(\omega)$ is to be determined. If the transform of the input is $F_1(\omega)$, the transform of the output is given by

$$F_2(\omega) = jF_1(\omega)G(\omega) \quad . \tag{A.2}$$

In order for the output $f_2(t)$ to be real, $F_2(\omega)$ must have Hermitian symmetry. Substituting Eq. (A.2) into Eq. (A.1), one obtains

$$F_1(-\omega)G(-\omega) = -F_1^*(\omega)G^*(\omega) \quad .$$

Since $f_1(t)$ is real, $F_1(\omega)$ is Hermitian, and we find that G satisfies the relation

$$G(-\omega) = -G^*(\omega) \quad .$$

In other words, G is skew Hermitian.

The function G must be real to maintain the 90° phase difference between F_1 and F_2. It follows that $G(-\omega)=-G(\omega)$. In addition, our "black box" has no effect on the magnitude of F_1 (i.e., $|F_2|=|F_1|$); so $|G|=1$. It is concluded that

$$G(\omega) = \mathrm{sgn}(\omega) \equiv \begin{cases} 1 & , \quad \omega > 0 \\ 0 & , \quad \omega = 0 \\ -1 & , \quad \omega < 0 \end{cases} \quad .$$

Thus, if a broadband signal is to be shifted by 90°, its Fourier transform must be multiplied by $j\ \mathrm{sgn}(\omega)$.

APPENDIX B

ATMOSPHERIC ABSORPTION OF A SMALL-SIGNAL N WAVE

In this appendix analytical and digital methods are described for calculating the shape of a small-signal N wave as it propagates through homogeneous air. Results from the theoretical models are compared with measured N waveforms. The digital techniques employed herein are used in Chapter III to account for atmospheric absorption in the cylindrical tube.

The coefficient α for calculation of the absorption of sound in air has been standardized in American National Standards Institute (ANSI) document S1.26-1978.[B.1] The frequency dependence is given in simplified form by

$$\alpha = a\omega^2 + b\omega_O/\left[1+(\omega_O/\omega)^2\right] + d\omega_N/\left[1+(\omega_N/\omega)^2\right] \quad \text{Np/m} \quad , \qquad (B.1)$$

where ω ($=2\pi f$) is the angular frequency, ω_O and ω_N are the angular vibrational relaxation frequencies of oxygen and nitrogen, respectively, and a, b, and d depend on the ambient temperature T and pressure p_o. The values of ω_O and ω_N depend on T, p_o, and the relative humidity RH. Procedures for calculating ω_O, ω_N, a, b, and d are given in the ANSI standard. The absorption coefficient calculated by this method is accurate to within ±10%, subject to the following restrictions:

$$50 \le f/p_o \le 10^6 \text{ Hz/atm} \quad , \quad p_o < 2 \text{ atm} \quad ;$$

$$0 \le T \le 40°\text{C} \quad ;$$

$$10 \le \text{RH} \le 100\% \quad .$$

An analytical solution is found for the propagation of an ideal N wave through air. The solution is based on an expansion of α to first order in ω^2; the expansion is valid at frequencies such that $\omega \gg \omega_0$. The low frequency accuracy of the solution is improved by approximating with a two-term polynomial fit; the coefficients are determined from a quadratic fit of the ANSI absorption.

A computer model based on the ANSI absorption is developed to calculate the effects of atmospheric absorption on arbitrary broadband pressure signals.

Finally, the results of a free-medium propagation experiment are presented. Measured waveforms are in favorable agreement with those obtained from the analytical and digital models.

1. Quadratic Approximation for α

Each of the three terms in the expression for α represents the effect of a different absorption mechanism. The first term on the right-hand side of Eq. (B.1) is equal to the sum of the so-called classical thermoviscous absorption α_{cl} (which includes Stokes' assumption about the ratio of the two viscosity coefficients) and the rotational relaxation absorption α_r. The classical absorption is defined by[B.2]

$$\alpha_{cl} = \frac{\nu\omega^2}{2c_o^3}\left[\frac{4}{3} + \frac{\gamma - 1}{Pr}\right] \quad \text{Np/m} \quad ,$$

where ν is the kinematic viscosity, γ is the ratio of specific heats, c_o is the sound speed, and Pr is the Prandtl number. The rotational relaxation absorption at room temperature has been measured by Greenspan.[B.3] Bass and Keeton[B.4] give a simplified result for f << 100 MHz,

$$\alpha_r = 0.32\ \alpha_{cl} \quad .$$

The second and third terms in Eq. (B.1) owe their presence to the vibrational relaxation of oxygen and nitrogen, respectively. When T, p_o, and RH are within the limits set by the standard, ω_O is between one and two orders of magnitude greater than ω_N. If the frequency range of interest is limited to $\omega >> \omega_O$, the third term may be neglected, and the second may be expanded in powers of $(\omega_O/\omega)^2$ to yield

$$b\omega_O\left[1+\left(\omega_O/\omega\right)^2\right]^{-1} = b\omega_O\left[1-\left(\omega_O/\omega\right)^2 + \ldots\right] \approx b\omega_O \quad .$$

The total atmospheric absorption may therefore be approximated by the quadratic

$$\bar{\alpha} = a\omega^2 + b\omega_O \qquad (\omega >> \omega_O) \quad .$$

The parameters a and b and the relaxation frequencies ω_O and ω_N have been computed for the actual atmospheric conditions according to ANSI S1.26. Under typical laboratory conditions the oxygen relaxation frequency $f_O = \omega_O/2\pi$ lies between 10 kHz and 75 kHz. More specifically, when T=25°C, p_o = 1 atm, and RH=48%, we find that

$$f_O = 54.3 \text{ kHz} \quad ,$$
$$a = 4.71 \times 10^{-13} \text{ Np} - \text{sec}^2/\text{m} \quad ,$$
$$b\omega_O = 3.64 \times 10^{-1} \text{ Np/m} \quad .$$

The approximate absorption $\bar{\alpha}$ and the ANSI absorption α are plotted in Fig. B.1. The $\bar{\alpha}$ curve is an unacceptably poor approximation at frequencies below about 50 kHz: the error is 82% at 50 kHz and 2500% at 10 kHz. Clearly, strict adherence to the condition $\omega >> \omega_O$ is a severe restriction

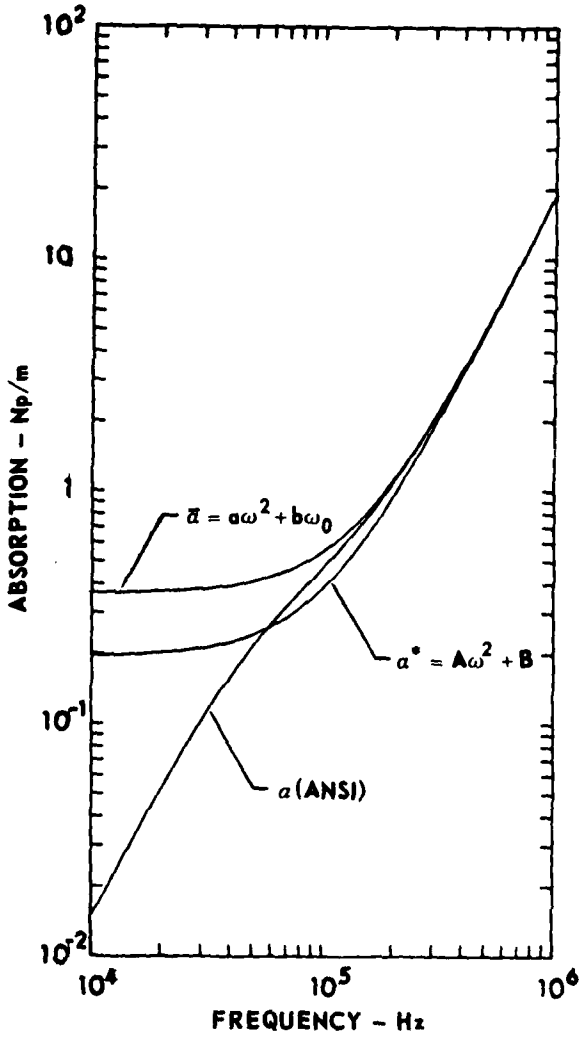

FIGURE B.1
ABSORPTION CURVES FOR AIR: ANSI STANDARD AND POLYNOMIAL FIT
RH = 48%, T = 25°C, p_0 = 1.0 atm

on the usefulness of the $\bar{\alpha}$ curve. The frequency content of a small-signal N wave is now examined to determine whether it conforms to this restriction.

The Fourier spectrum (magnitude of the Fourier transform) of an ideal N wave is obtained from Eq. (3.56),

$$|\mathcal{F}[N(t)]| = |(2/\omega)j_1(\omega T_o)| \text{ (units of time)} \quad ,$$

where $j_1(z)$ is the spherical Bessel function of the first kind of order 1 and T_o is the N wave half-duration. The first (and largest) peak in the

spectrum is located at the point $\omega_p = 2\pi f_p \approx 2.1/T_o$. Although the spectrum has nonzero amplitude down to zero frequency, a reasonable low end cutoff may be imposed at a frequency where the spectrum level is 10 dB below the peak level. In the case of an ideal N wave, the cutoff frequency f_{-10dB} is approximately equal to $f_p/7$. Now the amplitude and duration of spark-produced N waves cannot be varied independently.[B.5] In order to qualify as a "small signal" at typical short laboratory distances (peak pressure level < 125 dB re 2×10^{-5} N/m^2), an N wave must have a half-duration less than about 5 μsec. Then, if $T_o \leq 5$ μsec, the low end cutoff frequency f_{-10dB} is approximately equal to 10 kHz.

One may similarly show that the upper cutoff frequency f^{-10dB} of the envelope of an ideal N wave spectrum falls approximately at $7f_p$. The high frequency range of the approximate absorption is limited by the restriction of the ANSI absorption to frequencies less than 1 MHz. Furthermore, the bandwidth of the experimental apparatus is 1 MHz. If the N wave spectrum is limited to $f \leq f^{-10dB} = 1$ MHz, the usable range of N wave duration is restricted to $T_o \geq 2.5$ μsec. To summarize, the infinite bandwidth of a low amplitude, ideal N wave may be reduced to an important band of frequencies between 10 kHz and 1 MHz; yet the approximate absorption is considerably in error at frequencies below 50 kHz.

In an effort to achieve better overall agreement between the standard and approximate absorption curves, a linear, least squares regression was performed on the ANSI absorption to determine a best-fit approximation of the form $\alpha^* = A\omega^2 + B$. The regression was performed over the interval 10 kHz to 1 MHz with a sampling density of 25 points per

decade. The following atmospheric conditions were specified: T=25°C, p_o = 1 atm, and RH=48%. For these conditions the "improved" coefficients A and B were determined to be

$$A = 4.79 \times 10^{-13} \text{ Np - sec}^2/\text{m} \quad ,$$

$$B = 1.94 \times 10^{-1} \text{ Np/m} \quad .$$

The correlation coefficient is 0.9996. The quadratic fit is within +0.18, -0.14 Np/m of the ANSI absorption at 48% relative humidity between 10 kHz and 1.0 MHz. Relative error is usually considered a more valuable statistic than absolute error. The relative error between α^* and α is large at low frequencies. Nevertheless, the attenuation is so small at low frequencies that the effects of the error on the propagation of a small-signal N wave over short distances are negligible.

The best-fit absorption α^* is presented in Fig. B.1 along with the ANSI absorption α and the first approximation $\bar{\alpha}$. The quadratic fit α^* represents a significant improvement over the first approximation $\bar{\alpha}$, especially with regard to N wave propagation. The error in $\bar{\alpha}$ is large at low frequencies (3.1 Np/m at 10 kHz) and vanishingly small at high frequencies (6×10^{-3} Np/m at 1 MHz), while the error in α^* is balanced more evenly throughout the frequency domain.

The fact that the ANSI and best-fit curves intersect is of additional merit. The second approximation α^* is more accurate than the first approximation $\bar{\alpha}$ in a band of frequencies centered at the intersection frequency, 58.4 kHz. For example, in the octave band centered at 58.4 kHz (41.3 - 82.5 kHz), the error in α^* is within -0.057, +0.061 Np/m. Now the maximum amplitude in the spectrum of an ideal N wave whose half-

duration is 5 μsec falls at 67 kHz. At this frequency the error in α^* is 0.024 Np/m, and the error in $\bar{\alpha}$ is 0.14 Np/m. It is therefore expected that the use of α^* instead of $\bar{\alpha}$ will yield more accurate results in the analytical solution, which is derived in the next section.

2. Propagation of a Small-Signal N Wave; Approximate Absorption

The approximate absorption coefficient is now applied to a diverging, spherical N wave. An integral solution is obtained which is valid for a large class of signals f(t) whose Fourier spectra are concentrated in, but not necessarily confined to, the frequency band 10 kHz to 1 MHz. The limits of integration are $-\infty$, ∞. It is assumed that the spectral components of f below 10 kHz and above 1 MHz contribute little to the shape of f(t); error in their attenuation will therefore make little difference to the shape of the propagated waveform.

Consider an outgoing spherical wave f(t) whose Fourier transform $F(\omega)$ has the aforementioned characteristics. For propagation through air, dispersion is negligible and the absorption may be approximated by α^*. The signal may be represented at position R by its Fourier transform

$$F(\omega,R-R_o) = (R_o/R)\ F(\omega,R_o)\ e^{-jk(R-R_o)} \quad ,$$

where $F(\omega,R_o)$ is the Fourier transform of the signal at the source position R_o and the propagation constant k is defined by

$$k = \omega/c_o - j\alpha^* \quad .$$

Since

$$\mathcal{F}^{-1}\left[e^{-jk(R-R_o)}\right] = \left[4\pi A(R-R_o)\right]^{-1/2} \exp\left[-B(R-R_o) - t'^2/4A(R-R_o)\right] \quad ,$$

where $t'=t-(R-R_o)/c_o$, the time function $f(t',R-R_o)$ corresponding to $F(\omega,R-R_o)$ is given by the following convolution integral:

$$f(t',R-R_o) = (R_o/R)\left[4\pi A(R-R_o)\right]^{-1/2} e^{-B(R-R_o)}$$

$$\times \int_{-\infty}^{\infty} f(t'-\tau,R_o)\, e^{-\tau^2/4A(R-R_o)}\, d\tau \quad . \qquad (B.2)$$

It is possible to evaluate this integral exactly for a variety of simple functions f, including periodic functions, Gaussian functions, and a few transients of finite duration. One such transient is the ideal N wave.

Consider the ideal N function, which, in terms of the dimensionless retarded time $\phi=t'/T_o$, is given by [see Eq. (3.57)]

$$N(\phi) = -\phi \text{ rect}[\phi/2] \quad . \qquad (B.3)$$

When the source function $f(\phi,R_o)$ is equal to $N(\phi)$, the convolution integral takes the form

$$\frac{R}{R_o} f(\phi,R-R_o) = \left[4\pi A(R-R_o)\right]^{-1/2} e^{-B(R-R_o)}\, T_o$$

$$\times \int_{-\infty}^{\infty} (\tau-\phi) \text{ rect}[(\phi-\tau)/2]\, e^{-\tau^2/\eta}\, d\tau \quad ,$$

where $\eta=4A(R-R_o)/T_o^2$. Changing the limits of integration in accordance with the properties of the rect function, we may rewrite the above integral as the sum of two integrals,

$$\frac{R}{R_o} f(\phi,R-R_o) = \left[4\pi A(R-R_o)\right]^{-1/2} e^{-B(R-R_o)}\, T_o$$

$$\times \left\{\int_{\phi-1}^{\phi+1} \tau\, e^{-\tau^2/\eta}\, d\tau - \phi \int_{\phi-1}^{\phi+1} e^{-\tau^2/\eta}\, d\tau\right\} \quad .$$

The result is

$$\frac{R}{R_o} f(\phi,R-R_o) = e^{-B(R-R_o)} \left((\eta/\pi)^{1/2} e^{-(\phi^2+1)/\eta} \sinh(2\phi/\eta) \right.$$

$$\left. - \frac{\phi}{2} \left\{ \mathrm{erf}[(\phi+1)/\sqrt{\eta}] - \mathrm{erf}[(\phi-1)/\sqrt{\eta}] \right\} \right) \quad , \qquad (B.4)$$

where erf[x] is the error integral, defined by

$$\mathrm{erf}[x] = \frac{2}{\sqrt{\pi}} \int_0^x e^{-t^2} dt \quad .$$

Let us examine the behavior of the second term in Eq. (B.4). When the effective absorption is very small, η approaches zero. This limit is appropriate for large values of T_o and for short distances. Since

$$\mathrm{erf}[x] \sim \begin{cases} 1 & , \quad x > 2 \\ -1 & , \quad x < 2 \end{cases} \quad ,$$

the second term on the right-hand side of Eq. (B.4) is approximately linear near the time origin. It has extrema at some values of $|\phi|<1$ and drops to half the extremum amplitude when $|\phi|=1$.

The behavior of the first term differs from that of the second term in such a way as to diminish their sum. The extrema of the first term are found at the points $\phi=\pm 1$:

$$\frac{R}{R_o} f(\pm 1,R-R_o) = \pm(\eta/4\pi)^{1/2} e^{-B(R-R_o)} (1-e^{-4/\eta}) \quad .$$

The peak amplitude tends to zero when η is small and is approximately equal to $1/2\sqrt{\pi}$ for $\eta=1$. When the effective absorption is large, $\eta\to\infty$ and both the first and second terms vanish.

The two contributing terms and their sum are shown for various values of the parameter η in Fig. B.2. The factor $\exp[-B(R-R_o)]$ has been suppressed because it is the same in all cases. The second term exhibits the basic character of a decaying N wave: its amplitude decays with increasing R. The extra attenuation represented by the first term is appreciable only for moderately large values of η ($10^{-1}<\eta<10^{3}$).

A similar approximation of the atmospheric absorption curve has been used by Rogers and Gardner,[B.6] who took advantage of the fact that

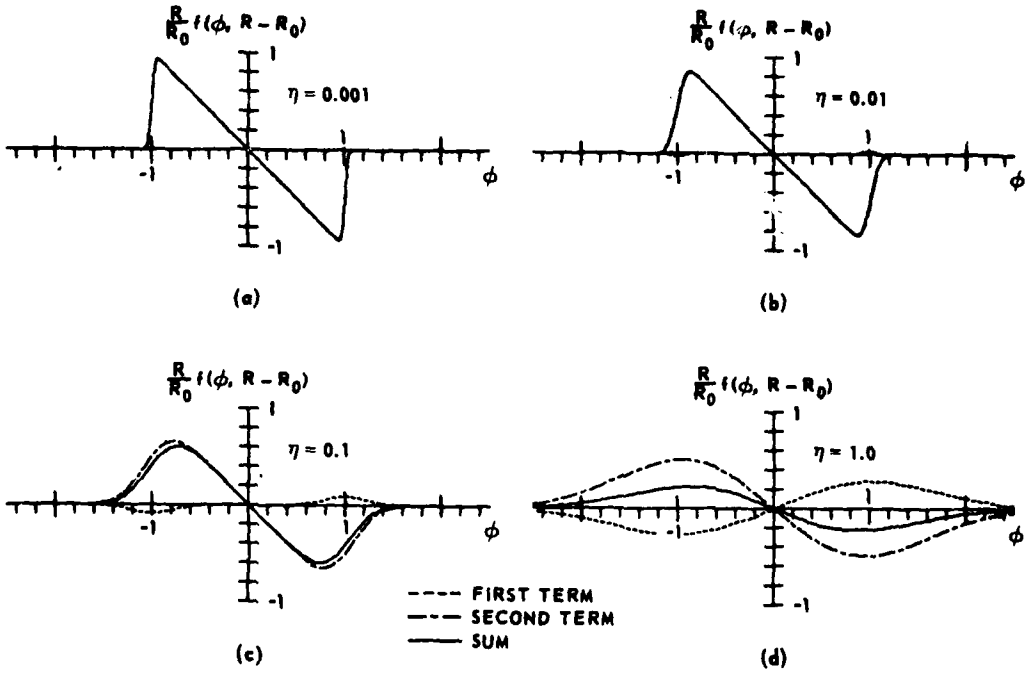

FIGURE B.2
ANALYTICAL SOLUTION FOR VARIOUS VALUES OF THE ABSORPTION PARAMETER η
THE FACTOR $\exp[-B(R-R_0)]$ HAS BEEN SUPPRESSED
$\phi = t'/T_0$

ARL:UT
AS-80-776
RDE - GA
2 - 22 - 80

the curve was a simple ω^2 dependence for frequencies far below the nitrogen relaxation frequency.

3. Digital Implementation; ANSI Standard Absorption

Direct comparison of the analytical solution for an ideal N wave with measured waveforms is not very revealing because the real wave does not start out (at the reference distance R_o) as an ideal N. This fact motivated the development of a computer algorithm that is able to handle both ideal and real waveforms. Use of the computer model made possible an indirect comparison of the analytical solution and the measurements, and afforded a useful check for both.

The computer model is summarized in Fig. B.3. First the fast Fourier transform (FFT) is used to obtain a frequency domain

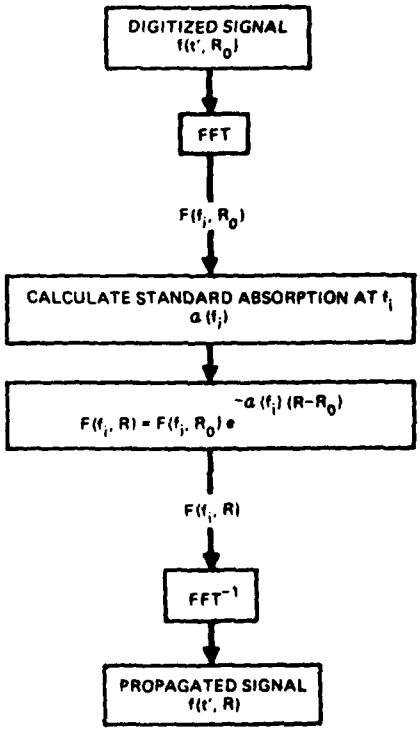

FIGURE B.3
COMPUTER ALGORITHM FOR EVALUATING ABSORPTION EFFECTS ON A SIGNAL OF ARBITRARY TIME WAVEFORM

representation of the (digitized) reference waveform. Next the ANSI standard absorption is applied to each frequency component. Finally, the inverse FFT is used to obtain the time waveform of the attenuated signal. Two ways of providing the input $f(t',R_o)$ were used: The ideal N wave was digitized by a computer subroutine; real N waves were digitized by the oscilloscope.

First we discuss the results for an ideal N wave input. Two different sets of computations were made: (1) T_o fixed (5 μsec) and $R-R_o$ varied so as to yield the values 0.001, 0.01, 0.1, 1 for η; (2) $R-R_o$ fixed (1 m) and T_o varied to yield the same four values for η. The first set corresponds to physical propagation through the atmosphere. The second serves to establish a range of validity for the analytical solution. The results are presented in Fig. B.4, along with waveforms calculated using the analytical model under the same conditions.

Consider first the two columns, Fig. B.4(a) and (b). The agreement for each value of η can easily be justified: The spectrum of an N wave whose half-period is 5 μsec is, for the most part, within the designed frequency window 10 kHz - 1 MHz. For T_o = 5 μsec the analytical solution is accurate for the life of the signal, at least until the signal has been attenuated by 40 dB.

The second set of computations leads to the waveforms shown in columns (c) and (d). Comparison of the two columns reveals that slight discrepancies exist between the analytical and digital computations. When T_o is much larger than 5 μsec, significant low frequency energy lies outside the design window. Since low frequency absorption in the analytical model does not change with frequency, below 10 kHz the

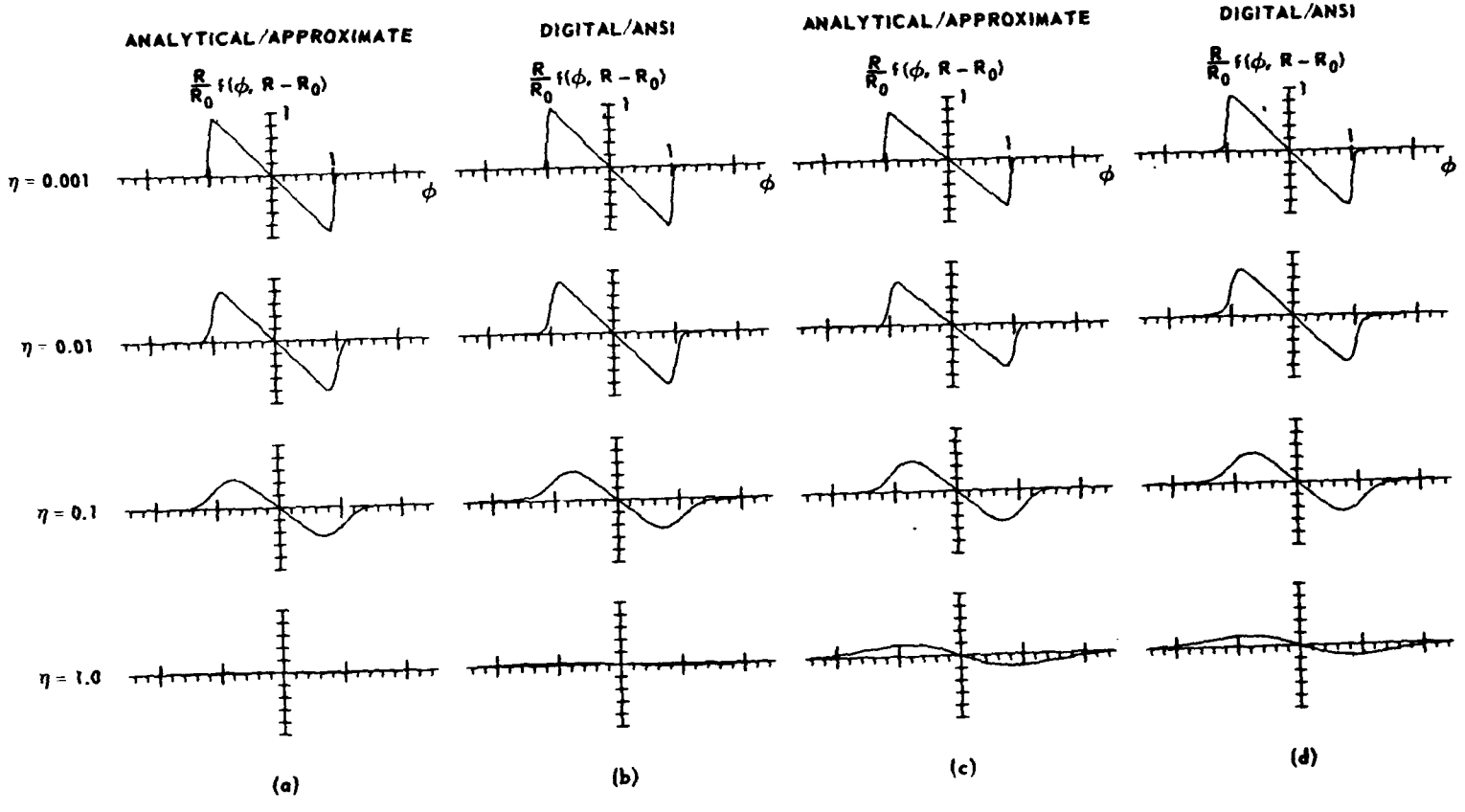

FIGURE B.4

COMPARISON OF IDEAL N WAVEFORMS CALCULATED BY ANALYTICAL AND DIGITAL METHODS FOR VARIOUS VALUES OF THE ABSORPTION PARAMETER η

INITIAL SIGNAL IS AN IDEAL N WAVE. IN COLUMNS (a) AND (b), $T_0 = 5.0\ \mu sec$, AND $R - R_0 = 0.013$, 0.13, 1.31, AND 13.1 m. IN COLUMNS (c) AND (d), $R - R_0 = 1.0\ m$ AND $T_0 = 43.7$, 13.8, 4.37, AND 1.38 μsec. RH = 48%, T = 25° C, $p_0 = 1.0$ atm

ARL:UT
AS-80-778
RDE-GA
2-22-80

approximate attenuation is far greater than the true attenuation. This disparity is manifested as an amplitude discrepancy in the upper two pairs of waveforms in Figs. B.4(c) and (d). The head and tail sections, where the high frequency components are most visible, are quite similar in the analytical and digital models. The slope of the linear portion, which depends mainly on low frequency components, is slightly lower in the analytical model.

Comparisons of column (a) with column (c) and (b) with (d) reveal the extent to which the approximate and ANSI absorption coefficients deviate from strict dependence on the single nondimensional parameter η. For example, if the constant factor $\exp[-B(R-R_o)]$ is suppressed, the analytical solution depends only on ω^2 and, hence, only on η, but the range of validity is more strictly limited at the low end. If in the digital model R is fixed and T_o is chosen to specify a certain value of η [Fig. B.4(d)], the results differ from those obtained by fixing T_o and choosing R [Fig. B.4(b)]. This is so because, for low frequency signals, the ANSI absorption is not simply dependent on ω^2.

In summary, the analytical/approximate and digital/ANSI models give similar results for ideal N waves whose half-periods are less than 5 μsec. The computer model is of course more accurate because it employs a more precise description of the atmospheric absorption.

4. Experiment

Measurements of the free-field attenuation of small-signal N waves in air were carried out using the spark source, microphone, and electronic system discussed in Chapter II. A 0.16 J spark was chosen because (1) the period of the radiated N wave was long enough

(T_o = 5.0 μsec) to ensure good measurement fidelity, and (2) the amplitude was low enough to ensure that nonlinear distortion was insignificant over the distances of interest. Experiments with shorter N waves yielded similar results, but accuracy was limited by the 0.5 μsec time resolution of the oscilloscope.

Time waveforms were recorded at distances of 40, 60, 100, and 160 cm. Preliminary results lacked consistency because of the variation or "jitter" in the spark amplitude. The following procedure was devised to statistically filter out the jitter. Only signals from sparks whose breakdown voltage was in a certain narrow range (2.0 ±0.2 kV, determined by the accuracy of the monitoring voltmeter) were stored in the oscilloscope memory. The peak amplitudes of the stored pressure waveforms were averaged for twenty such signals at each receiver location. Finally, the spark source was discharged until a signal having a peak amplitude equal to the average peak amplitude (+0.5%, -0.08%) was recorded. When an "average pressure trace" was measured in this way for each microphone position, results exhibited satisfactorily consistent trends. The standard deviation for each of the 20-term averages ranged from 2.6% to 3.7% of the average peak value. The measured "average waveforms" are shown in Fig. B.5(a). The amplitudes have been multiplied by R/R_o to suppress the effect of spherical spreading.

The reference waveform (measured at $R=R_o$) was used as an input for the computer model, and propagated waveforms were computed over the distances $R-R_o$. The computed waveforms are presented in Fig. B.5(b). Agreement between the measured and computed waveforms is well within experimental tolerance.

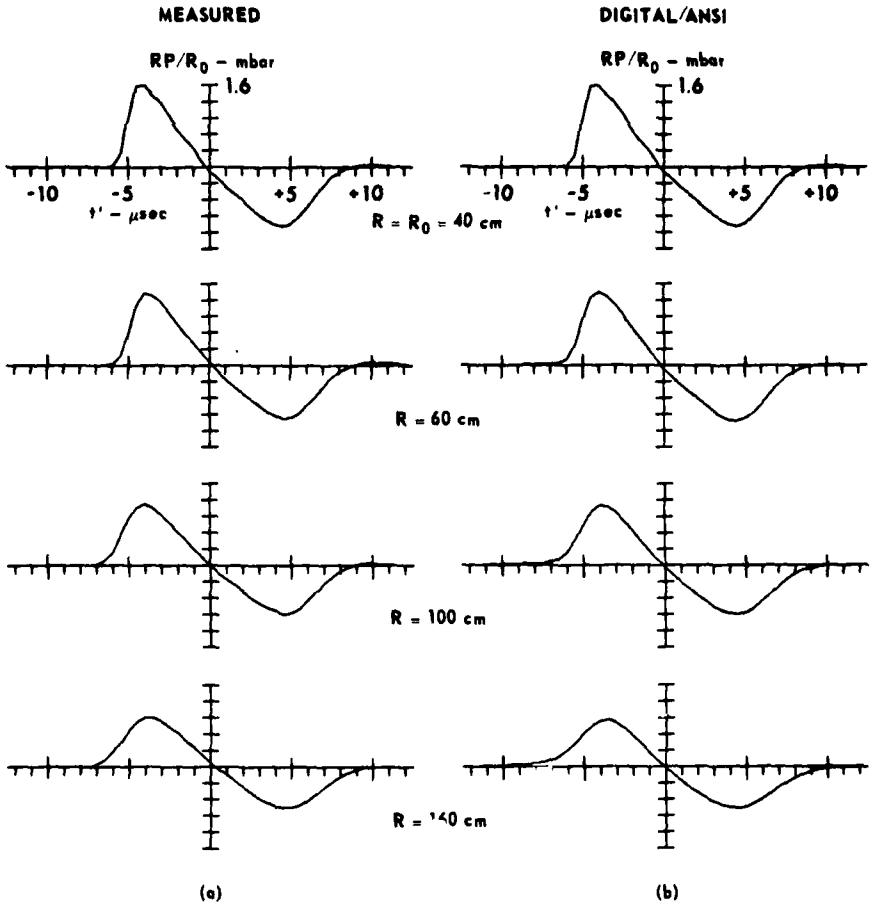

FIGURE B.5
MEASURED AND COMPUTED N WAVEFORMS AS A FUNCTION OF RANGE
RH = 48%, T = 25° C, p_0 = 1 atm

ARL:UT
AS-80-779
RDE-GA
2-22-80

5. Summary: Comparison of Analytical/Approximate Model with Measurements

The work described in this appendix was motivated by a desire to analytically describe the amplitude and shape of a small-signal N wave as it propagates through an homogeneous atmosphere. A closed-form solution based on an approximate form of the absorption coefficient has been derived for a signal that is initially an ideal N wave. The analytical/approximate solution compares favorably with a computer solution based on the American National Standard absorption. When the N wave half-period is less than or equal to 5 μsec, the results of the two models are in good agreement for the life of the waveform.

A simple attenuation experiment was performed in the open air to ascertain the effects of atmospheric absorption on a real N wave. Absorption effects were also computed using the ANSI absorption coefficient. The results, though limited in scope, are in excellent agreement, and serve to verify the absorption standard in its application to broadband signals.

To better compare the results of the analytical model with the measured data, the analytical and digital methods were used to compute waveforms (ideal N wave input) for distances equal to those traversed in the experiment. The initial value of T_o was found from measured data to be 5.0 μsec, and η was calculated from T_o and $R-R_o$. The calculated waveforms appear in Fig. B.6. If the digital model is viewed as an intermediary and the differences between the initial ideal and real input waveforms are taken into account, a very creditable correspondence between the analytical solution [Fig. B.6(b)] and measured data [Fig. B.5(a)] is apparent. The measured and numerically computed waveforms exhibit an important effect of relaxation: the midpoint of each head shock moves away from the point

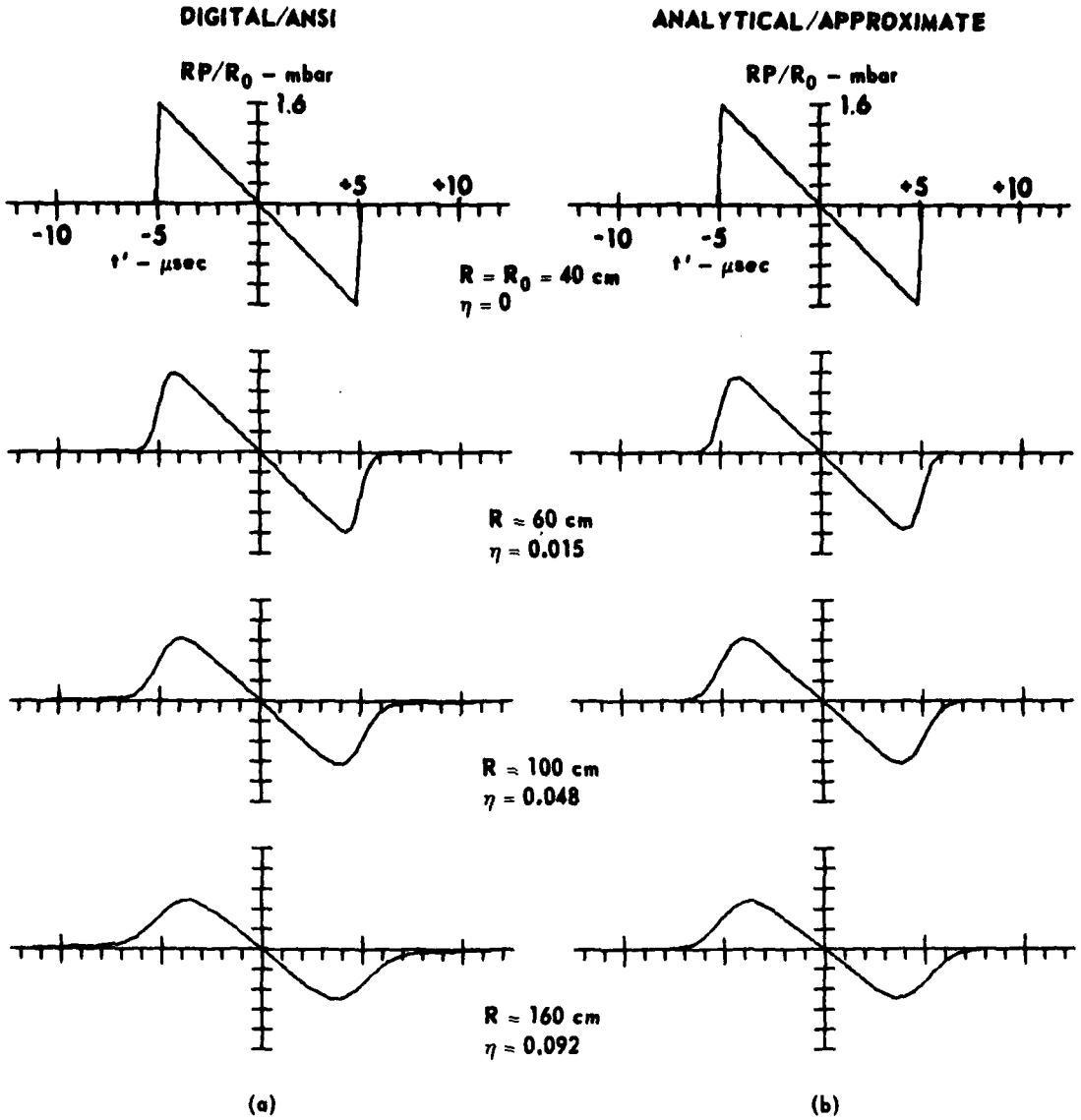

FIGURE B.6
N WAVEFORMS CALCULATED BY ANALYTICAL AND DIGITAL METHODS AS A FUNCTION OF RANGE
INITIAL SIGNAL IS AN IDEAL N WAVE
$T_0 = 5.0\,\mu sec$, RH = 48%, T = 25° C, p_0 = 1 atm

ARL:UT
AS-80-780
RDE -GA
2-22-80

$t' = -5$ μsec as the range increases. This effect is not found in the analytically calculated waveforms because the simple $A\omega^2+B$ dependence of the analytical/approximate model gives rise to waveforms which are symmetric about T_o. However, for the ranges of $R-R_o$ and T_o considered, differences between the results obtained from the two theoretical models are small. It is concluded that the analytical solution is an accurate model for propagation of small-signal, short-duration N waves over the distances encountered in the tube experiment.

APPENDIX C

PROGRAM LISTINGS

Listings for Program NTUBE, Subroutine PLTWAVE, and Function ABSORP are presented in this appendix, Program NTUBE is used to compute on-axis waveforms from a given direct waveform. Subroutine PLTWAVE is designed to plot the computed waveforms in the desired format. Function ABSORP is used to compute atmospheric absorption in accordance with ANSI Standard S1.26-1978.

```
      PROGRAM NTUBE(DATA,INPUT,OUTPUT,PLOT,OUT,TAPE1=PLOT,
     *              TAPE3=DATA,TAPE6=OUT)
C
C  PROGRAM TO COMPUTE REFLECTED WAVEFORMS FROM POINT SOURCES WITH THE
C     SOURCE AND RECIEVER ALONG THE AXIS IN A TUBE.  DATA IS A
C     DIGITIZED WAVEFORM WHICH IS ASSUMED TO HAVE TRAVELLED THE AXIAL
C     DISTANCE OF THE TUBE, X.  PROPER PHASE SHIFT IS APPLIED TO THE WAVEFORM.
C     ATMOSPHERIC ABSORPTION, MICROPHONE DIRECTIVITY FACTORS AND TWO POINT
C     SIGNAL SMOOTHING ARE OPTIONAL.
C  THE NUMBER OF POINTS IN THE DIGITIZED WAVEFORM IS REQUIRED ALONG WITH
C     THE AXIS LENGTH AND CHARACTER HEIGHT.  THESE LAST TWO PARAMETERS
C     ARE USED ONLY BY THE ARL PLOT ROUTINES.
C
C  EXTERNALS:
C    MMBSJ1 - IMSL (INTERNATIONAL MATHEMATICAL AND STATISTICAL LIBRARY)
C             FUNCTION FOR FIRST ORDER BESSEL FUNCTION OF THE FIRST KIND.
C    FFTCC  - IMSL FAST FOURIER TRANSFORM SUBROUTINE.
C    PLTWAVE- SUBROUTINE TO PLOT THE COMPUTED WAVEFORMS, USING ARL WRITTEN
C             PLOTTING SUBROUTINES.
C    ABSORP - ARL FUNCTION TO COMPUTE THE ATMOSPHERIC ABSORPTION COEFF IN AIR.
C
C
      REAL WK(1650),Y(250),T(250),DELTAT,YPLT(250),NORM,KA,MMBSJ1
      INTEGER N,IWK(1650),REFNO
      COMPLEX A(250),B,CPHASE,BN
      CO=343.0
C
C  SET INITIAL VALUES AND OPTIONS (SELECTED BY  #YES# - #NO#  RESPONSES).
      PRINT*,#INPUT NUMBER OF POINTS, AXIS LENGTH #,
      READ*,N,AXLEN
      PRINT*,#ABSORB TO BE APPLIED+, MIC FACTOR+, SIGNAL SMOOTHING#,
      READ*,IAB,MICFAC,NAVG
C
C
C  READ THE DIGITIZED WAVEFORM FROM THE FILE (FREE FORMAT INPUT),
C    THE LAST RECORD CONTAINS THE DATA PARAMETERS.
C    IDENT : COL 01-10  UP TO 10 CHARACTER IDENTIFICATION OF THE WAVEFORM.
C    PER   : COL 11-20  PERIOD (IN SECONDS) OF INPUT WAVEFORM.
C    X     : COL 21-30  DISTANCE IN TUBE FROM SOURCE TO RECIEVER (METERS).
```

```
PROGRAM NTUBE      73/171  OPT=1                                FTN 4.7+485        80/07/15. 12.13.57

C     TRAD  : COL 31-40  RADIUS OF TUBE (METERS).
C     TEMP  : COL 41-50  TEMPERATURE OF AIR IN TUBE (DEGREES C).
C     RH    : COL 51-60  RELATIVE HUMIDITY IN TUBE (PERCENT
C
      DO 10 J=1,N
      READ(3,*)Y(J)
   10 CONTINUE
      READ(3,300)IDENT,PER,X,TRAD,TEMP,RH
      TEMP=TEMP+273.15
C
C
C  DELTAF=DIFFERENCE IN FREQUENCIES OF THE POINTS IN THE FREQ.DOMAIN.
      DELTAF=1./PER
C
C  SET UP TIME ARRAY FOR PLOTTING N-WAVE.
      N=N-1
      DELTAT=5./N
      DO 20 J=1,N
      T(J)=-2.5+(J-1)*DELTAT
   20 CONTINUE
C  FIX END POINT.
      N=N+1
      T(N)=2.5
C
C  PRINT OUT DATA AND TIME ARRAY.
      WRITE(6,200)IDENT,(T(J),Y(J),J=1,N)
      WRITE(6,400)PER,X,TRAD,TEMP,RH
C
C
C  NORMALIZE ZERO TO PEAK AMPLITUDE OF WAVEFORM TO 5:
C      GET LARGEST VALUE OF INPUT DATA.
      NORM=Y(1)
      DO 15 J=2,N
      IF(Y(J).LE.NORM)GOTO 15
      NORM=Y(J)
   15 CONTINUE
C      NORMALIZE ARRAY BY DIVIDING THE DATA BY NORM THEN * 5.
      DO 17 J=1,N
      Y(J)=Y(J)/NORM*5.0
```

```
   17 CONTINUE
C
C  PLOT INITIAL N-WAVE.
      REFNO=0
      CALL PLWAVE(T,Y,N,AXLEN,IDENT,REFNO)
C
C  NORMALIZE WAVEFORM TO 1.
      DO 18 J=1,N
      Y(J)=Y(J)/5.0
      A(J)=CMPLX(Y(J),0.0)
   18 CONTINUE
C
C
    1 CONTINUE
C  INPUT THE NUMBER OF THE REFLECTION IN THE TUBE.
      PRINT*,$ENTER N$,
      READ*,REFNO
C
C  COMPUTE PHASE SHIFT IN DEGREES.
      PHASE=45.0+(REFNO-1)*90.0
      IF(REFNO.EQ.0)PHASE=0.0
C  CONVERT PHASE TO RADIANS.
      PHASE=.0174533*PHASE
C
C  COMPUTE EFFECTIVE DISTANCE WAVE TRAVELLED FOR INPUT NO OF REFLECTIONS.
C    INPUT WAVEFORM HAS ALREADY PROPOGATED DIST X SO ADDITIONAL
C    ABSORPTION NEED ONLY BE APPLIED TO THE DIFF DUE TO REFLECTIONS.
      RN=SQRT(X*X+(2.*TRAD*REFNO)**2)
      RD=RN-X
      SINT=2.*REFNO*TRAD/RN
C  COMPUTE MICROPHONE DIRECTIVITY TERM.
      KA=2.*3.1415927*.001/343.*SINT
C
C
C  TRANSFORM N-WAVE TO FREQ. DOMAIN.
      CALL FFTCC(A,N,IWK,WK)
C  PHASE SHIFT THE WAVE:
C      MULTIPLY THE FIRST HALF OF POINTS BY EXP(-I*PHI) AND
C      THE SECOND HALF OF THE POINTS BY EXP(I*PHI),
```

```
C          WHERE: I=SQRT(-1).
C  THEN APPLY (IF REQUESTED) ATMOSPHERIC ABSORPTION
C     AND MICROPHONE DIRECTIVITY FACTORS TO THE FREQ COMPONENTS.
C  THE FFT ROUTINE PRODUCES THE COMPLEX CONJUGATE OF THE TRANSFORM, TO
C     OBTAIN THE CORRECT TRANSFORMATION THE VALUES MUST BE COMPLEX CONJUGATED
C     BEFORE THEY ARE MULTIPLIED BY THE PHASE FACTOR.
      NIHALF=N/2+1
C  COMPUTE PHASE FACTOR IN FREQUENCY DOMAIN.
      CPHASE=CMPLX(0.0,PHASE)
      B=CEXP(CPHASE)
      BN=CEXP(-CPHASE)
      A(1)=CONJG(A(1))*B
C  COMPUTE FIRST HALF OF THE FREQUENCY COMPONENTS.
      DO 40 J=2,NIHALF
      F=DELTAF*(J-1)
      OMEGA=F*2.*3.141592
      A(J)=CONJG(A(J))*B*SQRT(OMEGA)
      IF(IAB.EQ.≠YES≠)A(J)=A(J)*(10.**(-ABSORP(TEMP,1.0,RH,F)/20*RD))
      ARG=KA*F
      IF(MICFAC.EQ.≠YES≠)A(J)=A(J)*2.*MMBSJ1(ARG,IER)/ARG
   40 CONTINUE
      NIHALF=NIHALF+1
C  COMPUTE SECOND HALF OF THE FREQUENCY COMPONENTS.
      DO 50 J=NIHALF,N
      F=DELTAF*(N+1-J)
      OMEGA=F*2.*3.141592
      A(J)=CONJG(A(J))*BN*SQRT(OMEGA)
      IF(IAB.EQ.≠YES≠)A(J)=A(J)*(10.**(-ABSORP(TEMP,1.0,RH,F)/20*RD))
      ARG=KA*F
      IF(MICFAC.EQ.≠YES≠)A(J)=A(J)*2.*MMBSJ1(ARG,IER)/ARG
   50 CONTINUE
C TRANSFORM BACK TO TIME DOMAIN.
      CALL FFTCC(A,N,IWK,WK)
C
C
C  PUT THE REAL PART OF A INTO YPLT AND RE-NORMALIZE THE WAVEFORM FROM THE
C    TRANSFORM BY DIVIDING THE TIME COMPONENTS BY N.  ALSO SMOOTH WAVEFORM
C    BY TWO POINT AVERAGING (IF REQUESTED); AND APPLY AMPLITUDE FACTOR.
      NP=N
```

```
      IF(NAVG.EQ.≠YES≠)NP=N-1
      AMP=X*SINT*SQRT(2.*3.141592/CO/RN)
      DO 60 J=1,NP
      IF(NAVG.EQ.≠YES≠)A(J)=(A(J)+A(J+1))/2.
      A(J)=A(J)/N*AMP
      YPLT(J)=REAL(A(J))
   60 CONTINUE
C
C  PLOT COMPUTED REFLECTED WAVEFORM.
      CALL PLTWAVE(T,YPLT,NP,AXLEN,IDENT,REFNO)
C
      PRINT*,≠OBTAIN ANOTHER WAVEFORM≠,
      READ*,IANS
      IF(IANS.NE.≠YES≠)STOP

   PLACE THE ORIGINAL NORMALIZED WAVEFORM BACK INTO A.
      DO 70 J=1,N
      A(J)=CMPLX(Y(J),0.0)
   70 CONTINUE
C
      GOTO 1
C
C
C ******************** FORMATS ****************************
C
  200 FORMAT(≠1≠,/,12X,A10,/,≠0≠,7X,≠TIME AND AMPLITUDE VALUES≠,/,≠0≠,/
     1       ,123(5X,F5.2,8X,F6.1,/))
  300 FORMAT(A10,E10.3,F10.4,F10.5,F10.2,F10.2,F10.0)
  400 FORMAT(≠0≠,5X,≠PERIOD=≠,E10.3,/,6X,≠TUBE AXIAL DIS.=≠,F6.4,/,
     1       6X,≠TUBE RADIUS=≠,F6.5,/,6X,≠TEMP=≠,F6.2,/,6X,
     2       ≠RELATIVE HUMID=≠,F6.2)
      END
```

```
      SUBROUTINE PLTWAVE(T,Y,N,AXLEN,IDENT,REFNO)
C  SUBROTINE PLOTS THE WAVEFORM ON A CENTERED AXIS FROM -1 TO 1.
C  ONLY VALUES FROM -3 TO 3 ARE PLOTED.
C
C  PARAMETERS:
C    T     -  X (TIME) ARRAY.
C    Y     -  Y (AMPLITUDE) ARRAY.
C    N     -  NUMBER OF POINTS TO PLOT.
C    AXLEN -  LENGTH (IN INCHES.XX) OF AXES.
C    IDENT -  ALPHAMERIC IDENTIFICATION PLACED ON PLOT.
C    REFNO -  NUMBER OF REFLECTIONS OF THE WAVE TO BE PLOTTED, USED ONLY
C             AS A REFERENCE PLACED ON THE PLOT.
C
      DIMENSION T(250),Y(250)
      INTEGER LABEL1(1),REFNO
      REAL YP(250)
      AYLEN=1.2*AXLEN
      XORIG=.5*AXLEN
      YORIG=.5*AYLEN
      DX=5./AXLEN
      DY=30./AYLEN
      PSEP=8.5
      LABEL1(1)=2H
C
      CALL PLTLEN(4LPLOT,6HNPHASE)
      CALL PLTDIM(8.5,11.0,0,4)
      CALL ORIGIN(1.0,5.0)
      CALL PLTAXIT(0.0,0.0,AXLEN,0.0,-2.5,2.5,.2,LABEL1,-2,0)
      CALL ORIGIN(XORIG,-YORIG)
      CALL PLTAXIS(0.0,0.0,AYLEN,90.0,-15.,15.,1.,LABEL1,2,0)
      CALL PLTAXIS(0.0,0.0,AYLEN,90.0,-15.,15.,1.,LABEL1,-2,0)
      CALL ORIGIN(0.0,YORIG)
C
C  SET ANY POINTS GREATER THAN 15 (RESP. LESS THAN -15),
C    TO 15 (RESP. -15).
      DO 10 J=1,N
      YP(J)=Y(J)
      IF(ABS(Y(J)).LT.15.0)GOTO 10
      YP(J)=SIGN(15.,Y(J))
```

```
   10 CONTINUE
C
C  PLOT THE DATA.
      CALL PLTDATA(T,YP,N,0,0,0.0,DX,0.0,DY,0.0)
C
C  PLACE THE DATA IDENTIFYING LABEL AND REFLECTION NUMBER ON PLOT.
      CALL PLTLINE(-XORIG,-4.0,.14,0.0,3LLTN)
      WRITE(1,300)IDENT,REFNO
C
      CALL PLTEND(PSEP)
      RETURN
C
  100 FORMAT(#1#)
  200 FORMAT(#-1#)
  400 FORMAT(#2.5#)
  500 FORMAT(#-2.5#)
  300 FORMAT(A1,/,#NO OF REFLECTIONS: #,I2)
      END
```

```
FUNCTION ABSORP     73/171  OPT=1                          FTN 4.7+485        80/07/15. 12.13.57

      FUNCTION ABSORP(T,P,RH,F)
C     PROGRAM CALCULATES ATMOSPHERIC ABSORPTION COEFFICIENT
C  ALGORITHM FROM FORMULAS GIVEN BY H. E. BASS IN WYLE LAB REPORT 72-2
C        F   FREQUENCY (HZ)
C        P   ATMOSPHERIC PRESSURE(ATMOSPHERES)
C        T   AIR TEMPERATURE (DEGREES KELVIN)
C        RH  RELATIVE HUMIDITY (PERCENT)
C     SOLUTION IN DB/METER
C     ACCURACY OF SOLUTION
C  + OR - 5 PERCENT FOR T FROM 273 TO 313
C                          RH FROM 0 TO 100
C                          F FROM 50 HZ TO 10 MHZ
C                          P FROM .03 TO 1 ATM
C     F/(P/P0) MUST BE LESS THAN 10MHZ
      T1=273.16
      RATIO=T1/T
      ARG1=-8.29692*(1./RATIO-1.)
      ARG2=4.76955*(1.-RATIO)
      ARG3=10.79586*(1.-RATIO)-5.02808*ALOG10(1./RATIO)+1.50474E-04*
     1  (1.-10**ARG1) +4.2873E-04*(10**ARG2-1.)-2.2195983
      PSP=10**ARG3
      H=RH*PSP/P
      FRO=P*(24.+4.41E+04*((.05+H)/(.391+H))*H)
      TRATIO=T/293.15
      FRN=P/SQRT(TRATIO)*(9.+350.*H*EXP(-6.142*((TRATIO**(
     1  -.33333333333))-1.)))
      ARG4=8.6859*SQRT(TRATIO)*(F**2.)/P
      ARG5=1.84E-11+2.1913E-04/TRATIO*P*((2239.1/T)**2.)*EXP(-2239.1/T)
     1 /(FRO+F**2./FRO)
      ARG6=8.1619E-04/TRATIO*P*((3352./T)**2.)*EXP(-3352./T)/
     1 (FRN+F**2./FRN)
      ABSORP=ARG4*(ARG5+ARG6)
      RETURN
      END
```

REFERENCES

1. Ervin Kay and Joseph B. Keller, "Asymptotic Evaluation of the Field at a Caustic," J. Appl. Phys. 25, 876-883 (1954). See also Refs. 3, 24, 33.

2. Jean-François Hamet, "Pulse Propagation in a Cylindrical Resonator," M.S. Thesis, School of Engineering and Applied Science, University of California, Los Angeles, California (1969).

3. Jean-François Hamet, "Some Acoustic Phenomena Related to Curved Surfaces," Technical Report UCLA-Eng-7142, School of Engineering and Applied Science, University of California, Los Angeles, California (1971).

4. G. Kirchhoff, "Ueber den Einfluss der Wärmseleitung in einem Gase auf die Schallbewegung," Ann. der Phys. 134, 177-193 (1868).

5. Lord Rayleigh, The Theory of Sound (Dover Publications, New York, 1945) Vol. II, pp. 319-328.

6. H. E. Hartig and R. F. Lambert, "Attenuation in a Rectangular Slotted Tube of (1,0) Transverse Acoustic Waves," J. Acoust. Soc. Am. 22, 42-47 (1950).

7. B. P. Bogert, "Classical Viscosity in Tubes and Cavities of Large Dimensions," J. Acoust. Soc. Am. 22, 432-437 (1950).

8. E. A. G. Shaw, "Attenuation of (1,0) 'Transverse' Acoustic Waves in a Rectangular Tube," J. Acoust. Soc. Am. 22, 512 (1950).

9. Ralph E. Beatty, Jr., "Attenuation of (n,0) Transverse Modes in a Rectangular Tube," J. Acoust. Soc. Am. 22, 639 (1950).

10. Ralph E. Beatty, Jr., "Boundary Layer Attenuation of Higher Order Modes in Rectangular and Circular Tubes," J. Acoust. Soc. Am. 22, 850-854 (1950).

11. Robert F. Lambert, "Wall Viscosity and Heat Conduction Losses in Rigid Tubes," J. Acoust. Soc. Am. 23, 480-481 (1951).

12. F. Douglas Shields, K. P. Lee, and W. J. Wiley, "Numerical Solution for Sound Velocity and Absorption in Cylindrical Tubes," J. Acoust. Soc. Am. 37, 724-729 (1965).

13. F. Douglas Shields, H. E. Bass, and N. L. Bolen, "Tube Method of Sound Absorption Extended to Frequencies Far Above Cutoff," J. Acoust. Soc. Am. 62, 346-353 (1977).

14. H. Tijdeman, "On the Propagation of Sound Waves in Cylindrical Tubes," J. Sound Vib. 39, 1-33 (1975).

15. H. A. Scarton and W. T. Rouleau, "Axisymmetric Waves in Compressible Newtonian Liquids Contained in Rigid Tubes: Steady-Periodic Mode Shapes and Dispersion by the Method of Eigenvalleys," J. Fluid Mech. 58, 595-621 (1973).

16. D. V. Anderson, T. D. Northwood, and C. Barnes, "The Reflection of a Pulse by a Spherical Surface," J. Acoust. Soc. Am. 24, 276-283 (1952).

17. H. A. Wright, Jr., "Time-Domain Analysis of Broad-Band Refraction and Diffraction," J. Acoust. Soc. Am. 46, 661-666 (1969).

18. James C. Lockwood, "Two Problems in High Intensity Sound. Part II. The Diffraction of N Waves by a Circular Aperture in a Plane Baffle," Applied Research Laboratories Technical Report No. 71-26 (ARL-TR-71-26), Applied Research Laboratories, The University of Texas at Austin, July 1971 (AD 740 498).

19. Wesley N. Cobb, "Diffraction of a Plane N Wave of Finite Amplitude by a Slit," Applied Research Laboratories Technical Report No. 77-43 (ARL-TR-77-43) (AFOSR-TR-78-0149), Applied Research Laboratories, The University of Texas at Austin, August 1977 (ADA 050 410).

20. Wayne M. Wright, "Studies of N Waves from Weak Sparks in Air, Final Report," ONR Report NR-384-321, Physics Dept., Kalamazoo College, Kalamazoo, Michigan, June 1971 (AD 725 865).

21. G. B. Whitham, "A New Approach to Problems of Shock Dynamics. Part I: Two Dimensional Problems," J. Fluid Mech. 2, 145-171 (1957).

22. G. B. Whitham, "A New Approach to Problems of Shock Dynamics. Part II: Three Dimensional Problems," J. Fluid Mech. 5, 369-386 (1957).

23. B. A. Davy and D. T. Blackstock, "Measurements of the Refraction and Diffraction of a Short N Wave by a Gas-Filled Soap Bubble," J. Acoust. Soc. Am. 49, 732-737 (1971).

24. W. D. Beasley, J. D. Brooks, and R. L. Barger, "A Laboratory Investigation of N-Wave Focusing," NASA Technical Note TN D-5306, Langley Research Center, Hampton, Virginia, 1969.

25. E. P. Cornet, "Focusing of an N Wave by a Spherical Mirror," Applied Research Laboratories Technical Report No. 72-40 (ARL-TR-72-40) (AFOSR-TR-73-0624), Applied Research Laboratories, The University of Texas at Austin, 19 September 1972 (AD 757 035).

26. Bradford Sturtevant, "Studies of Shock Focusing and Nonlinear Resonance in Shock Tubes," Proceedings of the 9th International Shock Tube Symposium, Stanford University, 1973, pp. 23-34.

27. B. Sturtevant and V. A. Kulkarny, "Dynamics of Weak Shock Waves at a Focus," Proceedings of the Interagency Symposium on University Research in Transportation Noise, North Carolina State University, Raleigh, North Carolina, 5-7 June 1974, Vol. I, pp. 402-415.

28. M. Sanai, T. Y. Toong, and A. D. Pierce, "Ballastic Range Experiments on Superbooms Generated by Refraction," J. Acoust. Soc. Am. 59, 513-519 (1976), and "Ballistic Range Experiments on the Superboom Generated at Increasing Flight Mach Numbers," J. Acoust. Soc. Am. 59, 520-524 (1976).

29. Frederick M. Pestorius, "Propagation of Plane Acoustic Noise of Finite Amplitude," Applied Research Laboratories Technical Report No. 73-23 (ARL-TR-73-23)(AFOSR-TR-74-0711), Applied Research Laboratories, The University of Texas at Austin, August 1973 (AD 778 868).

30. Mark O. Anderson, "The Propagation of a Spherical N Wave in an Absorbing Medium and Its Diffraction by a Circular Aperture," Applied Research Laboratories Technical Report No. 74-25 (ARL-TR-74-25) (AFOSR-TR-74-1736), Applied Research Laboratories, The University of Texas at Austin, August 1974 (AD 787 878).

31. John H. Gardner and Peter H. Rogers, "Thermospheric Propagation of Sonic Booms from the Concorde Supersonic Transport," NRL Memorandum Report 3904, Naval Research Laboratory, Washington, D.C., November 1978.

32. P. H. Rogers and J. H. Gardner, "Sonic Booms in the Thermosphere," J. Acoust. Soc. Am. 67, 78-91 (1980).

33. W. L. Roever, J. H. Rosenbaum, and T. F. Vining, "Acoustic Waves from an Impulsive Source in a Fluid-Filled Borehole," J. Acoust. Soc. Am. 55, 1144-1157 (1974).

34. Jeremy Hall, Frank Miller, and Gene Simmons, "A Technique for the Precise Measurements of Acoustic Velocity in, and Between, Boreholes with a Sparker Source," Geoexploration 17, 179-184 (1979).

35. M. Salikuddin, P. D. Dean, H. E. Plumblee, Jr., and K. K. Ahuja, "An Impulse Test Technique with Application to Acoustic Measurements," AIAA 5th Aeroacoustics Conference, Seattle, Washington, 12-14 March 1979, Paper 79-0679.

36. Harry E. Plumblee, Jr., Personal communication to D. T. Blackstock, 7 April 1980.

37. Wayne M. Wright, "High Frequency Electrostatic Transducers for Use in Gases," Acoustics Research Laboratory Technical Memorandum No. 47, Acoustics Research Laboratory, Harvard University, Cambridge, Massachusetts, 1962.

38. Henry Wallman, "Bandpass Amplifiers: Pulse Response and General Considerations," in Vacuum Tube Amplifiers, George E. Valley and Henry Wallman (eds.) McGraw-Hill Book Co., Inc., New York, New York, 1948), Chapter 7, pp. 274-300. See especially the graphs on p. 280.

39. See, for example, Marvin E. Goldstein, Aeroacoustics (McGraw-Hill Book Co., Inc., New York, 1976), p. 26.

40. David T. Blackstock, "Approximate Equations Governing Finite-Amplitude Sound in Thermoviscous Fluids," General Dynamics Technical Report GD-1463-52 (AFOSR-5223), General Dynamics/Electronics, Rochester, New York, May 1963 (AD 415 442).

41. Philip M. Morse and Herman Feshbach, Methods of Theoretical Physics (McGraw-Hill Book Co., Inc., New York, 1953), pp. 808-811.

42. Ian N. Sneddon, Fourier Transforms (McGraw-Hill Book Co., Inc., New York, 1951), pp. 516-519.

43. David T. Blackstock, "High-Intensity Sound Research, 1961-1978 (Final Report under Contract F44620-76-C-0040), Applied Research Laboratories Technical Report No. 79-36 (ARL-TR-79-36)(AFOSR-TR-79-0906), Applied Research Laboratories, The University of Texas at Austin, July 1979 (ADA 072 550).

44. See, for example, David T. Blackstock, "Nonlinear Acoustics (Theoretical)," in American Institute of Physics Handbook, D. E. Grey (ed.) (McGraw-Hill Book Co., Inc., New York 1972), Chapter 3n, p. 3-187.

45. The earliest use of this approach is found in L. D. Landau and E. M. Lifshitz, Fluid Mechanics (Pergamon Press, London, 1959), pp. 375-376.

A.1 Henry Stark and Franz B. Tuteur, Modern Electrical Communications: Theory and Systems (Prentice-Hall, Englewood Cliffs, New Jersey, 1979), Chap. 2.

B.1 American National Standard Method for the Calculation of the Absorption of Sound by the Atmosphere, S1.26-1978/ASA 23 (1978).

B.2 L. B. Evans, H. E. Bass, and L. C. Sutherland, "Atmospheric Absorption of Sound: Theoretical Predictions," J. Acoust. Soc. Am. 51, 1564-1575 (1972).

B.3 Martin Greenspan, "Rotational Relaxation in Nitrogen, Oxygen, and Air," J. Acoust. Soc. Am. 31, 155-160 (1959).

B.4 H. E. Bass and Roy G. Keeton, "Ultrasonic Absorption in Air at Elevated Temperatures," J. Acoust. Soc. Am. 58, 110-112 (1975).

B.5 Wayne M. Wright, "Studies of N Waves from Weak Sparks in Air, Final Report, "ONR Report NR-384-321, Physics Dept., Kalamazoo College, Kalamazoo, Michigan, June 1971 (AD 725 865).

B.6 See Ref. 32.

4 May 1981

DISTRIBUTION LIST FOR
ARL-TR-81-22
UNDER CONTRACT N00014-75-C-0867

Copy No.	
1 - 3	Office of Naval Research Physics Program Office (Code 421) 800 North Quincy Street Arlington, VA 22217
4	Office of Naval Research Director, Technology (Code 200) 800 North Quincy Street Arlington, VA 22217
	Director Defense Advanced Research Projects Agency 1400 Wilson Blvd. Arlington, VA 22209
5 - 7	Attn: Technical Library
	Naval Research Laboratory Department of the Navy Washington, DC 20375
8 - 10	Attn: Technical Library
11 - 13	Office of the Director of Defense Research and Engineering Information Office Library Branch The Pentagon Washington, DC 20301
14 - 15	U. S. Army Research Office Box 12211 Research Triangle Park, NC 27709
16 - 27	Defense Technical Information Center Cameron Station, Bldg. 5 5010 Duke Street Alexandria, VA 22314
	Director, National Bureau of Standards Department of Commerce Washington, DC 20234
28	Attn: Technical Library

Distribution List for ARL-TR-81-22 under contract N00014-75-C-0867 (Cont.)

Copy No.	
29 - 31	Commanding Officer Office of Naval Research Western Regional Office 1030 East Green Street Pasadena, CA 91101
32 - 34	Commanding Officer Office of Naval Research Eastern/Central Regional Office 666 Summer Street Boston, MA 02210
	Commandant of the Marine Corps Washington, DC 20380
35	Attn: Scientific Advisor (Code RD-1)
	Naval Ordnance Station Indian Head, MD 20640
36	Attn: Technical Library
	Naval Postgraduate School Monterey, CA 93940
37	Attn: Technical Library (Code 0212)
	Naval Missile Center Point Mugu, CA 93010
38	Attn: Technical Library (Code 5632.2)
	Naval Ordnance Station Louisville, KY 40214
39	Attn: Technical Library
	Commanding Officer Naval Ocean Research & Development Activity NSTL Station, MS 39529
40	Attn: Technical Library
	Naval Explosive Ordnance Disposal Facility Indian Head, MD 20640
41	Attn: Technical Library
	Naval Ocean Systems Center Department of the Navy San Diego, CA 92152
42	Attn: Technical Library

Distribution List for ARL-TR-81-22 under contract N00014-75-C-0867 (Cont.)

Copy No.	
	Naval Surface Weapons Center White Oak Laboratory Department of the Navy Silver Spring, MD 20910
43	Attn: Technical Library
	David W. Taylor Naval Ship Research and Development Center Department of the Navy Bethesda, MD 20084
44	Attn: Central Library (Code L42 and L43)
	Naval Avionics Facility Department of the Navy Indianapolis, IN 46218
45	Attn: Technical Library
	Director U. S. Army Engineering Research and Development Laboratories Fort Belvoir, VA 22060
46	Attn: Technical Documents Center
47 - 49	ODR&E Advisory Group on Electron Devices 201 Varick Street New York, NY 10014
50	Air Force Office of Scientific Research Department of the Air Force Bolling AFB, DC 22209
	Air Force Weapons Laboratory Kirtland Air Force Base Albuquerque, NM 87117
51	Attn: Technical Library
	Air Force Avionics Laboratory Air Force Systems Command Wright-Patterson Air Force Base Dayton, OH 45433
52	Attn: Technical Library
	Lawrence Livermore Laboratory University of California P.O. Box 808 Livermore, CA 94550
53	Attn: Dr. W. F. Krupke

Distribution List for ARL-TR-81-22 under contract N00014-75-C-0867 (Cont.)

Copy No.	
	Harry Diamond Laboratories 2800 Powder Mill Road Adelphi, MD 20783
54	Attn: Technical Library
	Naval Air Development Center Department of the Navy Johnsville Warminster, PA 18974
55	Attn: Technical Library
	Naval Weapons Center Department of the Navy China Lake, CA 93555
56	Attn: Technical Library (Code 753)
	Naval Training Equipment Center Department of the Navy Orlando, FL 32813
57	Attn: Technical Library
58	Naval Underwater Systems Center New London Laboratory Detachment Technical Center New London, CT 06320
59	Office of Naval Research Resident Representative Room No. 582, Federal Building Austin, TX 78701
60	Physical Sciences Group, ARL:UT
61	Reuben H. Wallace, ARL:UT
62	Library, ARL:UT
63 - 100	Reserve, ARL:UT